2023

Aerosol Synthesis of Tungsten Bronze Particles for NIR Shielding

Hao Tu
Virginia Commonwealth University

Aerosol Synthesis of Tungsten Bronze Particles for NIR Shielding

A dissertation submitted in partial fulfillment of the requirements for the degree of
Doctor of Philosophy at Virginia Commonwealth University

By

Hao Tu
M.S., Material Science, Wuhan University of Technology, China, 2015
B.S., Inorganic Non-metallic Material Engineering, Wuhan University of Technology, China, 2011

Advisor: Daren Chen
Floyd D Gottwald Sr. Professor,
Department of Mechanical and Nuclear Engineering

Virginia Commonwealth University
Richmond, Virginia
April, 2023

Acknowledgment

I am immensely grateful to my supervisor, Prof. Dare Chen, for his constructive advice, constant support, and generous help during my Ph.D. journey. Prof. Chen not only instructs me on academic research but also imparts valuable life lessons to me. I am deeply inspired by his professionalism, positivity, motivation, discipline, and passion, which helped me grow as a person and a researcher. I also appreciate his wife and family's warmth and kindness in a foreign land. You have made this possible for me. I also want to thank my dissertation committee members sincerely: Prof. Wei-Ning Wang, Prof. Sheng-Chieh Chen, Prof. David Pui, and Prof. Jing Wang. Your expertise, insightful feedback, and guidance were essential for my Ph.D. program. I also thank Prof. Dmitry Pestov and Prof. Carl Mayer for their technical assistance in material characterization in the VCU facility center. I also thank my graduate program director Prof. Karla Mossi for her continuous help and support. I am also grateful to Dr. Di Liu and Dr. Peng Wang, my mentors and friends, during my Ph.D. study. I also thank Dr. Zan Zhu, Yu Zhang, Yuanhang Yang, Jie Zhang, Hao Chen, Xiaofei Li, Chenchao Fang, Jingtao You, Dr. Mingyao Mou, and Dr. Xiaotong Chen for your camaraderie and support over the past few years. Finally, I am grateful to my loving wife, X. L. Sun, my son, J. Y. Tu, my father, J. Q. Tu, and my mother, J. Yu, for being with me all the way. Your love, support, understanding, and encouragement are the most precious gifts in my life.

Table of contents

List of figures

List of tables

Abstract

Due to the challenges of global warming and the energy crisis, this dissertation stresses the importance of efficient energy utilization in sectors like buildings and transportation that use much energy for HVAC systems. It shows how improving HVAC systems can lower energy consumption and emissions and support sustainability and global warming mitigation. Solar radiation, especially near-infrared (NIR) radiation, increases the energy consumption of HVAC systems in vehicles and buildings. Blocking NIR radiation can save energy and money by reducing air conditioning loads. The dissertation introduces various transparent NIR shielding products and their growing global market value.

Tungsten bronze is a NIR shielding material that can absorb the whole NIR range and transmit high visible light. This dissertation compares it with other NIR shielding materials to demonstrate the advantages of tungsten bronze on NIR shielding. The tungsten bronze particles can be coated on transparent media to reduce the indoor temperature under solar radiation. However, the previous methods of producing tungsten bronze particles are energy and time-consuming. Thus, this dissertation introduces the continuous production of tungsten bronze particles via aerosol synthesis. Multiple setup match with different precursors and solvents are presented in the thesis. The effect of precursor and solvent are also discussed. The high-quality tungsten bronze particle can be produced through a cheap and environmentally friendly precursor and solvent.

Particle size has an essential effect on optical performance. The particle size of tungsten bronze on NIR shielding is valuable to investigate for improving performance. The dissertation introduces the tungsten bronze particle of different sizes being separated by the cascade impactor. The vis-NIR spectrum for different sizes of tungsten bronze particles is measured. The most suitable particle size for NIR shielding is found by SETS calculation.

In practice NIR shielding application, the functional particles are randomly suspended in a transparent carry matrix. The dissertation also presents our work on the optical modeling of tungsten bronze particles to investigate the random particle location and multi-scattering effect on the NIR shielding performance. The effect of the particle's size, concentration, and shape on the NIR optics is explained in detail in the thesis.

Keywords: Aerosol-assisted, Tungsten Bronze, Particle, NIR Shielding

Chapter 1. Introduction

Humanity faces two critical challenges today: global warming and the energy crisis. Renewable energy is a promising solution to these problems, and significant efforts have been made to develop large-scale wind, hydro, solar, biomass, and geothermal power systems. The use of renewable energy has grown to approximately 11%[1] of total energy consumption since the introduction of global warming and climate change concepts in the 1980s. However, in addition to developing new energy sources, efficient energy utilization is also essential to reduce greenhouse gas emissions and energy consumption. This is particularly important in sectors with significant energy consumption, such as buildings and transportation. In these sectors, ventilation and air conditioning (HVAC) systems consume a considerable amount of energy, and improving their energy efficiency can significantly reduce energy consumption and associated emissions. For example, in fuel-powered vehicles, air conditioning (AC) can consume up to 0.2 ~ 1 liter of petrol per 100 km, while in electric vehicles, it can consume up to 10-20% of the battery's energy. In buildings, air cooling alone accounts for 11.3% of electricity consumption in the US commercial sector and 18.58% in the residential sector.[2] Therefore, addressing energy efficiency in HVAC systems is crucial for achieving sustainable energy consumption and reducing the impact of global warming.

1.1 Significance of NIR shielding

Solar radiation is the main heat source during the day and the primary reason for the energy consumption of vehicles and buildings' air conditioning systems. Although human eyes can only perceive visible light, solar radiation contains significant invisible energy, particularly in the near-infrared (NIR) range, the major thermal energy source. NIR accounts for approximately 50%[3] of solar radiation. In the case of building air conditioning, up to 30%[4] of energy consumption is attributed to solar radiation penetrating through windows. Therefore, blocking this invisible thermal energy can reduce air conditioning loads and decrease energy consumption in vehicles and buildings. According to 2021 data from US Energy Information Administration[2], if all US commercial and residential windows blocked the entire NIR spectrum from solar radiation, electricity consumption could reduce by 1.4% to 2.8%, leading to billions of dollars in annual savings on electricity bills.

In order to decrease the amount of energy consumed by HVAC systems due to NIR radiation, various transparent NIR shielding products have been studied, including smart windows, glazing coating, and thermal shield fabric. As of 2020[5], the global market for transparent solar filtering (NIR shielding) products was valued at approximately 6 billion dollars, and it is expected to grow at an annual rate of around 9% to reach approximately 10 billion dollars by 2026.

1.1.1 What is NIR?

Near-infrared (NIR) refers to the part of the electromagnetic spectrum that lies immediately adjacent to the visible light spectrum, just beyond the red end of the visible range. NIR wavelengths range from about 700 to 2500 nanometers and are, therefore, invisible to the naked eye. The sun emits a broad spectrum of electromagnetic radiation, including visible, ultraviolet, and near-infrared. About 43% of the sun’s energy is visible light, while the remaining 57% is in the form of other types of radiation, including near-infrared radiation.

1.1.2 NIR shielding mechanism

To remove this invisible energy from solar radiation, several mechanisms exist for the methods in the NIR shielding, including absorption, reflection, scattering, and hybrid ones.

Absorption: Materials can absorb NIR radiation and convert it into heat, reducing the amount of radiation that passes through. Some materials that are effective at absorbing NIR radiation include some forms of metal oxide, such as reduced tungsten or bronze. Due to the localized electron shifting between ions with lattice distorting, NIR photons are coupled and absorbed.[6]

Reflection: Materials can reflect NIR radiation, preventing it from passing through the material. Highly reflective materials such as metals, especially aluminum, and silver, are commonly used for NIR shielding. Some metal oxides, like indium tin oxide (ITO) and vanadium pentoxide (V_2O_5 are commonly considered NIR-reflective rather than NIR-absorbing material. The abundant free electrons on the surface can reflect the NIR radiation if there is enough thickness in the coating of the material.

Scattering: Materials can scatter NIR radiation in many directions, reducing the amount of radiation that passes through. The particles of effective material embedded in glass, polymers, and ceramics can scatter the NIR radiation. Due to the particle's dimensions being close to the wavelength of the visible and NIR light, the geometry features greatly impact the NIR shielding. For example, localized surface plasmon (LSP)[7] is when a surface plasmon is confined within a nanoparticle comparable to or smaller than the wavelength of the light that excites the plasmon. The interaction of a light wave with vibrating electrons at a specific position on the surface of the nanomaterial can explain the phenomenon. The nanoparticle's surface is metallic, which provides localized free electrons in the conduction band that can oscillate when excited by incident light. The frequency of this oscillation is determined by various factors such as electron density, effective electron mass, and size and shape of the charge distribution.[8,9] In this way, the specific NIR wavelength range can be scattered by the particles.

Hybrid: Combining absorption, reflection, and scattering can achieve even greater NIR shielding. For example, some materials are designed with a multilayer structure with a reflective, scattering, and absorbing layer. This hybrid method is the most common for practical products since a single NIR shielding material is limited, which cannot guarantee performance on the whole NIR range. For example, some metal oxide, e.g., ITO, can only shield the NIR in a relatively longer wavelength. However, to achieve an extended shielding range, the other material with the shielding ability for shorter wavelengths, e.g., silver, is applied to combine with the metal oxide coating. In one instance, Chen[10] combines the lamellar structure with noble metal to produce a composited film to shield NIR in an extended range. Layers of Ge and Ag are coated onto transparent media to better shield performance on NIR's full range and transparency for visible light. Another example is that Miao[11] combines the metal oxide, aluminum-doped zinc oxide (AZO), and the noble metal, silver, to form a multilayer structure to gain universal NIR shielding and high transmittance on visible light. Otherwise, shielding NIR is not only by the intrinsic material optical properties but also by the fine geometric features. One brilliant example is the commercial product by 3M company.[12] It combines the one-dimensional photonic crystal film and antimony-doped tin oxide (ATO) to gain NIR shieling on the full range.

1.1.3 NIR shielding materials

Based on the mechanism introduced above, the researchers have investigated various materials for NIR shielding. In Figure 1-1, the species of NIR shielding materials are listed in different types. It can be divided into metal, metal oxide, and metalloid by the element species.

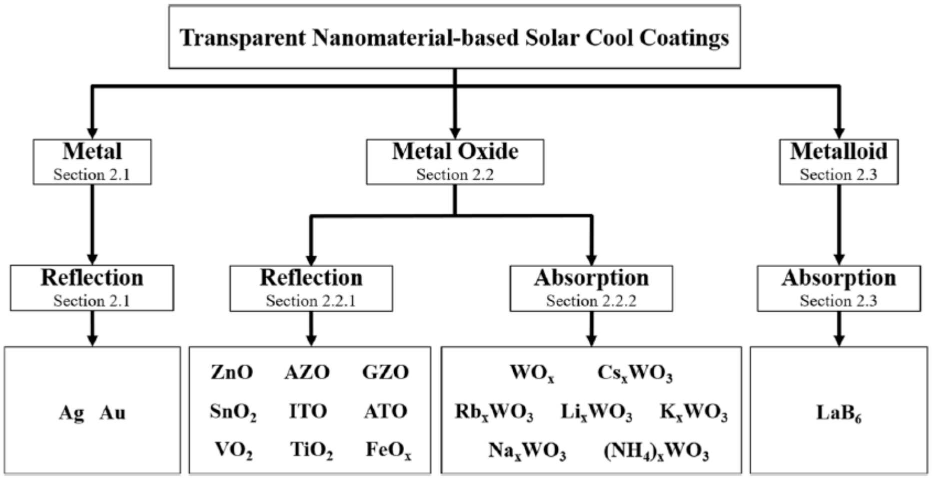

Figure 1-1. Classifications of transparent inorganic Nanomaterial-based Solar Cool Coatings.[13]

Such materials in the above species can be processed into two major statuses for the NIR shielding. One is a fully dense layer/coating of the effective material; the other is a particle-suspended media in which the particle is made of the effective material, and the media is a transparent matrix. Generally, a full dense layer of functional material means a high price because processing such a high quantity of crystalline layer for refractory material is expensive to archive, e.g., commercial ITO-coated glass (usually several dollars per square inch) or sapphire-coated glass (external layer of iPhone screen). Therefore, the most widely applied in practice is the particle-suspended media, which can cover a much larger area with consuming smaller amounts of effective material.

1.1.3.1 Metals

People have used noble metals in transparent coatings for decades for solar heat reflection. Copper (Cu), platinum (Pt), aluminum (Al), gold (Au), and silver (Ag) are common choices. Ag is the superior option due to its high reflectivity and low absorptivity.[14] Due to the properties of LSPR, the shielding range of Ag particles correlates with the particle size (see Figure 1-2). The Ag particle dispersed film is high in reflectivity NIR around ~1000 nm. Therefore, to shield the extended range of NIR, metals must combine the other materials to obtain the general NIR shielding on the whole range, which is one shortage. For another one, due to its high electrical conductivity, metal layer coating on the windows reduces GPS and cell phones' signal strength inside the buildings and autos. The other metal, for example, aluminum, also has the problem of a narrow shielding range, typically between 700 and 1100 nm, and the reflectivity in the NIR region is relatively lower than the silver.

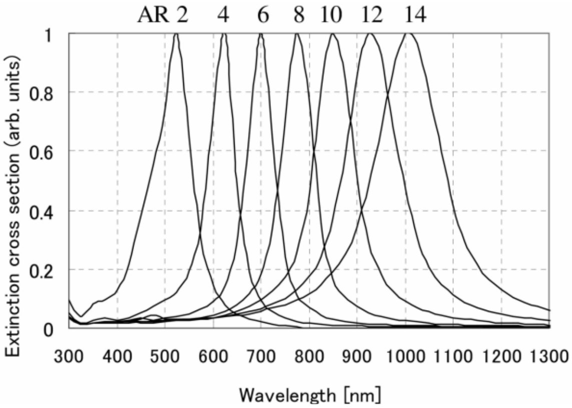

Figure 1-2. Normalized extinction cross-sections of silver nanodisks were calculated for various aspect ratios (AR). The thickness is kept constant at 10 nm, and the AR is varied by changing the diameter.[15]

1.1.3.2 Metal oxides

Due to the high electrical conductivity, some conductive metal oxide nanoparticles can shield NIR by the LSPR effect. Usually, the metal oxide used for NIR shielding includes zinc oxide (ZnO)[14,16–18], aluminum-doped zinc oxide (AZO)[9,11,19–25], gallium zinc oxide (GZO)[26,27], vanadium dioxide (VO_2)[28,29], tin oxide (SnO_2)[30–32], antimony-doped tin oxide (ATO)[29,33–38], indium tin oxide (ITO)[9,14,39–44], iron oxide (FeO_x)[45] and titanium oxide (TiO_2)[28,46]. We can easily find that all such metal oxides are n-type doping semiconductors capable of offering free surface electrons. Due to the local free electrons, their nanoparticles have metallic effects on the surface, reflecting the NIR in a certain range. In some metal oxide optical spectrum data[10,24,32,43,47], the products usually cannot effectively shield the NIR from 780 nm to 1500 nm (some to 2000 nm), which the range is close to the visible part. However, the solar radiation in this range, from 780 nm to 1500 nm, composes about 70% of the entire NIR radiation in solar light. This is a shortage that cannot be neglected.

1.1.3.3 Metalloid

Metalloid lanthanum hexaboride (LaB_6) particles also shield NIR by the LSPR, but it relies on the absorption effect other than the reflection. Also, particle size is the primary influencing factor on the NIR shielding performance. The fine nanosized LaB_6 particles have better shielding performance around the 1000 nm wavelength.[48] However, the very fine particles of lanthanum hexaboride do not show a good shielding performance on the longer wavelength of NIR.

1.1.4 Production methods for NIR shielding materials

Various material processes have been proposed to produce the NIR shielding materials. Such materials processing methods can be divided into bottom-up and top-down approaches. The bottom-up means producing the matter from the basic molecules or atoms, and the top-down is reversed processing. The typical top-down method to produce NIR shielding materials includes sputtering and grinding. And the bottom-up method includes solvo-/hydro-thermal and pyrolysis.

1.1.4.1 Sputtering deposition

Sputter deposition is a physical vapor deposition (PVD) method of thin-film deposition by sputtering. It involves ejecting material from a “target” source onto a “substrate” such as a silicon wafer[95]. People use sputtering deposition on glass coating to produce tinted solar filtering glass. By ion or atom bombardment on the target, the sputtered atoms are ejected from the target and then introduced by the magnetic or electrical field to deposit onto the material surface and form a film layer. Such a method is commonly used for multilayer metal oxide and noble metals like AZO[21,24], ITO, and Ag[10] coatings. The sputtering has the advantage of precise coating thickness control, multi-choices on coating material species, and fast processing time. However, the complex, expensive, and energy-intensive equipment is the shortage of the sputtering method. Also, this technology is can only for newly-produced processing.

1.1.4.2 Grinding

Grinding, paired with other synthesis methods, like fused salt and solid powder reaction, can produce particle material for NIR shielding. Due to the particles’ size being one of the primary influences on NIR shielding performance, the size of the particles produced by the grinding should be fine enough to be effective in the NIR range. It can be seen in the production of LaB_6[48,49] and tungsten bronze[50]. However, the grinding process is time-consuming and energy-costly because most of the motion energy is consumed by the abrasive additives or the particles. Moreover, the impurity induced by the abrasive is another disadvantage of this processing.

1.1.4.3 Solvothermal (or Hydrothermal)

Solvothermal (or hydrothermal) is a branch of techniques to synthesize material in high-temperature and high-pressure conditions. Due to the environment in solvothermal/hydrothermal being very close to the homogenous nucleation condition, crystal particles synthesized by this method are highly consistent with size and composition. Usually, solvothermal/hydrothermal can produce nanocrystals with narrow size distribution and high purity. The reactor of solvothermal/hydrothermal generally can only be operated in batch processing. The reaction time for one batch synthesis of NIR shielding materials, such as TiO_2, ZnO, and tungsten bronze, varies from several to tens of hours. Time-consuming and solvent waste is the shortages for this method when applied for large-scale production.

1.1.4.4 Flame pyrolysis

Flame pyrolysis produces metal oxide powders from the combustion reaction. Atomized precursor solution of the metal salts mixes with the fuel and oxidant gas to combust to form crystalline metal oxide particles. The product particles are synthesized in seconds for total processing by collecting the particle from the flame exhaust. As aerosol processing with high efficiency, flame pyrolysis can easily scale the production rate by increasing the liquid-feed-in speed and flow rate. It is one of the features of aerosol-based synthesis technology.[51] However, controlling the products' consistency is difficult due to the combustion's uncertainty and unstable conditions. The size of particles synthesized by flame pyrolysis is not mono-distributed like the solvothermal-synthesized ones. The large particle in pyrolysis-synthesized powder causes the decline of visible light transmittance.

1.2 Tungsten bronze on NIR shielding

1.2.1 Advantages of tungsten bronze

As one of the hybrid NIR shielding mechanism materials, tungsten bronze (M_xWO_3, M = Li[52], Na[52–56], K[52,54,57–59], Ru[52], Cs[33,60–68], NH_4[69]) can absorb the NIR in the whole range and have a high transmittance on visible light. A typical cesium tungsten bronze's optical spectrum is shown in Figure 1-3. The spectrum curves sharply downturns at the division range (700 ~ 900 nm) between visible and NIR and keeps high absorption at the above 1000 nm range. Otherwise, it has ~80% transmission at ~500 nm. Furthermore, at the longer wavelength range, from ~1500 nm to ~15000 nm, which is deep into the mid-IR and far-IR region, $Cs_{0.32}WO_3$ still has a perfect shielding effect. For now, tungsten bronze's optical properties best meet the requirement for being transparent to visible light and shielding NIR as much as possible.

In comparing multiple NIR shielding materials, including noble metals, metal oxides, lanthanum hexaboride, and tungsten bronze, tungsten bronze can shield the full range of NIR by its dual mechanism. The others need to be composited with the second matter to work on the whole range of NIR shielding. When the tungsten bronze particles are coated on the transparent media, no specific microstructure, like multilayers, is necessary for its work. In some recent research, building models with the coated window can have an indoor temperature 20 to 30 degrees Celsius lower than the ordinary one under the same simulated solar radiation.[70,71]

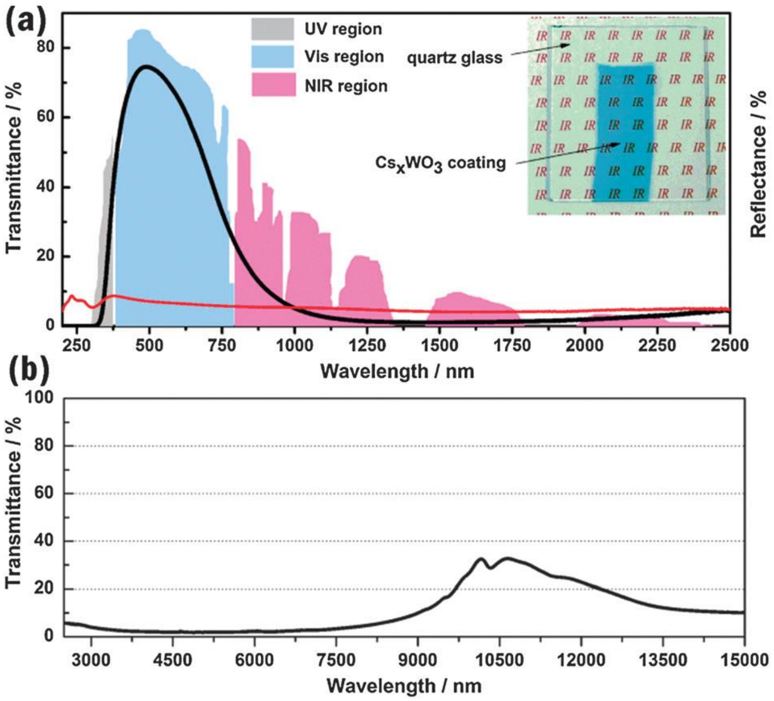

Figure 1-3. (a) Transmittance (black line) and reflectance (red line) spectra of Cs$_{0.32}$WO$_3$ coating. The background shows the relative energy wavelength distribution of the solar spectrum at sea level. Inset shows the picture of Cs$_{0.32}$WO$_3$ film coated on quartz glass. (b) FT-IR spectra of Cs$_{0.32}$WO$_{3.47}$[72].

1.2.2 Methods of the tungsten bronze production

As for the synthesis of tungsten bronze, Table 1-1 summarizes the preparation methods to produce tungsten bronze particles reported in the literature. Among them, the hydrothermal and solvothermal methods are batched and typically require a long reaction time to obtain the desired crystallinity of tungsten bronze particles. In addition to the long reaction time, the solid-phase reaction method requires a grinding/milling post-process which is very energy-intensive and time-consuming. The sputtering coating method has also produced crystalline tungsten bronze particles. The process is again batched and requires sophisticated and expensive equipment.

Table 1-1. Summary of the methods for synthesizing tungsten bronze particles.

Reference	Method	Processing Time

Shanks (1972) [73]	Fused salt electrolysis	Several days
Y. T. Zhu and Manthiram (1994) [74]	Aqueous solution reaction and annealing	5 hours
J. -X. Liu et al. (2010) [67]	Solvothermal reaction and annealing	13 hours
Guo, Yin, Huang, Yang, et al. (2011) [72]	Solvothermal reaction	20 hours
Guo, Yin, Huang, and Sato (2011) [58]	Hydrothermal reaction and annealing	25 hours
Guo, Yin, Yan, and Sato (2011) [66]	Solvothermal reaction	20 hours
Guo, Yin, and Sato (2012) [54]	hydrothermal reaction and annealing	1 hour
Gao and Jelle (2013) [75]	Aqueous solution reaction and hydrothermal	24 hours
J.-X. Liu et al. (2013) [68]	Solvothermal reaction and annealing	13 hours
Luo et al. (2013) [55]	Hydrothermal reaction and annealing	3 days
J. Liu et al. (2014) [63]	Hydrothermal reaction and annealing	3 days
Shi et al. (2014) [60]	Hydrothermal reaction and annealing	3 days
Guo et al. (2015) [76]	Solvothermal reaction	1 hour
J.-X. Liu et al. (2015) [61]	Solvothermal reaction	22 hours
Long et al. (2015) [64]	Electron beam evaporation and annealing	2 hours

Wu et al. (2015)[17]	Solvothermal reaction	20 hours
Zeng et al. (2015)[77]	Aqueous solution reaction and annealing	1 day
Machida and Adachi (2016)[65]	Aqueous solution reaction and annealing	13 hours
Chen et al. (2018)[78]	Aqueous solution reaction and annealing	1 day
Hirano et al. (2018)[62]	Flame-assisted spray pyrolysis and annealing	1 hour
Qi et al. (2019)[71]	Solvothermal reaction	4 hours
Y. Zhu et al. (2019)[70]	Milling and solid-phase reaction	2 days
Linyuan, Mingqing, and Yong (2020)[79]	Hydrothermal & solvothermal reaction	2 days
Nakakura et al. (2020)[80]	Spray pyrolysis & annealing & milling	13 hours
Song et al. (2020)[81]	Grinding & annealing & milling	
Yi et al. (2020)[82]	Solvothermal reaction	20 hours
Chao et al. (2021)[56]	Solvothermal reaction	5 hours
Shen, Ding, et al. (2021)[69]	Solvothermal reaction	1 day
Shen, Wang, et al. (2021)[33]	Solvothermal reaction	1 day
Wang et al. (2014)[83]	Solvothermal reaction	3 days

1.3 Aerosol synthesis of particle materials

1.3.1 Advantages of aerosol synthesis

Aerosol synthesis is a highly effective method for producing high-quality nanoparticles that meet scalability requirements, one-step, toxic-agent-free, size-tunable, rapid, and continuous production. This method generates aerosol particles that react or condense to form the desired nanostructured material. The process can be divided into three main stages: precursor generation, aerosol formation, and particle growth and collection. The precursor material is generated by either chemical reaction or physical vaporization, then converted into an aerosol using nebulization or atomization. The resulting particles are allowed to react or condense to form the desired nanostructured material, which can be controlled by adjusting factors such as reaction temperature, flow rate, and chemical composition of precursor solutions. Aerosol-based processing does not require grinding or additional procedures, thus saving energy consumption. Given these merits, it is significant to investigate the use of aerosol technology to produce tungsten bronze nanoparticles.

The process can be divided into three main stages: (i) precursor generation, (ii) aerosol formation, and (iii) particle growth and collection.

Precursor Generation: In this stage, the precursor material is generated by either chemical reaction or physical vaporization. Depending on the synthesis method, the precursor can be a gas or a liquid. Precursor materials include metal salts, metal-organic compounds, and metal oxide powders.

Aerosol Formation: Once the precursor material is generated, it is then converted into an aerosol by using techniques such as nebulization, atomization, or spray drying. These techniques convert the liquid or solid precursor material into small droplets or particles, then dispersed in a carrier gas, such as nitrogen or helium.

Particle Growth and Collection: Once the aerosol particles are formed, they are allowed to react or condense to form the desired nanostructured material. The particle growth and collection can occur in various ways, such as in a high-temperature furnace, a flame reactor, or a fluidized bed reactor. The final product is collected after the growth process is complete.

Aerosol synthesis has several advantages over other methods for producing nanostructured materials. These advantages include the ability to produce uniform particles with controlled size and shape, the ability to produce a wide range of materials, and the scalability of the process. Additionally, aerosol synthesis can be easily integrated with other processes, such as thin film deposition and printing, making it a versatile tool for nanotechnology research and development

1.3.2 Examples of different aerosol synthesis

Several examples of aerosol synthesis methods have been developed for producing various nanostructured materials. Here are some examples:

Flame spray pyrolysis (FSP)[84]: FSP is a widely used aerosol synthesis technique for producing metal oxide nanoparticles, such as titanium dioxide, zinc oxide, and iron oxide. This method involves combusting a precursor material in a flame, forming aerosol particles that react or condense to form the desired nanostructured material.

Electrospray synthesis (ES)[85]: ES produces nanoparticles from a solution containing a precursor material. It involves electrostatically charging the precursor solution and then applying an electric field to generate an aerosol of charged droplets. The droplets then evaporate and subsequently condense to form nanoparticles.

Nebulized flame synthesis (NFS)[86]: NFS is a method for synthesizing carbon-based nanoparticles. It involves nebulizing a precursor solution and then introducing it into a flame, which is thermally decomposed to form carbon-based nanoparticles.

Aerosol-assisted chemical vapor deposition (AACVD)[87]: AACVD is a process of deposition of thin films and coatings. It involves generating an aerosol of precursor material and transporting it to a substrate surface. The precursor material then reacts or condenses on the substrate surface to form a thin film or coating.

Spray pyrolysis (SP)[88]: SP is a method for synthesizing metal and metal oxide nanoparticles. It involves nebulizing a precursor solution and spraying it onto a heated substrate. The precursor droplets evaporate, react, or condense on the substrate surface to form the desired nanostructured material.

Solution spray pyrolysis (SSP): SSP is an update to the spray pyrolysis method that involves nebulizing a precursor solution and introducing it into a heated reactor tube. The precursor solution then undergoes a series of chemical reactions to form the desired nanostructured material. This method has been used to synthesize various types of nanoparticles, including metal oxides, carbon-based materials, and semiconductor materials.

1.4 Optical modeling of NIR shielding particles

1.4.1 Particle NIR optics

As the fundamental mathematical theory of particle optics, Mie scattering describes how light interacts with spherical particles of different sizes and compositions. The theory is named after the German physicist Gustav Mie, who developed it in the early 1900s.

According to the Mie solution, the scattering and extinction cross-section, each normalized to the particle geometric cross-section α ($\alpha = \pi d^2/4$), can be expressed as

$$Q_s = \sigma_\mathrm{s}/\alpha = \frac{2}{x^2}\sum 2n_\mathrm{p} + 1a_\mathrm{n}^2 + b_\mathrm{n}^2$$

Equation 1-1

$$Q_\mathrm{e} = \sigma_\mathrm{e}/\alpha = \frac{2}{x^2}\sum 2n_\mathrm{p} + 1\mathrm{Re}\ a_\mathrm{n} + \mathrm{Re}\ b_\mathrm{n}$$

Equation 1-2

where $x = (2\pi/\lambda)(d/2)$, d is the particle diameter, λ is the wavelength of the incident wave, and n_p is the order of the multipole expansion of the polarization due to charge oscillation inside the particle. The coefficients a_n and b_n represent the contribution of the multipoles of order n_p. Equation 1-1 and Equation 1-2 show that if the particle diameter were much smaller than the wavelength of the incident light, the scattering or extinction cross-section would decline very fast with the decreasing particle diameter. That means the produced nanoparticles, with a smaller diameter than the NIR wavelength, are naturally weak in NIR shielding.

1.4.2 Modeling on particle optics

The Mie scattering has been utilized to examine the near-infrared (NIR) optics of a single particle through modeling. According to the Mie theory, the refractive index or dielectric function is assumed to be constant and inputted at a specific wavelength. This allows for calculating the extinction cross-section area of a particle with a particular diameter for a given light wavelength. Nonetheless, the Mie scattering incident ray can only be applied to particles with diameters close to the light wavelength. Alternatively, the DDA method[89] has been used to investigate the optical performance of individual particles using the dipole approximation for the object structure, taking into account nanoparticles. This method can simulate the optical characteristics of an individual particle with different shapes, such as spherical, cubic, or cylindrical. However, it also necessitates using the matter's dielectric function as an input parameter.

1.5 Research motivation

1.5.1 Advantages of tungsten bronze on NIR shielding

Various functional materials could be utilized to shield NIR from penetrating through transparent media such as glass. The commercial NIR shielding glass coating includes dielectric-Ag-dielectric films, metal-free solar reflecting films, and functional particles-imbedded film[90]. The dielectric-Ag-dielectric film reflects the NIR by the multiple film structure of Ag and dielectric oxide layers, e.g., indium tin oxide (ITO) and antimony tin oxide (ATO).[91] Ag is applied in the layers because of its unique optical properties [92,93]. Both ITO and Ag are expensive due to their production scale and storage.[90] In addition, the manufacture of dielectric-Ag-dielectric films is by sputtering processing, in which highly precise thickness control of the Ag layer is required since the extra thickness of the Ag layer would result in the dramatic reduction of visible light transmission[90]. Further, due to its high electrical conductivity, an Ag layer could reduce the signal strength of cell phones, GPS, and other wireless devices. The metal-free solar reflecting films' NIR shielding function relies on the refractive index difference of polymer layers.[12] The above films typically have laminated construction with hundreds of layers, and the commercial products of the above films have been applied to the automobile since the early 2000s.[90] However, the irreversible aging of polymer-based films typically occurs because the C-C bond is vulnerable to high-energy UV photons in solar light. In general, the lifespan of a piece of high-quality metal-free solar reflecting film is ~10 years. The above makes metal-free films unpopular in permanent cases such as architectural windows.

Without any special film structure, the other candidates for the NIR shielding are functional-particle-imbedded films. Examples of these functional particles are rare-earth hexaboride (ReB_6, Re = La, Ce, Pr, Nd, and Gd) and tungsten bronze (M_xWO_3 M = Cs, Ru, K, NH_4) in the previous studies.[48,49,54,72,94,95] The performance of rare-earth hexaboride particles is related to the particle size because the NIR absorption is based on the localized surface plasma resonance (LSPR) of conduction electrons.[49] Particles in a certain size range exhibit effective NIR shielding. The wavelength range for shielding NIR is also selective for the above particles.[49,94] Different from the LSPR mechanism, tungsten bronzes (M_xWO_3, M = Li, Na, K, Ru, Cs) particles shield the NIR via the insertion of alkali ion into tungsten oxide crystal lattice to form a solid solution, which is commonly observed in either the cubic or tetragonal crystal phase. Due to the ternary addition of positive ions, free electrons are induced to interact with photons by dipole absorption, which is why general wide-range NIR absorption by tungsten bronze.[96,97] Furthermore, as a family member of tungsten trioxide, tungsten bronze is insoluble in water and all acids except hydro fluoride. That means that tungsten bronze is chemically stable in the room or outside environment.

1.5.2 Issues for tungsten bronze synthesis

In the most popular investigated NIR shielding materials in recent ten years, since the high transmittance on visible light and excellent absorption on the full range of NIR, tungsten bronze is the most promising next-generation solar filtering material. However, commercial tungsten bronze products are far from becoming superior products in the solar filtering market. It is due to the inefficient preparation methods of tungsten bronze. In comparing multiple NIR shielding materials, including noble metals, metal oxides, lanthanum hexaboride, and tungsten bronze, tungsten bronze can shield the full range of NIR by its dual mechanism. The others need to be composited with the second matter to work on the whole range of NIR shielding. When the tungsten bronze particles are coated on the transparent media, no specific microstructure, like multilayers, is necessary for its work. In some recent research, building models with the coated window can have an indoor temperature 20 to 30 degrees Celsius lower than the ordinary one under the same simulated solar radiation.[69]

For the materials processing part, four methods have been applied to produce tungsten bronze, sputtering, solvothermal, grinding, and flame pyrolysis. However, all of them have some shortages. The sputtering method needs high investment in equipment. The solvothermal method has an advantage in product quality but with enormously time-consuming. The grinding method is energy-intensive and easily impurified. The flame pyrolysis method is highly efficient but short in particle properties consistency. So, it is magnificent to have an efficient way to produce tungsten bronze.

1.5.3 Aerosol synthesis of Tungsten bronze particles

For the reasons above, we want to investigate a method with such merits: scalable, one-step, toxic-agent-free, size-tunable, rapid, and continuous, to synthesize high-quality nanoparticles of tungsten bronze for NIR shielding. The aerosol-based method can meet the requirements. The method has been utilized to produce particles from the sub-micrometer to the nanometer size range.[47] Since its continuous operation[98] and product quality reproducibility,[99] an aerosol-based process is considered very suitable for scale-up production. Furthermore, the product's properties vary with the reaction temperature, flow rate, and chemical composition of precursor solutions in aerosol-assistant synthesis.[99] Without grinding processing and after procedures, aerosol-based processing is more saving in energy consumption. Therefore, it is significant to investigate a novel method based on aerosol technology to produce tungsten bronze nanoparticles.

1.5.4 Effect of precursors and solvents

In metal oxide synthesis, the precursor and solvent are the two major impactors for the synthesized product's efficiency and cost. In the synthesis of tungsten bronze, the precursor directly determines the chemical composition of the final product. Otherwise, the species of tungsten bronze mainly differ in the doping cation, including all of the alkali metals, in which sodium, potassium, and cesium are the most common in practice. Thus, further investigation on the precursor is highly valuable to extend the complexity of the aerosol synthesis of tungsten bronze.

Alcohol-based solvents are widely selected in liquid-phase methods to prepare tungsten bronze particles. However, organic solvents are costly and not environmentally benign. Alternatively, DI water can serve as a solvent in preparing tungsten bronze particles in the hydrothermal method[77]. Thus, replacing organic solvents with cheap and environmentally friendly solvents, e.g., water, in the aerosol-assisted method is required to make it more feasible, economical, and environmentally benign for the scale-up preparation of tungsten bronze particles.

1.5.5 Effect of particle size

Most works on tungsten bronze NIR shielding concern the elemental composition and crystal phase effects on shielding performance. However, the particles' size is the primary influence because the LSPR effect is the major contributor to the shielding performance[6]. Therefore, tungsten bronze NIR shielding performance may be more sensitive to particles' size than any other impactors. It is necessary to confirm the correlation between tungsten bronze's particle size and optical properties. Flow operation based on particle size is one feature of aerosol-based processing. Obtaining the desired particle size using the aerosol-based method to synthesize the particle products is much more convenient.

1.5.6 Optical modeling of NIR shielding particles

Although the research on the NIR optics for tungsten bronze particles has been reported, all the modeling works only focused on individual particles, not on an ensemble of particles. In the meantime, NIR shielding particles are randomly suspended in a transparent carry matrix. For a coating of particle-suspended media, the variation of the coating thickness is inevitable, which may make the volumetric packing density in the layer significantly change. The effect of particle packing density on the optics of tungsten bronze particles has not been investigated.

Chapter 2. Experimental setups for the aerosol synthesis of tungsten bronze particles

2.1 Introduction

Wöhler reported the initial synthesis of tungsten bronze via the thermal reduction of fused salts.[100] The thermal reduction method later produced various tungsten bronzes (MxWO3, M = Li, Na, K, Ru, Cs).[101–103] Combining with electrolysis, the high-quality crystal in millimeters of tungsten bronzes with the tuned x in M_xWO_3 were produced.[73,104] The melt salt reaction generally requires high temperatures and produces macro (~ 3 cm) bulk products. However, for the coating applications, micro- or nano-particles are more friendly to the processing (compared with macro products). Grinding large crystals into powder form is expensive in energy and easily contaminated. The wet chemical method has thus been used first to prepare the sol-gel precursor composed of amorphous tungsten oxide and then to obtain the tungsten bronze powder through the thermal hydrogen reduction ($M_{0.33}WO_3$, M = Tl, Rb, Cs).[97] By the time-consuming solvothermal reaction, the nanoparticle of tungsten bronzes (M_xWO_3, M = K, Ru, Cs, NH_4) was directly synthesized at low temperatures.[54,72,95,105] Although multiple methods were proposed to produce tungsten bronze particles, the worldwide production of tungsten bronze powders remains extremely low. The processing methods, including melting salt, powder grinding, hydrothermal, and calcination, are energy costly and time-consuming. Such discontinuous processing is difficult to scale up the production rate.

Aerosol-based processing has produced particles in the sub-micrometer and even nanometer size range.[47] Because of its continuous operation at a high rate,[98] and the high reproducibility for product quality and purity,[99] the aerosol-based process is often considered a conventional method for large-scale nanomaterial manufacturing. Furthermore, the characteristics of particles could be controlled in tube reactors by varying the tube temperature, flow rate, and chemical composition of solutions in aerosol-based synthesis.[99] To make the synthesis of tungsten bronze feasible for future large-scale production, the flame-assistant method was proposed in the work of Hirano[62] for producing cesium tungsten bronze particles. In his report, the precursor can be continuously produced by flame-assistant synthesis. However, another individual annealing remains necessary to promote the crystallinity and eliminate the multiple phases. Further, his work uses cesium as the doping ion in the tungsten oxide. Since the natural abundance of cesium is very low, the price of cesium compound is very high for large scaling producing of NIR shielding materials. So, to make the tungsten oxide bronze feasible for industry-scale production for NIR shielding, a simple one-step method can continuously produce crystallized and monophasic products from cheap raw resources is still a challenge. Also, similar needs are found in electrochromic and gas-sensing nanomaterials, which rely on crystalline tungsten oxide compounds.

This chapter introduces the experimental setups used in the aerosol synthesis of tungsten bronze particles. The prototype, which is the droplet-based process, can efficiently synthesize sodium tungsten bronze particles in a crystalline and single phase. The effect of the particle crystal phase on the optical property was investigated by varying the composition of precursor solutions. The near-infrared absorption property of as-synthesized sodium tungsten bronze nanoparticles in cubic and tetragonal phases was evaluated. Otherwise, the trials on the setups are also included in this chapter, including the different flow configurations and furnace settings.

2.2 Summary of setups in the experiment

2.2.1 Prototype

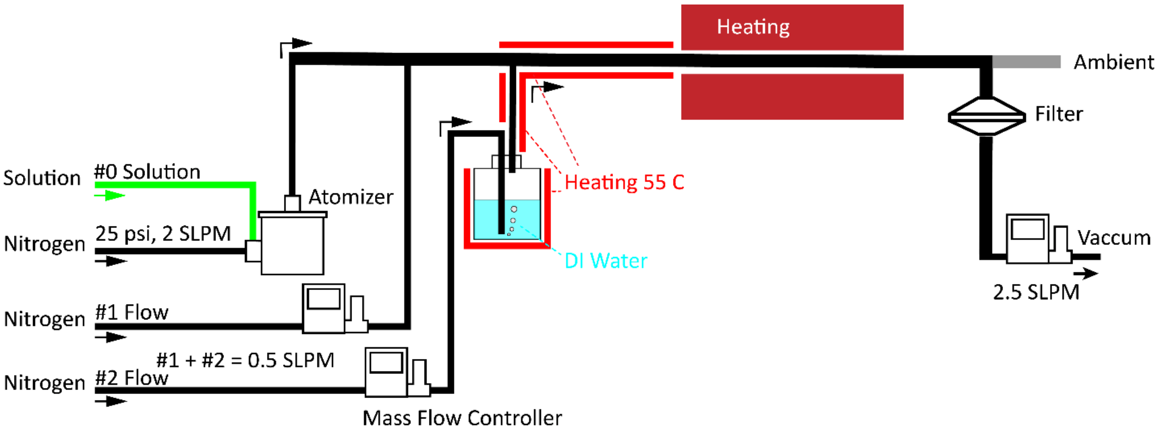

Figure 2-1. Schematic diagram of the experimental setup for producing sodium tungsten bronze nanoparticles. The photo of part of the setup is shown in Figure 0-1 in Appendix.

Figure 2-1 shows the schematic diagram of the experimental setup for preparing sodium tungsten nanoparticles. The system utilized a custom-made Collison atomizer to generate the polydisperse droplets from the precursor solutions. Different from a typical Collison atomizer in which the spray solution is kept in the spray chamber, the spray solution (#0) is fed to the spray nozzle of this atomizer from a syringe driven by a syringe pump (NE-1000, New Era Pump Systems). The compressed N_2 gas was used as the spray and carried flow to operate the atomizer. The pumping rate was set at 300 µL/min. The pressure of nitrogen carrier gas flow was set at 25 psi, resulting in a flow rate of ~ 2 SLPM (Standard Liter Per Minute).

The #0 solution is the mixture of two solutions A and B, in different percentages by volume. Solution A was prepared by dissolving the 7.93 g (0.02 mol) of tungsten chloride (WCl_6, Acros Organics) and the 1.16 g (0.02 mol) of sodium chloride (NaCl, Acros Organics) in 1000 mL methanol (CH_3OH, Alfa Aesar). The above solution was sealed in a bottle for continuous stirring for 3 days (at room temperature). Solution B was prepared in the same process as described without adding sodium chloride. All these solutions are sealed in glass bottles and stored in a chemical closet at room temperature. The molar Na/W ratio of the test #0 solution is summarized in Table 2-1. The #0 solution was transferred to a syringe for the experiments.

Table 2-1. The summary of the Na/W ratio in the precursor solution (#0 in Figure 2-1).

Na/W atomic ratio in #0 solution	1.0	0.8	0.6	0.5	0.4	0.3	0.2	0
Solution A (vol %)	100	80	60	50	40	30	20	0
Solution B (vol %)	0	20	40	50	60	70	80	100

Before entering the high-temperature tube furnace, the produced droplet stream in the atomizer was mixed with two other nitrogen flows (#1 and #2) while keeping the total flow rate of #1 and #2 at 500 SCCM (Standard CC per Minute). The #2 nitrogen flow bubbled through DI water kept in a container to carry water vapor. The DI water container was kept at 55 ^{o}C. At the temperature, the moisture concentration in the #2 flow is 0.23 $g \cdot L^{-1}$. The moisture concentration is measured by weighing the water mass loss in the DI water container at a specific time (1 hour). We assume all the water loss contributes to the flow's moisture concentration. The specific moisture concentration in the total flow under different #1 and #2 flow rates were given in Table 2-2 for reference. Mass flow controllers controlled all the nitrogen flow rates.

Table 2-2. The concentration of moisture in the carry flow at different rates (tested in this study).

#1 Flow rate (SCCM)	500	400	300	200	100	0
#2 Flow rate (SCCM)	0	100	200	300	400	500
Moisture content. in total flow (0.01 $g \cdot L^{-1}$)	0	0.92	1.84	2.76	3.68	4.60

The mixed flow in the total rate of 2.5 SLPM was then directed into a quartz tube placed in a high-temperature tube furnace (LINDBERG 1200C, Thermo Scientific). The retention time for the particle stream in the furnace was estimated at ~10 s. The furnace setting temperature was varied from 350 to 800 ºC. The as-produced particles were collected on a filter medium (Glass fiber filter, Pall Corporation) and placed in a filter holder installed at the exit of the tube furnace. The collection flow rate was 2.5 SLPM via a critical orifice and a vacuum pump. An additional opening line was also included in the setup to ensure the inlet of the filter holder was near the ambient pressure.

To characterize sample particles, the XRD patterns of the particles were measured by X'Pert PRO PANanalytical. The images and EDX spectrum of the samples were taken by Hitachi FE-SEM Su-70. We place a piece of glass slide in the outlet of aerosol flow, just in parallel with the flow, to load the particles for SEM. The XPS spectrum was analyzed by PHI VersaProbe III Scanning XPS Microprobe. The UV-Visible-NIR spectrum was measured by the M-2000 Ellipsometer (J.A. Woollam). The particles are dispersed in collodion/IPA (5 wt%) solution. The concentrations of particles are adjusted to maintain the transmittance at the NIR range equal to each other. Then 5 mL solution is spread onto a 2 in × 2 in glass slide to form a homogenous film. The size distribution of particles was measured by scanning mobility particle sizers (SMPS, TSI model 3080 & CPC 3775).

Note that when using the above setup to produce sodium tungsten bronze particles, the #0 solutions in the Na/W ratio of 1.0 and 0.4 were used since the particle samples under such conditions are just in the mono phase of cubic and tetragonal, respectively. The #2 flow rate was kept at 0.5 SLPM in both cases.

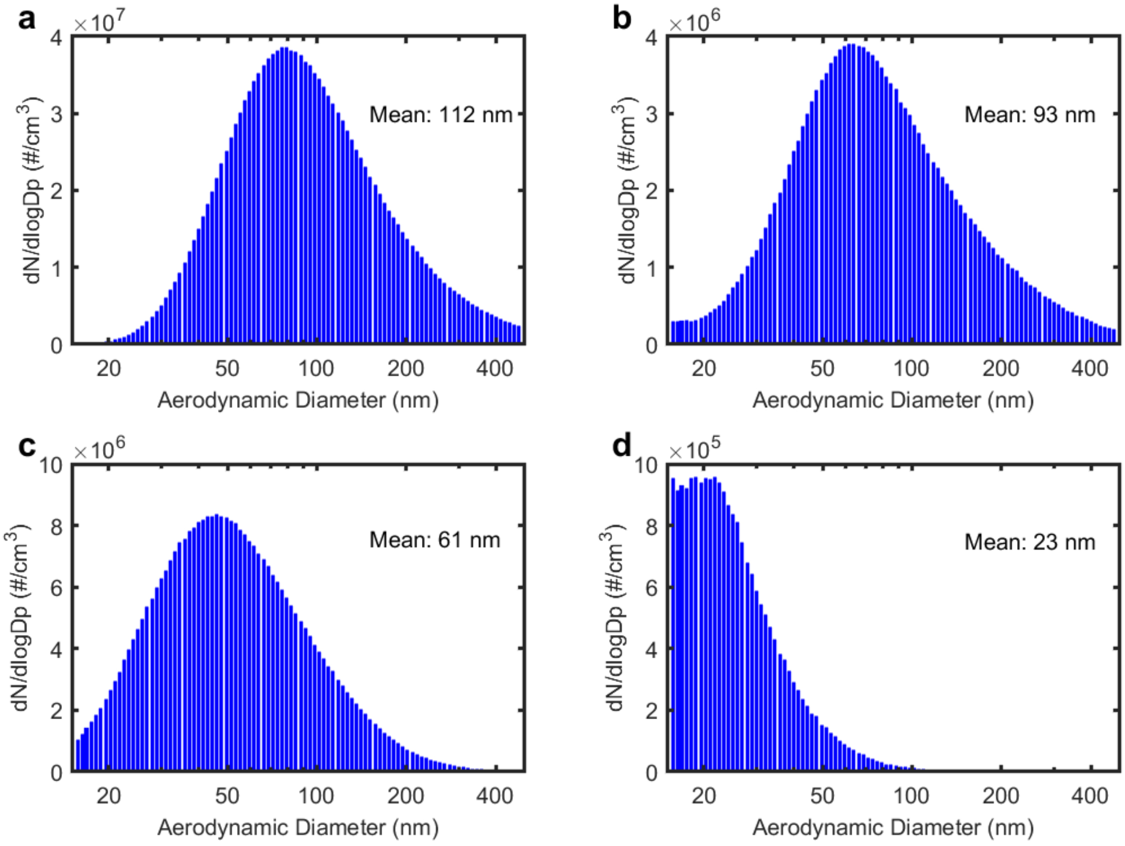

Figure 2-2. Size distributions of particles, measured by SMPS: (a) at the entrance and (b) at the exit of the tube furnace in the case of spraying the precursor solution (#0); (c) at the entrance and (d) at the exit of tube furnace in the case of spraying the methanol only.

To understand how sodium tungsten bronze particles were transformed from droplets produced by the spray, we measured the size distributions of particles before and after the high-temperature tube furnace. In addition to the precursor solutions (i.e., with a salt concentration of only 0.02 M), methanol only was used in this part of the investigation, which serves as both solvent and reduction agent. Figure 2-2a and c show the size distribution of particles prior to entering the tube furnace when spraying the precursor solution and pure methanol, respectively. The difference in the size distributions of particles shown in Figure 2-2a and c represents the particles of salt solute initially dissolved in the precursor solution. Compared to that shown in Figure 2-2c, the size distribution shown in Figure 2-2a has a much higher number concentration and larger peak particle size (although the shape characteristics of both size distributions are similar).

Figure 2-2b and d are the size distributions of particles measured by SMPS after the high temperature when spraying the precursor solution and pure methanol, respectively. Once passing through the furnace, the peak and number concentration of the particle size distribution initially produced by spraying the methanol was significantly reduced (compared with that shown in Figure 2-2c). Moreover, the peak and shape of the particle size distribution initially produced by spraying the precursor solution (shown in Figure 2-2b) slightly changed compared to that in Figure 2-2a, while the number concentration significantly declined. That means the aerosol droplets totally vaporize at high temperatures and then form the sodium tungsten bronze particles as produced because of the dramatic difference between the particle concentration at entering and exiting the furnace.

2.2.2 Setup with the flow stabilizing system

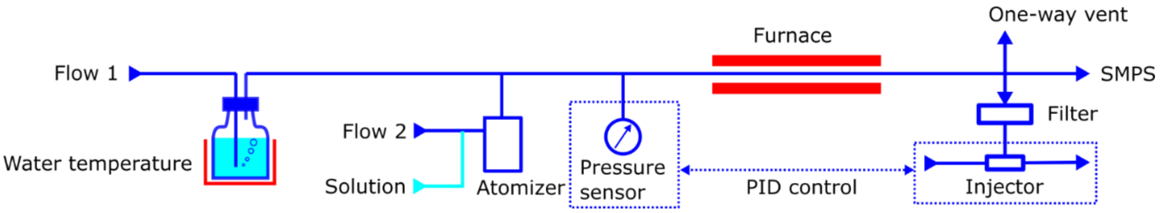

Figure 2-3. Schematic diagram of the experimental setup with PID control to stabilize the flow for producing tungsten bronze nanoparticles.

In particle production, we found that the filter's pressure drop increases with the loading process. The aerosol flow passing through the filter would decline with the increasing pressure drop of the filter. Thus, if the extraction force could compensate for the lost pressure drop, the flow passing through the filter could be maintained stable. Moreover, for the prototype in Figure 2-1, the corrosive byproduct harms the mass flow control on the tail.

Therefore, as shown in Figure 2-3, the PID control with a pressure sensor was added to the setups. Furthermore, the extracting method was replaced by an injector. It could maintain the flow according to the set pressure and feedback to the pressure changing by controlling the input flow on the injector. The injector could offer a higher vacuum with the increased input flow. This way, the system's total flow could be fixed at a configurated value. In Figure 2-3, Flow 1 is 1.0 SLPM, which passes through the water (the water temperature is 60 degrees Celsius) to offer moisture. Flow 2 is 3.0 SLPM injected into the atomizer. Flow 2 carries the precursor solution's aerosol and mixes it with Flow 1 before entering the furnace. The solution can be the precursor to synthesize the sodium, potassium, and cesium tungsten bronze particle, which will be discussed in the next chapter. The filter at the tail collects the produced particles. Also, other collectors can replace the filter, which we will discuss in Chapter 4. The other setups shown in the following text in this dissertation are with the PID controlling system by default, even though the system is not sketched in the schematic.

2.2.3 Setup with a nebulizer to create precursor aerosol

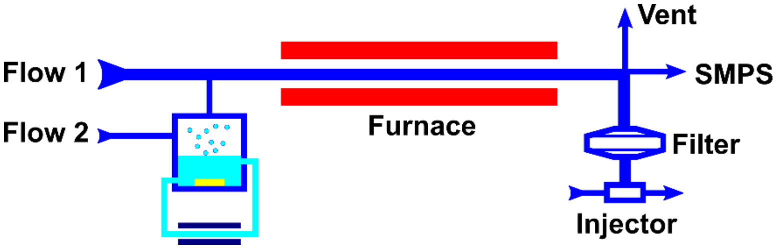

Figure 2-4. Schematic diagram of the experimental setup with a nebulizer as the precursor aerosol creator. (The flow stabilizing system, e.g., PID controlling system, is omitted in this graph. The solvent of the precursor used in this setup is water. The gas of the Flow is composed of 87.5% N_2 *and 12.5%* H_2*.)*

Figure 2-4 shows the setup with the nebulizer as the precursor creator. The nebulizer creates the aerosol by ultrasonic vibration, while the atomizer creates the aerosol by collision. The size distribution by mass of the aerosol droplets created by the nebulizer is mainly in the range of micrometers. It differs from the size distribution created by the atomizer; for example, the size distribution in Figure 2-2 is mainly in the nanoscale. However, the tungsten bronze particles produced by the nebulizer is nearly the same as the particle produced by the atomizer because the furnace temperature can fully vaporize the droplet entering the heating zone. Otherwise, the ultrasonic vibration in the nebulizer could increase the temperature inside the precursor chamber, which may change the properties of the precursor solution. Thus, a cooling system should be attached to the chamber. The photo of the nebulizer is shown in Figure 0-2 in the Appendix.

2.2.4 Setup with a dilution flow system

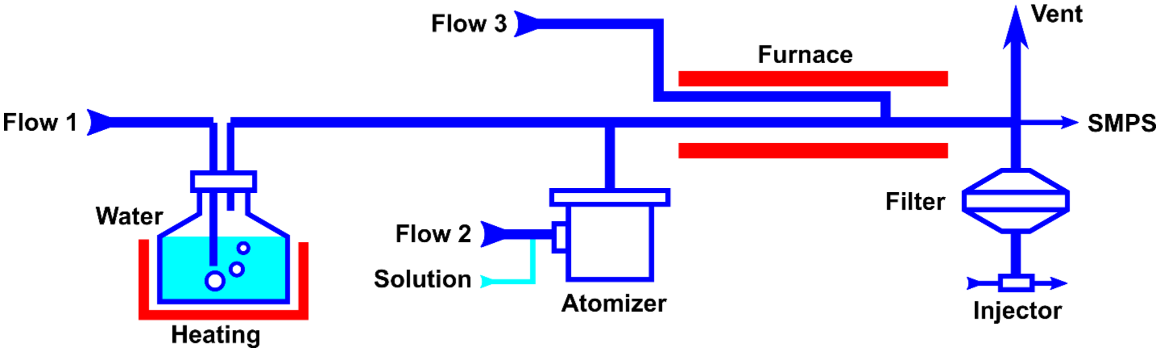

Figure 2-5. Schematic diagram of the experimental setup with dilution flow. (The flow stabilizing system, e.g., PID controlling system, is omitted in this graph. The solvent of the precursor used in this setup is methanol. The gas of the Flow is composed of 87.5% N_2 *and 12.5%* H_2*.)*

Furthermore, to archive the goal of investigating the size effect of tungsten bronze particles on the NIR shielding performance, we introduce the dilution flow into the setup to make the particle size distribution more controllable or find a solution to synthesize the tungsten bronze particle with tuned sizes. As shown in Figure 2-5, a third flow, Flow 3, was introduced in the system. Flow 3 enters the system near the end of the furnace heating zone. Flow 3 is a clear flow to dilute the produced particles to reduce the agglomeration between particles. The other two flows, Flow 1 and Flow 2 act as the same function as in Figure 2-3. Flow 2 (about 2 SLPM) carries the aerosol created by the atomizer. Flow 1 (about 0.5 SLPM) carries the moisture created by the heated water bottle. The produced tungsten bronze particles are collected by a filter at the tail.

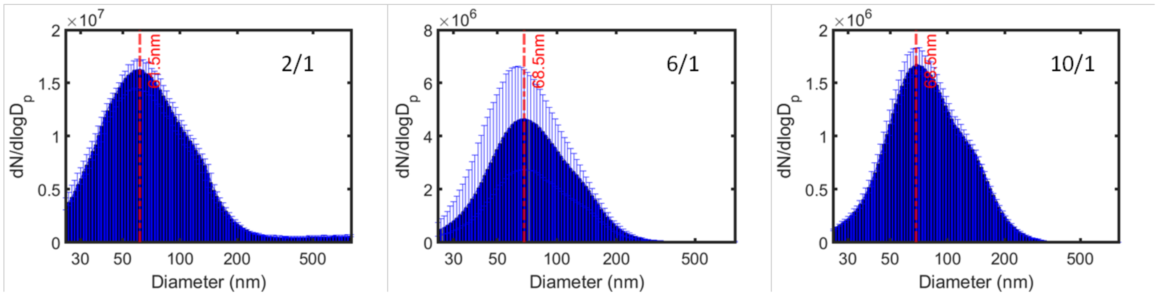

Figure 2-6. Particle size distribution under different dilution flow ratios (dilution flow rate / aerosol flow rate) equal 2/1, 6/1, and 10/1).

Figure 2-15 shows the size distribution of the particles produced under the dilution flow. The ratio of dilution flow to the aerosol flow equals 2/1, 6/1, and 10/1. It is found that the peak size of the particle decreases with the increased dilution flow. It means that the dilution flow declines the agglomeration of the particles. However, the peak size shift is only several nanometers, and the distribution valley also moves little. Therefore, it seems very difficult to change the size distribution only relying on the dilution.

2.3 Conclusion

The setups in this chapter are the major types used in our experiment. The mass flow controllers are used to control the flow rate precisely. The water bottle with heating offers moisture if required in the specific chemical reaction. Pure nitrogen, or the mixture with hydrogen, is used as the carrier gas in the setup. The precursor aerosol creator can be an atomizer or nebulizer, and both two types of the aerosol generator are compatible with the synthesis process. The flow stabilizing system based on PID control has been applied to the setup. The injector replaces the mass flow controller as the controlling extractor to avoid corrosion to the equipment on the tail. The effect of the dilution flow on the size of produced tungsten bronze particles can be observed but is very limited.

For example, a droplet-assisted synthesis process was introduced in the prototype setup to produce sodium tungsten bronze particles in one step continuously. In the process, the precursor solution was atomized and turned into droplets. The droplets carried by the N_2 flow were mixed with the partially saturated N2 flow before entering the high-temperature tube furnace. The produced sample was then collected at the exit of the furnace via the filtration method. Via the measurement of particle size distribution before and after the tube furnace, it is found that the precursor droplet vaporized in the furnace and then formed the crystalline sodium tungsten bronze particle.

Chapter 3. Precursors and solvents for the aerosol synthesis of tungsten bronze particles

3.1 Introduction

This chapter introduces the precursor and solvent used in our study of aerosol synthesis of tungsten bronze particles.

3.1.1 Species of different tungsten bronze species

The tungsten bronze includes several species, separated by the different doping alkali metal ions in the WO_3 crystal lattice. The doping alkali metal ion can be Li, Na, K, Ru, and Cs. In such species, cesium tungsten bronze (Cs_xWO_3) is the most frequently researched in many studies. However, due to the limited abundance of cesium on the earth, the price of such material containing cesium may be very high if widely applied. Thus, tungsten bronze with doping ions such as Na and K is valuable for investigating better NIR shielding performance.

Not only the chemical composition of doping alkali metal ions but also the multiple crystal phases exist for tungsten bronze. Because of the different distortions caused by the doping in the WO_3 lattice, a specific chemical composition of tungsten bronze can have several different crystal structures, e.g., the tetragonal and cubic phases of sodium tungsten bronze.

3.1.2 Precursor and solvents in the synthesis of tungsten bronze

For the precursor and solvent in the aerosol synthesis of tungsten bronze, the previous research on tungsten bronze preparation can anticipate the chemical reaction in aerosol synthesis. For tungsten bronze synthesis with a precursor, such as hydrothermal and solvothermal methods, the hydrolysis and reduction processes happen in the formation of tungsten bronze. Table 3-1 shows that the combination of salts containing alkali or tungsten and a reductive regent is the common solution for the tungsten bronze synthesis in previous studies. Therefore, such a combination would be similar and can be processed into aerosol or gas status. The homogeneity of regents in precursor solution is a high requirement for the reaction in the aerosol or gas. So the solubility of such salt regent should be enough in the precursor solvent.

Table 3-1. Summary of the precursor for preparing tungsten bronze particles.

Reference	Precursor
Y. T. Zhu and Manthiram (1994) [74]	$NaBH_4$, Na_2WO_3, aqueous solution
J. -X. Liu et al. (2010) [67]	WCl_6, CsOH, ethanol aqueous solution
Guo, Yin, Huang, Yang, et al. (2011) [72]	WCl_6, CsOH, ethanol solution
Guo, Yin, Huang, and Sato (2011) [58]	K_2WO_4, K_2SO_4, aqueous solution
Guo, Yin, Yan, and Sato (2011) [66]	WCl_6, CsOH, ethanol solution
Guo, Yin, and Sato (2012) [54]	$NaBH_4$, Na_2WO_3, aqueous solution

Gao and Jelle (2013) [75]	Na_2WO_3, Na_2SO_4, oxalic acid aqueous solution
J.-X. Liu et al. (2013) [68]	WCl_6, CsOH, ethanol solution
Luo et al. (2013) [55]	Na_2WO_4, HCl, citric acid, aqueous solution
J. Liu et al. (2014) [63]	Na_2WO_4, Cs_2CO_3, citric acid, aqueous solution
Shi et al. (2014) [60]	Na_2WO_4, Cs_2CO_3, citric acid, aqueous solution
Guo et al. (2015) [76]	WCl_6, oleylamine, oleic acid solution
J.-X. Liu et al. (2015) [61]	WCl_6, CsOH, ethanol solution
Wu et al. (2015) [17]	WCl_6, CsOH, ethanol solution
Zeng et al. (2015) [77]	WO_3, Cs_2CO_3, powders
Machida and Adachi (2016) [65]	Cs salt and W salt
Chen et al. (2018) [78]	WO_3, Cs_2CO_3, powders
Hirano et al. (2018) [62]	$(NH_4)_{10}(W_{12}O_{41})5H_2O$, Cs_2CO_3, aqueous solution

Qi et al. (2019) [71]	WCl_6, CsOH, benzyl alcohol solution
Linyuan, Mingqing, and Yong (2020) [79]	H_2WO_4, $CsSO_4$,
Nakakura et al. (2020) [80]	$(NH_4)_{10}(W_{12}O_{41})\cdot 5H_2O$, Cs_2CO_3, aqueous solution
Yi et al. (2020) [82]	WCl_6, CsOH, ethanol solution
Chao et al. (2021) [56]	NaOH, WCl_6, benzyl alcohol solution
Shen, Ding, et al. (2021) [69]	$(NH_4)_6H_2W_{12}O_{40}\cdot aH_2O$, Cs_2CO_3, tartaric acid, ethanol solution
Shen, Wang, et al. (2021) [33]	WCl_6, CsOH, ethanol solution
Wang et al. (2014) [83]	$(NH_4)_2WO_3$, $(NH_4)_2MoO_3$, ethylene glycol solution

3.2 Effect of precursor and solvent

According to the requirements mentioned above, the combinations of regent in our precursor are MCl (M = Na, K, Cs) and WCl_6 with alcohols (methanol or ethylene glycol) solvent, or MCl (M = Na, K, Cs) and $(NH_4)_2WO_3$ with water solvent. Because tungsten chloride (WCl_6) has a relatively high solubility in methanol (MeOH) and ethylene glycol (EG), while alkali chloride, MCl (M = Na, K, Cs), also has a considerable solubility in MeOH or EG. For MCl (M = Na, K, Cs) + $(NH_4)_{10}H_2(W_2O_7)\cdot xH_2O$ + water, the situation is almost the same as the former combination. The difference is that a reductive regent, hydrogen, is required in the synthesis. Additionally, water as the solvent is cheaper and more environmentally friendly.

3.2.1 Doping alkali metal ions in the aerosol synthesis of tungsten bronze particles

By adding the different alkali chloride salt into the precursor solution, we can obtain the different species of tungsten bronzes, including the Na_xWO_3, K_xWO_3, and Cs_xWO_3. Figure 3-1, Figure 3-2, and Figure 3-3 display the XRD pattern of the three produced species of tungsten bronze. From the XRD patterns in those figures, it can be found that there are few peaks of byproducts, which can prove the quality of the produced tungsten bronzes. Moreover, such results can be obtained by different combinations of precursors and solvents.

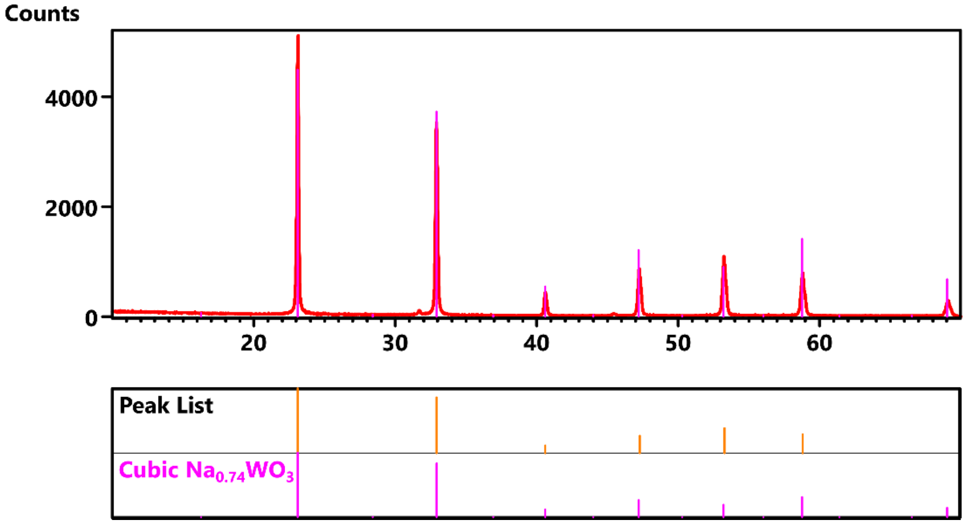

Figure 3-1. XRD pattern of produced cubic sodium tungsten bronze particles.

As shown in Figure 3-1, the sodium tungsten bronze particles in the cubic phase are synthesized by precursor, the aqueous solution dissolving NaCl and $(NH_4)_{10}H_2(W_2O_7)\cdot xH_2O$. Also, similar sodium tungsten bronze particles are produced via another precursor, which solvent is methanol or ethylene glycol. The XRD patterns of sodium tungsten particles synthesized through the methanol-based precursor are shown in Figure 3-10. It also shows negligible byproducts in the samples. The ratio of the doping element, sodium (Na), to the tungsten (W) is about 0.7 in the precursor solution for both cases.

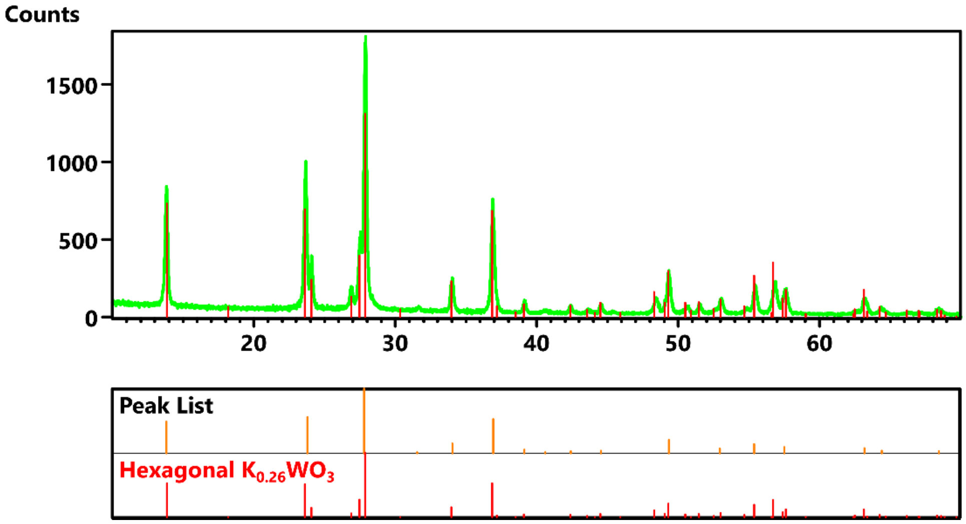

Figure 3-2. XRD pattern of produced hexagonal potassium tungsten bronze particles.

Figure 3-2 shows the XRD pattern of produced potassium tungsten bronze particles. It also shows a high quality for little byproduct exists in the sample. Moreover, the atomic ratio of potassium to tungsten is about 0.3 in the precursor solution, which is KCl and $(NH_4)_{10}H_2(W_2O_7)\cdot xH_2O$ aqueous solution. If the synthesis was undergone through other solvents, e.g., ethylene glycol, the ratio K/Cl is also about 0.3 with the same product.

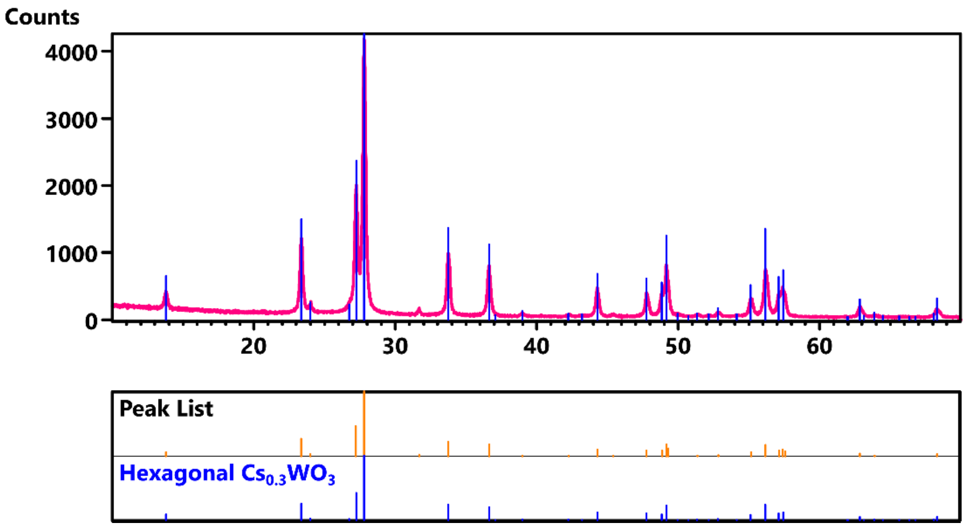

Figure 3-3. XRD pattern of produced hexagonal cesium tungsten bronze particles.

Figure 3-3 shows the XRD pattern of produced cesium tungsten bronze particles. It also shows high quality, like those in Figure 3-1 and Figure 3-2. The atomic ratio of cesium (Cs) to tungsten (W) is about 0.3 in the precursor, which is a water-based solution dissolving CsCl and $(NH_4)_{10}H_2(W_2O_7)\cdot xH_2O$. The same result could be obtained under the same ratio of Cs/W for the synthesis via other solvents.

In our study's aerosol synthesis of tungsten bronze particles, the doping alkali ion species directly result in a specific species of tungsten bronze. Even within different precursors and solvents, a specific atomic ratio of M/W (M = Na, K, Cs) can produce a stable result with high quality.

3.2.2 Chemical reactions with methanol as the precursor solvent

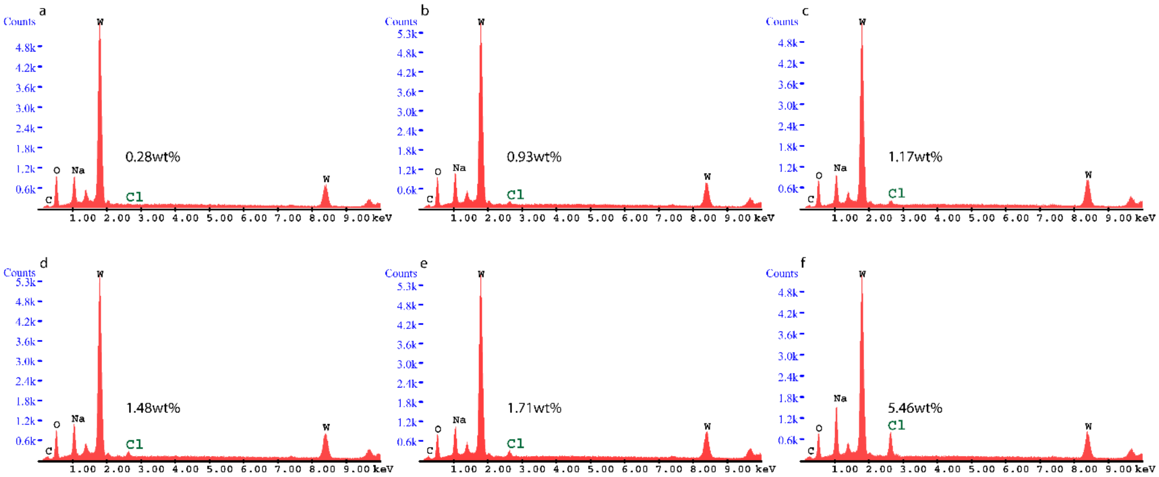

Figure 3-4. EDX data of sample particle products obtained at the moisture flow rate (#2 in Fig. 1)) of (a) 500, (b) 400, (c) 300, (d) 200, (e) 100, and (f) 0.0 SCCM. The tube furnace temperature was at 800 °C. The Na/W ratio is kept at 1.0.

When methanol serves as the precursor solvent, it also acts as the reductive regent. Due to the hydrolyzing process in the reaction, it requires water/moisture in the synthesis. Thus, there is a water/moisture source in the setup for the methanol solvent, for example, the ones in Figure 2-1 and Figure 2-5. Figure 3-4 shows the EDX data of sample products obtained through the setup in Figure 2-1, under the various flow rates (#2) passing through the DI water bottle. The series of EDX data evidence that the chlorine in the sample products increases from 0.28 wt% to 5.46 wt% with the decrease of the moisture concentration (via the decrease of #2 flow rate). Based on the above finding, the entire reaction in the tube reactor could be expressed in the following Equation 3-1:

$$WCl_6 + xNaCl + \frac{x}{6}CH_3OH + \left(3 + \frac{x}{6}\right)H_2O \rightarrow Na_xWO_3 + \frac{x}{6}CO_2 + (x+6)HCl$$

Equation 3-1

In Equation 3-1, the WCl_6 hydrolyzes with H_2O to form tungsten oxide in the presence of Na^+. Since the Na^+ atom is smaller than the void in the ReO_3 lattice of tungsten oxide, the sodium can easily diffuse into the lattice. According to the reaction, when there are no sufficient water molecules, the reaction would result in additional chloride salt residue. As shown in Figure 3-4, the chlorine weight percentage increases with the moisture flow rate (#2 in Figure 2-1) decreases. Additionally, because the methanol is strongly reductive, it reduces the tungsten from VI valence to lower ones such as V or IV, similar to the hydrogen thermal reduction in other previous works[62]. The difference between our work and the previous ones is using methanol as the solvent and the reductant.

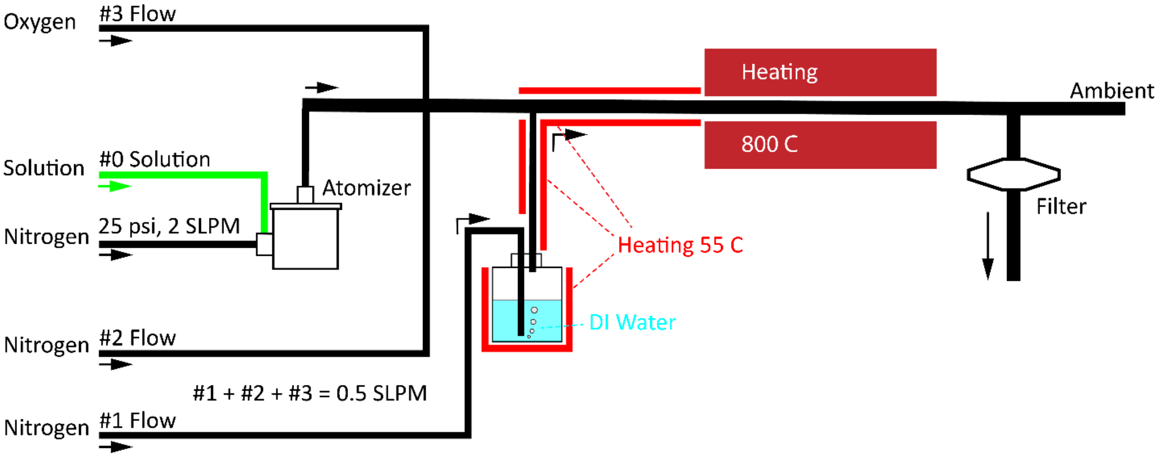

Figure 3-5. The schematic diagram of the experimental setup for verifying the reductive role of methanol used in the process.

To investigate the reductive effect of methanol, the oxygen flow rate was added to mix with the particle flow before entering the tube furnace (Figure 3-5). Introducing oxygen will reduce the reductivity of the reacting flow, preventing the W (VI) from being reduced to the lower valence. Figure 3-6 shows the XRD data of particle samples using the precursor solutions in different Na/W ratios in the setups (in Figure 3-5). It is observed that the metal state of tungsten always presents in the sample products obtained using precursor solutions of various Na/W ratios when there is ~8% oxygen in the total flow rate, and no crystal structure in the products were observed when the oxygen percentage is above or below 8%. The above finding indicates that the redox potential of methanol is not sufficient to reduce the W (VI) to the metal state (0). Alternatively, the redox potential of intermediates might be capable. We hypothesize the intermediate is formaldehyde, whose redox potential is higher than methanol[106]. Under a certain low concentration, the oxygen partially oxidizes methanol into formaldehyde. The W (VI) could thus be reduced to the metal state by the formaldehyde. It is concluded that methanol is a good candidate for serving as the solvent and reducing agent in the studied synthesis of sodium tungsten bronze because it can reduce the W (VI) to W(V) or W (IV) without over-reduction.

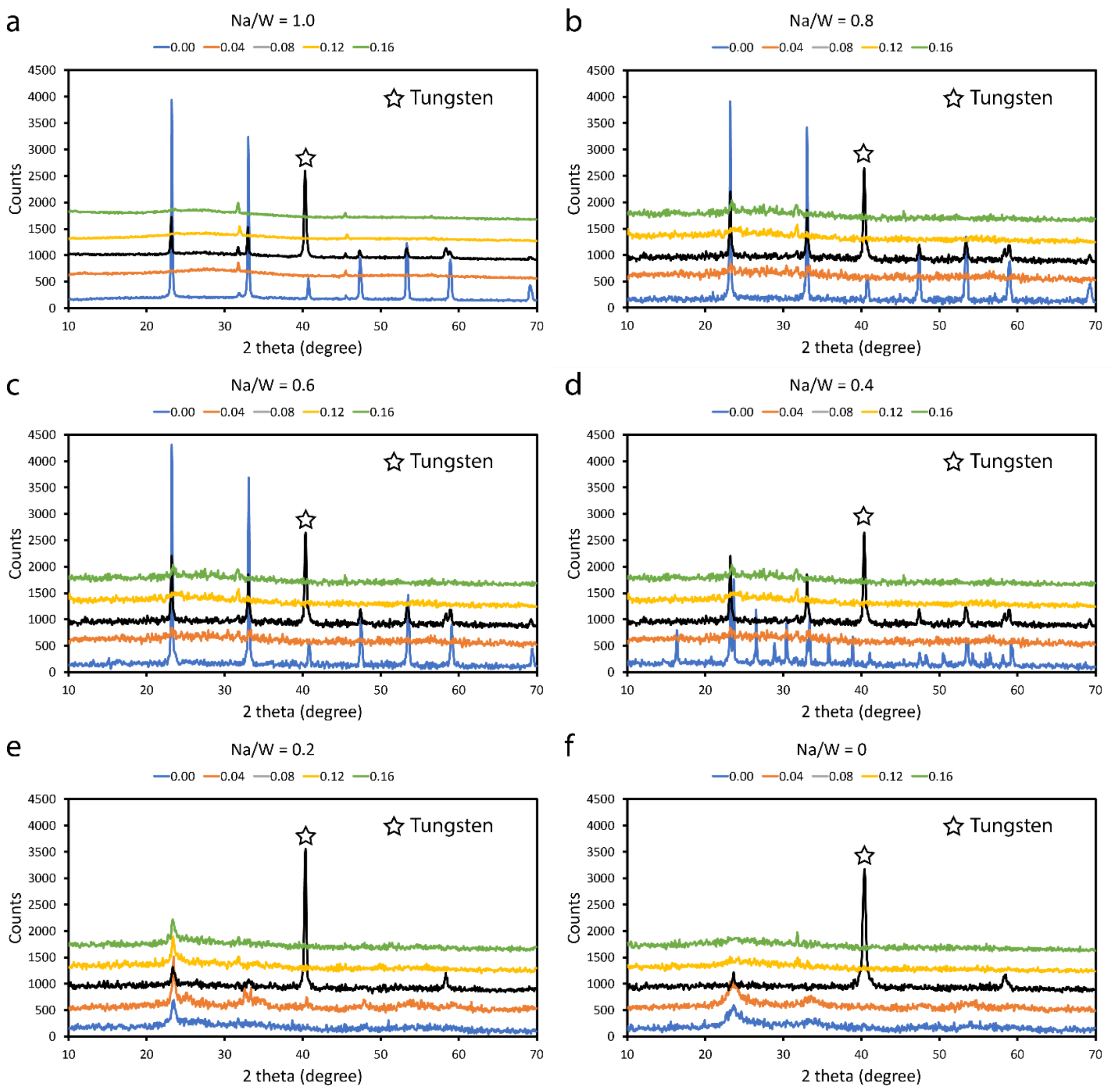

Figure 3-6. Powder-XRD data of the particle products obtained when spraying the precursor solutions with the Na/W ratio of (a) 1.00, (b) 0.80, (c) 0.60, (d) 0.40, (e) 0.20, and (f) 0.00, and under the oxygen volume ratio in total flow was 0.00, 0.04, 0.08, 0.12 and 0.16.

Based on the result and hypothesis above, we try to synthesize the other species of tungsten bronze using methanol as the solvent. However, we found that: (1). The mole solubility of KCl in methanol is much smaller than NaCl, which makes the methanol not proper as the solvent for KCl; (2) The CsCl is soluble in methanol, but the solution breaks the stability when the WCl_6 was mixed into the methanol solution, to form precipitation with pink color. Therefore, the methanol solution cannot serve as a solvent for the precursor in potassium and cesium tungsten bronze synthesis.

3.2.3 Chemical reactions with ethylene glycol as the precursor solvent

As another choice of an alcohol solvent, ethylene glycol (EG) can dissolve considerable amounts of NaCl, KCl, and CsCl. Additionally, the solubility of WCl_6 is high enough (nearly as high as 0.5M for the highest mole concentration) in EG. Thus, EG can be a solvent for the three precursors in synthesizing sodium, potassium, and cesium tungsten bronze. Similarly, EG is a reductant like methanol, so the reaction can be listed below.

$$WCl_6 + xMCl + \frac{x}{10}C_2H_4(OH)_2 + (3 + \frac{2}{10}x)H_2O \rightarrow M_xWO_3 + \frac{2x}{10}CO_2 + (x + 6)HCl$$

Equation 3-2

When the precursor solvent is EG, we used the setup shown in Figure 2-3 for the synthesis. The flow configuration is just described in Setup with the flow stabilizing system. The precursor solution can be pumped into the atomizer to generate the aerosol flow. The injection rate for the precursor solution into the atomizer is about 15 µL/min. The concentration of WCl_6 in the EG solution can be as high as 0.5 M. The Na/Cl, K/Cl, and Cs/Cl atomic ratios are 0.7, 0.3, and 0.3, respectively, the same as the methanol cases. The furnace temperature is 750 °C.

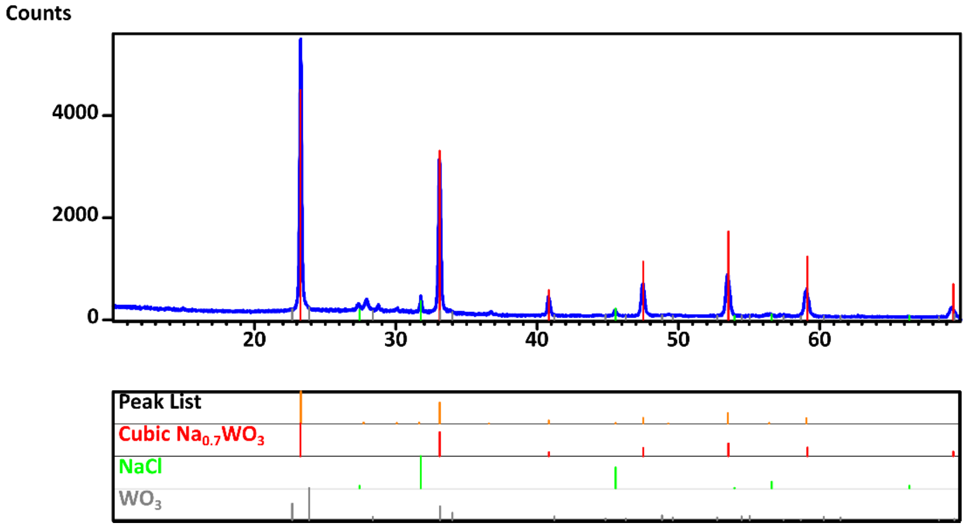

Figure 3-7. XRD pattern of produced cubic sodium tungsten bronze particles via EG-based precursor.

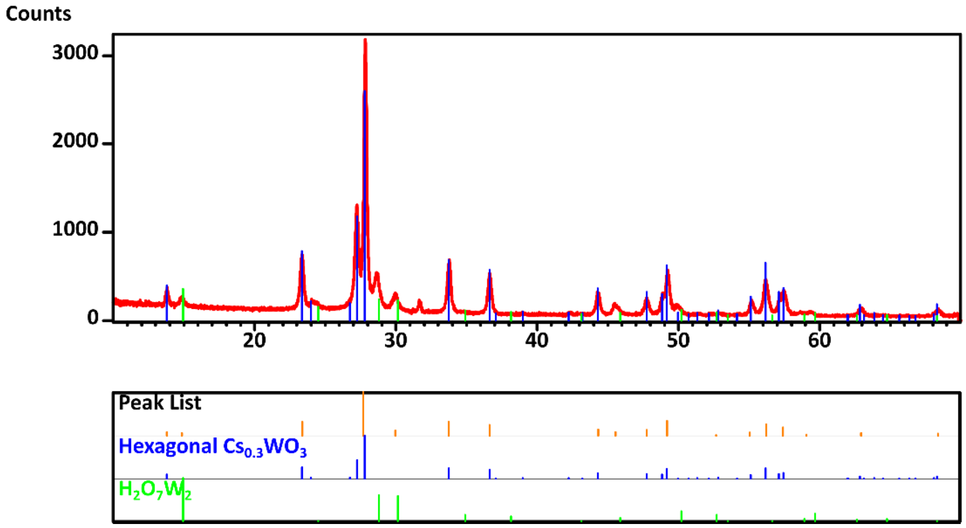

Figure 3-8. XRD pattern of produced hexagonal cesium tungsten bronze particles via EG-based precursor.

Figure 3-7 shows the XRD patterns of produced sodium tungsten bronze particles. While Figure 3-8 shows the one for cesium tungsten bronze particles. From both two results, it can be found that byproducts like NaCl, WO3, and $H_2O_7W_2$ (a hydrate of WO_3) exist in the samples. Compared with the cases of methanol (XRD of Na_xWO_3 in Figure 3-10) or water-based precursor solution (XRD of Na_xWO_3 in Figure 3-1 and Cs_xWO_3 in Figure 3-3), the product via EG-based precursor has more impurities than the methanol-based and water-based. Because of the high viscosity and high boiling point of EG solution, EG-based precursor solution is more difficult to be atomized into aerosol and needs a longer time to be fully vaporized. All those would cause the incompletion of the reaction and leave more impurities in the product. So obtaining the product with the same quality as methanol or water-based precursor may require more reaction time for EG-based precursor in the aerosol synthesis of tungsten bronze particles.

3.2.4 Chemical reactions with water as the precursor solvent

Water, a cheap and environmentally friendly solvent, is our target precursor solvent in our study. The source of tungsten, ammonium paratungstate ($(NH_4)_{10}H_2(W_2O_7)\cdot xH_2O$), and alkali chloride (MCl, M = Na, K, Cs), both are soluble in the aqueous solution. The atomizers and nebulizers designed for the aqueous solution are widely manufactured and applied. Thus, a water-based precursor solution can be flexible with different aerosol generation devices. The experiments conducted via the setup in Figure 2-4 and Figure 2-5 have water as the precursor solvent. Hydrogen is required to act as the reductant in the reaction. The reaction for the aerosol synthesis of tungsten bronze particles via water-based precursor can write below. (M = Na, K, and Cs)

$$(NH_4)_{10}H_2(W_2O_7)_6 \cdot xH_2O + 6yH_2 + 12yMCl \\ \rightarrow 12M_yWO_3 + (x+6)H_2O + 10NH_3 + 12yHCl$$

Equation 3-3

As shown in Figure 3-1, Figure 3-2, and Figure 3-3, the produced Na_xWO_3, K_xWO_3, and Cs_xWO_3 all come from the precursor in an aqueous solution. The little byproducts shown in the XRD patterns demonstrate the ability to produce high purity and crystallinity of tungsten bronze particles.

Furthermore, more details of the water-based synthesis of sodium tungsten bronze particles also be discussed in Chapter 4, which includes the formation of the particle in different sizes via the water-based precursor solution.

3.2.5 Effect of M/W (M = Na, Cs) ratio in the precursor solution

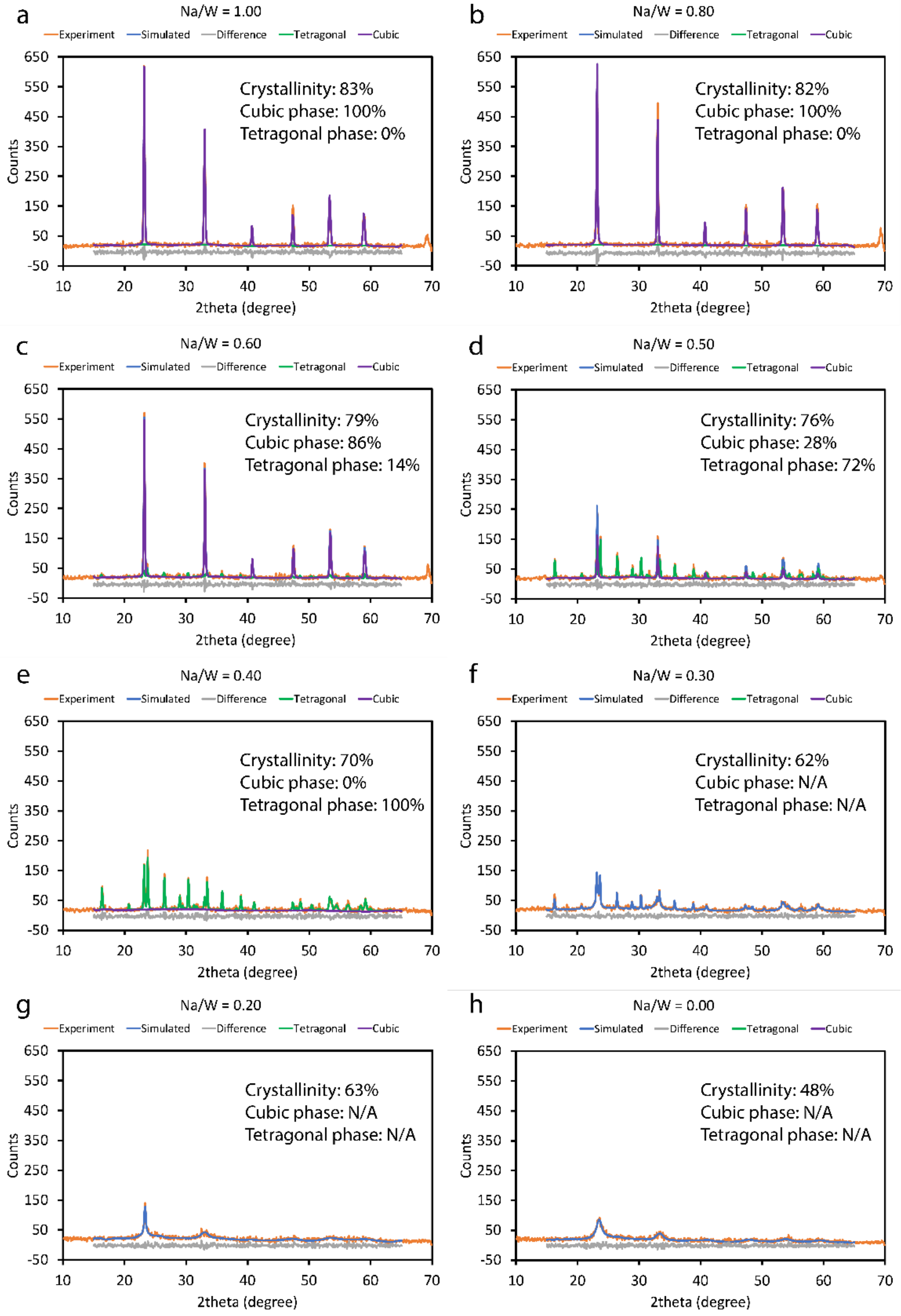

Figure 3-9. Comparison of the experimental and simulated patterns of powder-XRD for the sample products obtained when spraying the precursor solutions with the Na/W ratio of (a) 1.00; (b) 0.80; (c) 0.60; (d) 0.50; (e) 0.40; (f) 0.30; (g) 0.20 and (h) 0.00. The sample in (a) and (e) are cubic phase and tetragonal phase, specifically.

To study the effect of the Na/W ratio on the crystal phase and crystallinity of the products, the XRD data of powder samples obtained in the cases of spraying precursor solutions (#0 in Figure 2-1) in different Na/W ratios were analyzed by the XRD simulation. The sample products under the analysis were obtained at the furnace temperature of 800 ºC, while the highest temperature inside the furnace tube was 853 ºC. Figure 3-9 compares the simulated and measured XRD data of sample products. It is found that, with the decrease of the Na/W ratio in the precursor solution, the percentage of the sample in the cubic phase is decreased, and the percentage in the tetragonal phase is increased. Because the sodium atom acts as the padding material inside the scaffold of WO_3 to support the structure (i.e., with sodium atoms occupying the vacancy of the ReO_3 structure of WO_3), the crystal lattice tends to form in the cubic phase. On the contrary, with fewer sodium atoms, the crystal lattice of WO_3 tends to collapse to form in the tetragonal phase. Pure WO_3 could often form in the tetragonal phase at room temperature.[107] Specifically, when the Na/W ratio in the solution is larger than 0.8, only the pure cubic phase was found in the sample products because the measured XRD patterns in Figure 3-9a and b are well fit by the simulated ones in the cubic phase. On the other hand, when the Na/W ratio is reduced to 0.40, the sample powder is all in the tetragonal phase (Figure 3-9e). As the Na/W ratio in the precursor solution further reduced, the crystallinity of product samples dramatically decreased, and the phase composition analysis became not applicable (Figure 3-9f, g, and h). The above observation is out of our expectation that crystalline tungsten oxide particles should be synthesized without sodium chloride. It suggests that the formation of crystalline Na_xWO_3 particles relies on the catalyzing by a sodium ion. Since sodium chloride's melt point (801 ºC) is much lower than tungsten oxide (1473 ºC), sodium chloride acts as the ceramic flux to facilitate tungsten atoms' movement and lattice conversion via liquefaction.[108,109] Without the sodium chloride, the amorphous tungsten oxide product requires much time to form the crystal at the same 800 °C.[97]

3.2.6 Comparison of sodium tungsten bronze products in phases

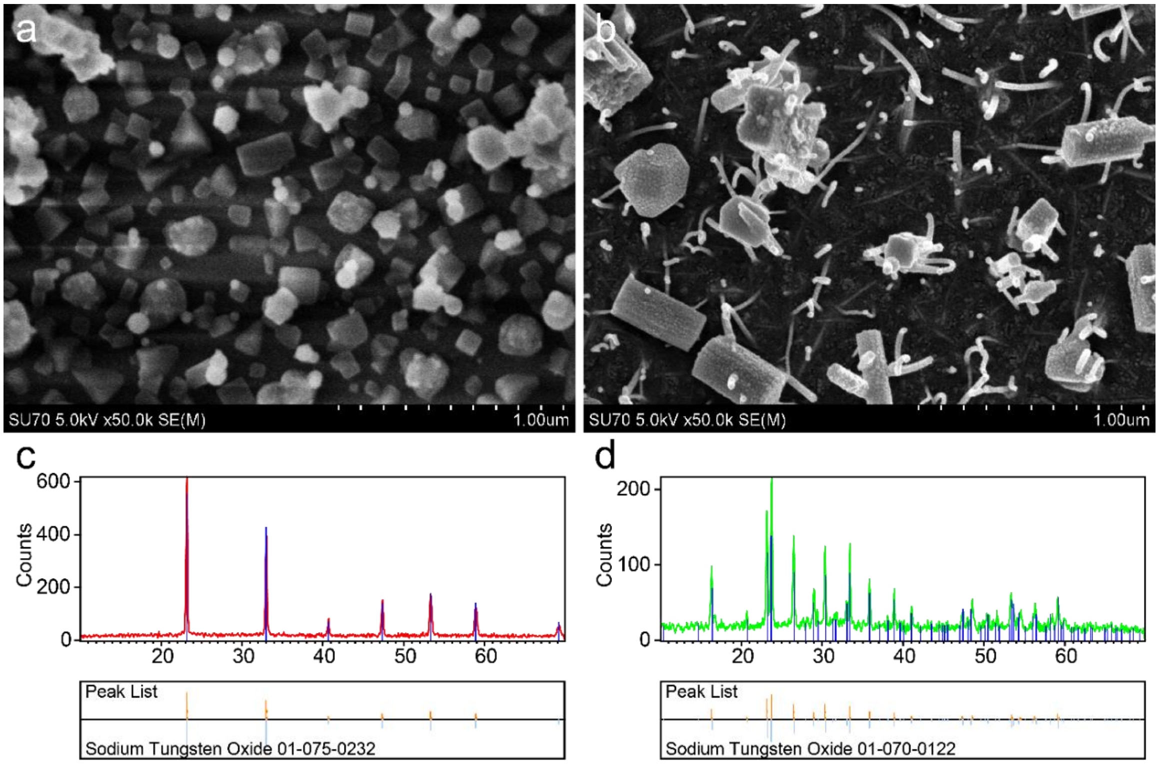

Figure 3-10. SEM images and XRD data of sodium tungsten bronze particle samples in the cubic phase (a, c) and tetragonal phase (b, d), respectively.

To investigate sodium tungsten bronze particles in two phases, the micro morphologies of sodium tungsten bronze in the cubic and tetragonal phases are shown in Figure 3-9a and b, respectively. The cubic shape (Figure 3-9a) and the orthogonal bar shape (Figure 3-9b) of sample particles match well with the crystal lattice types of two typical samples. From the powder-XRD patterns in Figure 3-9c and d, it is found that all the peaks of the samples in both the cubic and tetragonal phases correspond very well with the reference positions of ICDD PDF 01-075-0232 and 01-070-0122. The sharp peaks indicate the excellent crystallinity of the samples. The cubic phase sodium tungsten bronze has a much high intensity of the peaks above the background, which is evidence of better crystallinity than the tetragonal phase bronze. More, the calculated crystallinity of pure cubic and tetragonal phases of sodium tungsten bronze in Figure 3-9a and e are 83% and 70%, respectively.

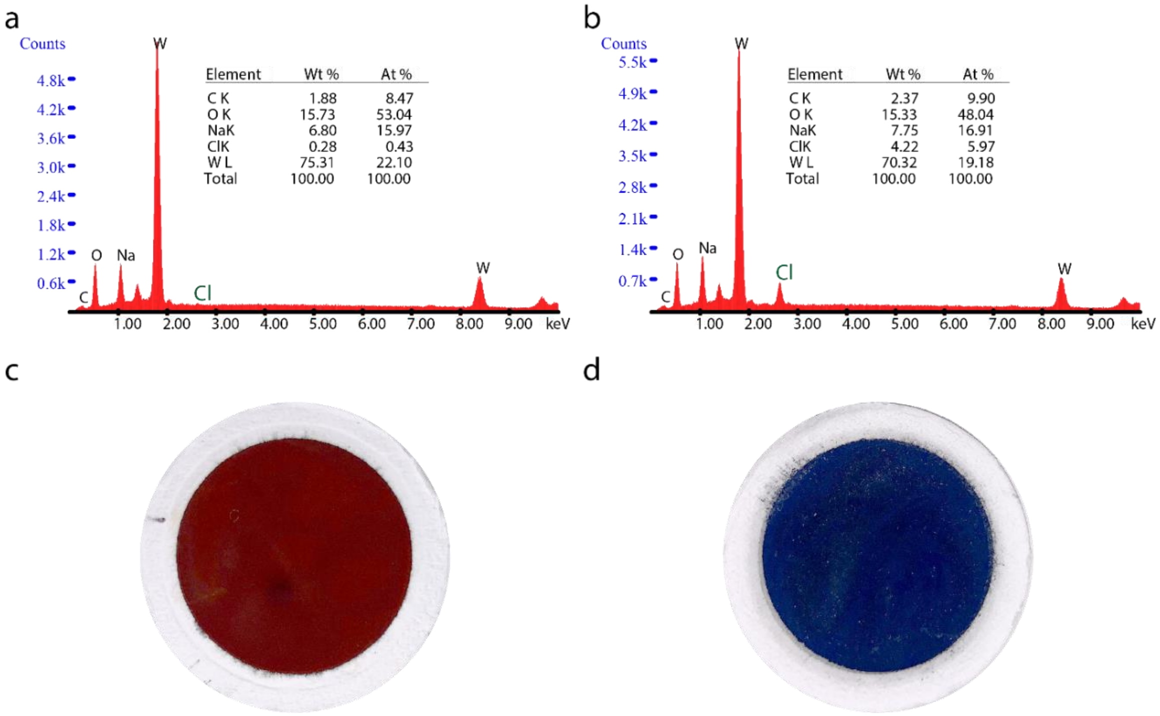

Figure 3-11. EDX data of sodium tungsten bronze for cubic phase (a) and tetragonal phase (b). Photos of sodium tungsten bronze particles in the cubic phase (c) and tetragonal phase (d) when collected on the filter medium.

From the EDX data shown in Figure 3-11, the sample's Na:W:Cl ratio in the cubic phase is ~ 0.72:1.00:0.02 and 0.88:1.00:0.31 for the sample in the tetragonal phase. Assuming all chlorine atoms come from NaCl, the Na:W ratio in the sodium tungsten bronze crystal of the cubic phase was 0.70:1.00 and 0.57:1.00 for the sample in the tetragonal phase. The molecular formulas for the cubic and tetragonal tungsten bronze are thus $Na_{0.70}WO_3$ and $Na_{0.57}WO_3$, respectively.

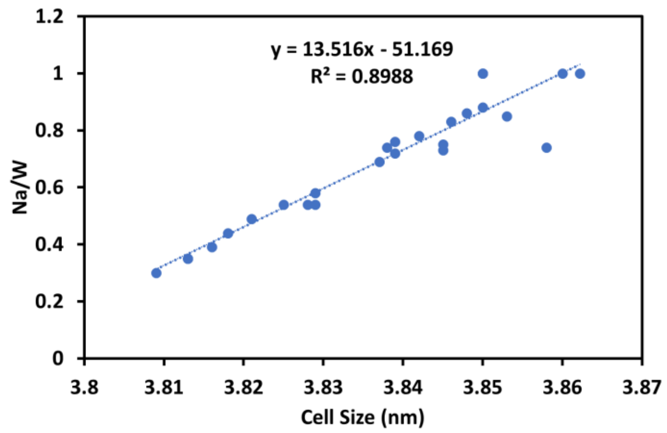

Figure 3-12. Summary of lattice size of cubic sodium tungsten bronze in the ICDD database

By comparing the lattice size of cubic sodium tungsten bronze in the ICDD database (Figure 3-11), a linear equation between lattice size and Na/W can be obtained. By submitting the experimental value of cell size, 3.84 (from XRD), into the equation, the Na/W ratio can be calculated as 0.732, which is very near the value of 0.70 ($Na_{0.70}WO_3$). Figure 3-11c and d are the photos of cubic and tetragonal phase sodium tungsten bronze samples. The purple-red color of the cubic phase sample and the blue color of the tetragonal phase sample aligns with the summary of color vs. ion content by Granqvist[110]. The color difference between the two samples results from different tungsten chemical statuses. Because more sodium atoms occupy the lattice void, the average tungsten valence in the cubic phase sample is lower than the tetragonal one[105], which should be verified by the XPS in Figure 3-13.

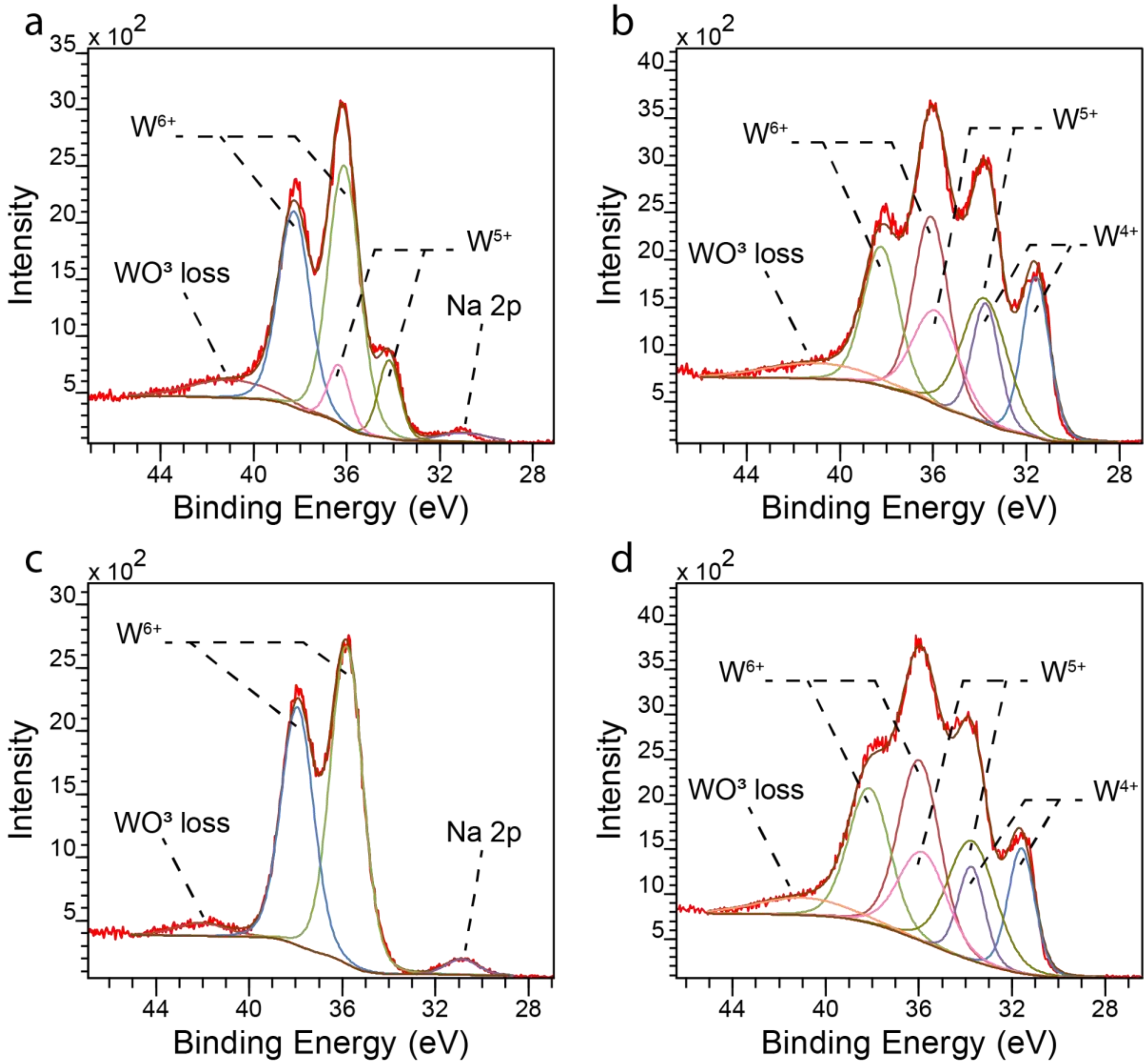

Figure 3-13. XPS data of sodium tungsten bronze samples in the cubic (a, b) and tetragonal (c, d) phases without the sputtering and with the sputtering of 4 min.

The XPS data for the sample products in the cubic and tetragonal phases are shown in Figure 3-13 (without and with the sputtering). For the surface tungsten atom, the V valence tungsten was observed in the cubic phase sample (Figure 3-13a), while no such peak area was identified in the sample of the tetragonal phase (Figure 3-13c). After the sputtering, the XPS data of the cubic phase sample (Figure 3-13b) shows a larger area of V or IV valence tungsten than the tetragonal one (Figure 3-13d). The above evidence shows that the tungsten in the cubic phase sample has more reductive status than the tetragonal phase one, which is the cause for the different band structure for the light absorption in the visible range.

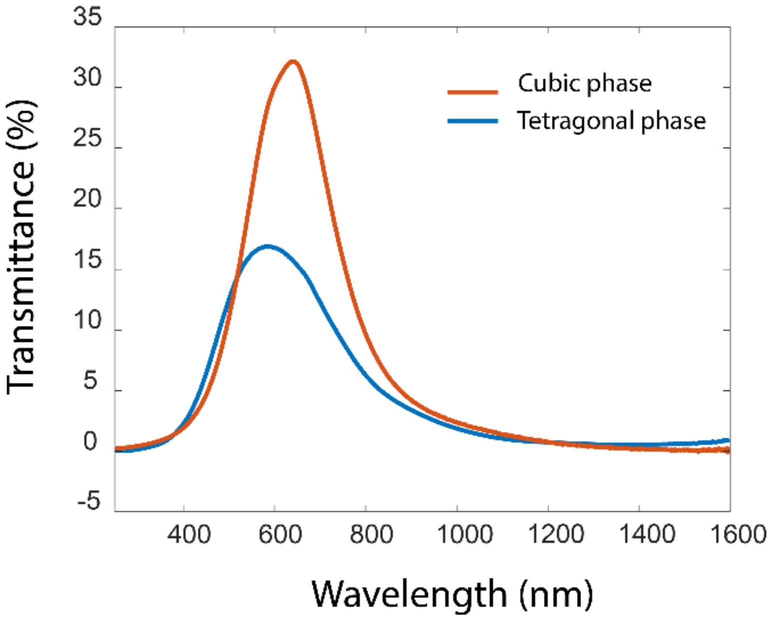

Figure 3-14. Transmittance of the sample sodium tungsten bronze products in the cubic and tetragonal phases (as the function of wavelength). The mass concentration of particles in the medium is kept the same.

Figure 3-14 shows the transmittance of sample particles in the cubic and tetragonal phases. It is found that the cubic phase sodium tungsten bronze particles show better transmittance in the visible light range than the tetragonal one. One possible reason for the observation is that the high sodium ion content in the cubic phase sample makes it highly efficient in the dipole absorption of NIR. Another possible reason is that the impurity content, carbon, and chlorine, in the cubic phase sample (8.47 At% and 0.43 At% in Figure 3-11a) are lower than the tetragonal phase one (9.90 At% and 5.97 At% in Figure 3-11b). The other reason might be that the cubic phase sample has a higher crystallinity, i.e., having less crystal boundary, than the tetragonal phase sample. The crystal boundary scatters the light, resulting in the reduction of transmittance.

3.2.7 Effect of precursor concentration

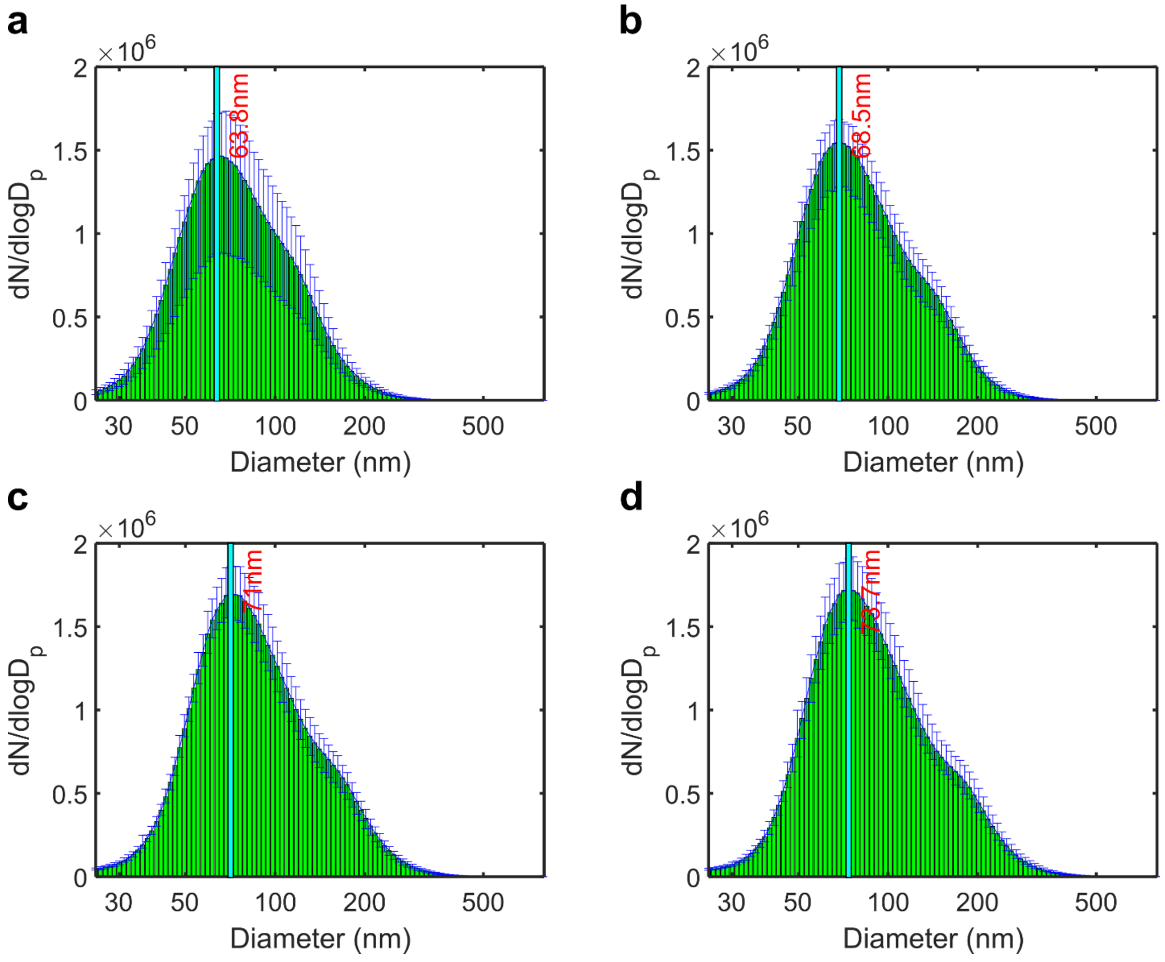

Figure 3-15. Size distribution of sodium tungsten bronze particle synthesized by different precursor concentrations: (a) 0.01 M, (b) 0.02 M, (c) 0.03 M, and (d) 0.04 M.

The concentration of the precursor solution affects the size of the produced particles when the other parameters are fixed. Figure 3-15 shows the size distribution of the sodium tungsten bronze particles produced by the setup in Figure 2-4 with a water-based precursor solution. The varying peak size of the particles at different precursor concentrations is evidence that the higher concentration, the larger the size of the particles. Furthermore, slight increases can be observed for the particle number concentration values. However, the area increase of the size beam does not linear relative to the precursor concentration increase. The reason may be that large particles have a major part in the total mass of particles, so the number count of particles will not reflect the perspective increases of mass input increase of the precursor.

3.2.8 Effect of furnace temperature

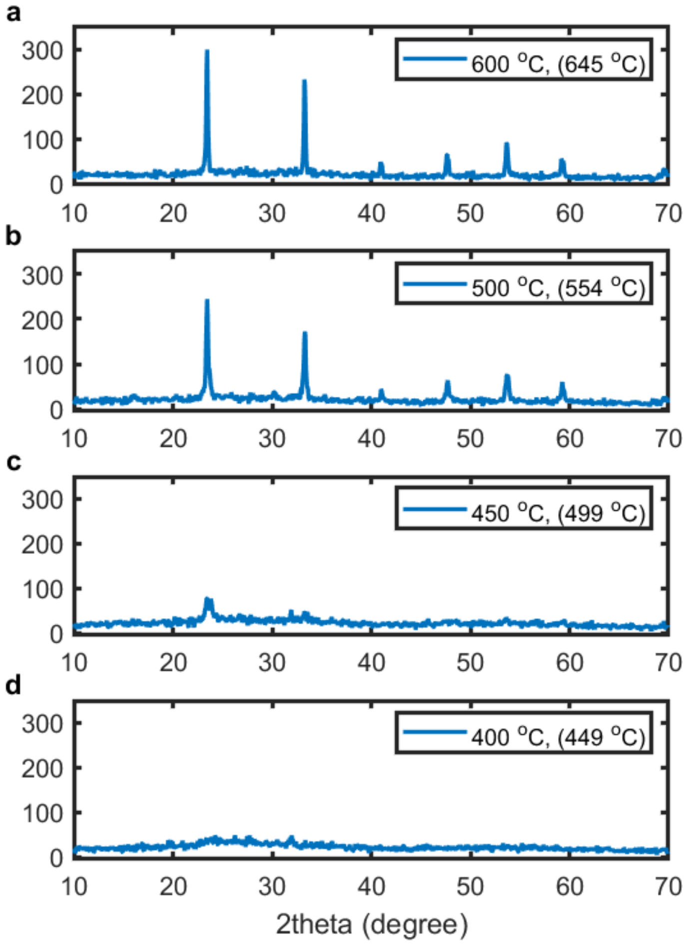

Figure 3-16. Powder-XRD data of sample products were obtained when the tube furnace was set at the setting temperature of (a) 600; (b) 500; (c) 450; and (d) 400 °C, attached with the highest temperature measured in the furnace tube in the bracket. The sample was produced at a Na/W ratio being 1.0 and #2 flow rate being 0.5 SLPM.

As for the effect of furnace temperature on the produced particles, Figure 3-16 shows the powder-XRD of sample products obtained at the different furnace setting temperatures from 400 to 600 °C, with the highest temperature inside the furnace tube indicated. It is found that the furnace temperature should be set above 450 °C to promote the formation of the crystal of sodium tungsten bronze. As the furnace temperature increased, the product samples' crystallinity increased.

3.3 Conclusion

This chapter introduces the relationship between the different precursors/solvents and the produced tungsten bronze particles. The doping alkali species determines the final types of tungsten bronze. Moreover, a similar product can be obtained with the same precursor atomic ratio of M/W (M = Na, K, and Cs), even via different solvent-based precursors. Several combinations of solvents and precursor reagents are summarized. The tungsten bronze particle produced through water-based precursor solution shows relatively high quality. Moreover, the water-based precursor solution has superb versatility for synthesizing sodium, potassium, and cesium tungsten bronze.

As shown in the synthesis of sodium tungsten bronze via methanol-base precursor, the effect of moisture concentration and heating temperature on products' quality (i.e., crystal phase and crystallinity) were systematically investigated. It is observed that the crystal phase and crystallinity are highly correlated to the composition of the precursor solution used. Increasing sodium content in precursor solution improves the crystallinity of sodium tungsten bronze particles. The above trend is also observed as the furnace temperature increases. Furthermore, with sufficient moisture, the byproduct from the reaction is found in trace amounts.

The mechanism of particle formation and chemical reaction involved in the process was further investigated. The methanol solvent in individual droplets is nearly evaporated before entering the tube furnace. The methanol vapor then serves as the reductive regent in the reaction occurred for particles to facilitate particle crystallization.

By varying the Na/W ratio in the precursor solution, sodium tungsten bronze particles in the cubic phase ($Na_{0.70}WO_3$) and tetragonal phase ($Na_{0.57}WO_3$) were produced in high purity. Both particle samples show the ability of the NIR shielding. Compared with those in the tetragonal phase, particles in the cubic phase ($Na_{0.70}WO_3$) have higher visibility in the visible light range because of their lower impurity content and higher crystallinity.

Chapter 4. Size effect on NIR shielding for tungsten bronze particles

4.1 Introduction

This chapter introduces an aerosol-assisted method to produce sodium tungsten bronze particles using aqueous precursor solutions and to experimentally investigate the size effect on the NIR shielding performance of produced particles. This chapter will present the aerosol-assisted method to produce sodium tungsten bronze particles (using DI water as the precursor solvent). A cascade impactor then collected the samples of as-produced particles in different size ranges. The NIR shielding performance of size-selected sodium tungsten bronze particles was then characterized to demonstrate the particle size effect.

4.1.1 Aerosol processing for the particle size classification and collection

Modeling studies found that the NIR shield performance of tungsten bronze particles highly depends on particle size [56,111]. A similar conclusion was also reported for lanthanum hexaboride (LaB_6) particles [49]. LaB_6 particles in a small size (26 nm) have better NIR shielding than ones in large sizes (120 nm). It is thus possible to obtain the optimal NIR shielding and visible transparency of tungsten bronze particles by tuning the particle size. However, preparing tungsten bronze particles in different narrow size ranges is difficult for liquid-phase methods. In literature, ball/bar milling has been the primary method to prepare particle samples with different peak sizes in a wide size range. Several hours of milling time were typical for having particles in sub-micrometer sizes. The smaller the resultant sizes, the longer the milling time. The impurities were often introduced in the milling, contaminating end products. Alternatively, particles produced by an aerosol-assisted method can be easily classified by existing particle collectors, for example, a cascade impactor or an electrical mobility classifier. A cascade impactor classifies particles by the inertial impaction, which is gauged by the particle Stokes number (depending on the particle size and density as well as flow velocity). The classified particle size can be determined when the particle density and flow velocity are specified. An electrical mobility classifier classifies particles based on the electrical mobility of particles. All the particles must be electrically charged before using mobility classifiers.

4.1.2 The particle NIR optics and the size effect of tungsten bronze particles on NIR shielding

The particle size effect on near-infrared (NIR) optics refers to how particles' size can affect their interaction with NIR radiation. In general, the interaction of particles with NIR radiation depends on their size, shape, and composition. As the size of a particle decreases, the surface area-to-volume ratio increases, which can lead to changes in its optical properties. One of the most significant effects of particle size on NIR optics is the phenomenon known as the Mie scattering[112] effect. The Mie scattering effect refers to the way that particles scatter light at different angles, depending on their size relative to the wavelength of the incident light. When the size of a particle is larger than the wavelength of the incident light, the Mie theory dominates the scattering, which predicts that larger particles will scatter light at larger angles. When the size of a particle is smaller than the wavelength of the incident light, the scattering is dominated by Rayleigh scattering[113], which predicts that smaller particles will scatter light more strongly in the forward direction.

These two theories, Mie and Rayleigh scattering, are widely used in particle applications related to NIR optics.

However, the Mie or Rayleigh scattering are theories describing the mono particle interaction with the incident ray. The particle-embedded media for NIR shielding are composed of particles in larger quantities. There is bare to see an overall theoretical equation or modeling that can forecast the effect of particle size on the NIR optics. One of the reasons for that is limited experimental data of particle ensemble in a tuned size for investigation. As for the size effect of tungsten bronze particles on NIR shielding, until recently, the clear relationship between them is still unrevealed due to the lack of the experiment result.

4.2 Method and Experiments

4.2.1 Chemicals, Characterization, and Particle Collection

In our method, the precursors for producing sodium tungsten bronze particles were Ammonium para tungstate, $(NH_4)_{10}H_2(W_2O_7)_6$ xH_2O (*Sigma-Aldrich*), and Sodium chloride, NaCl (*Fisher Scientific*). Ether a filter sampler (i.e., the filter holder with HEPA filter media) or a cascade impactor, i.e., micro-orifice uniform deposition impactor (MOUDI Model 110-R, *MSP Inc.*), was applied for the particle collection. The SEM images of produced particles were characterized by Hitachi SU-70 FE-SEM. The XRD patterns of samples were measured by an X-ray diffractometer (Multipurpose X-Ray Diffractometer, *Empyrean*). The vis-NIR spectrum of particle samples was taken by a spectroscopic ellipsometer (M-2000, *J.A.Woollam*). The TEM of the particle sample was measured by JEM-F200 Cold FEG Electron Microscope.

4.2.2 Experimental Setup and Method

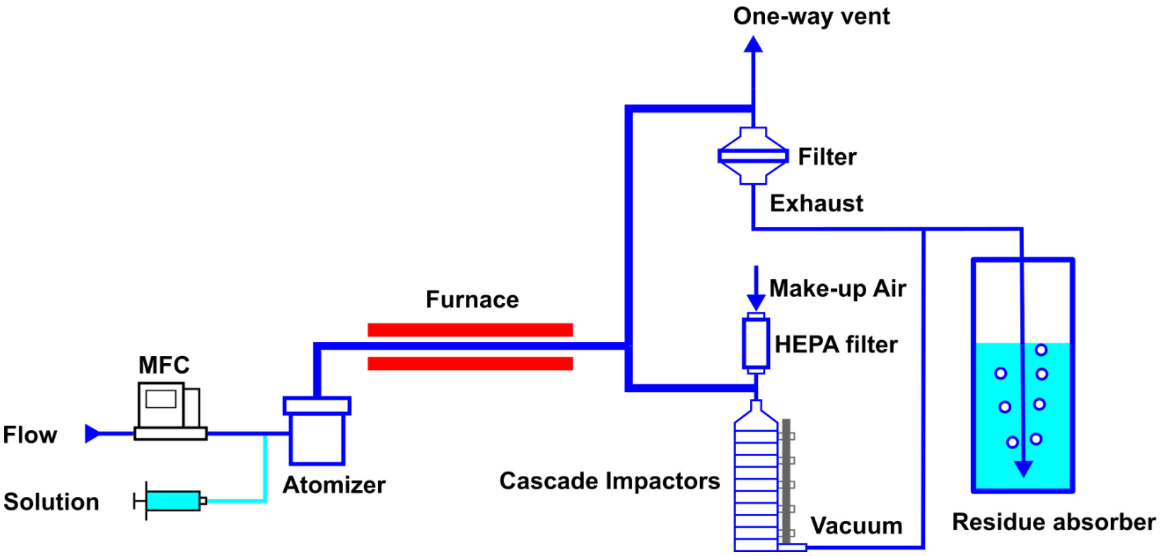

Figure 4-1. Schematic of the experimental setup.

Figure 4-1 shows the schematic diagram of the experimental setup for preparing crystalline sodium tungsten particles. The setup utilized a custom-made Collison atomizer to generate the polydisperse droplets from the precursor solutions. Unlike a typical Collison atomizer in which the spray solution is kept in the spray chamber, the spray solution of this atomizer is fed to the spray nozzle by a syringe pump. The pumping rate was set at 100 $\mu L \cdot min^{-1}$. The compressed mixture gas of nitrogen and hydrogen (N_2 87.5 vol%, H_2 12.5 vol%) was used as the spray and carrier flow to operate the atomizer. The pressure of carrier gas flow was set at 30 psi through a mass flow controller (MFC) to keep the carrier gas flow rate at 2.0 $sL \cdot min^{-1}$. The temperature of the tube furnace (with a heating zone length of 30 in (76.2 cm)) was set at 750 °C. A 3-ft quartz tube (with an outer diameter of 1 inch (2.54 cm) and a wall thickness of ~ 2 mm) was used as the reactor. At the exit of the tube reactor, resultant particles were collected either by a filter sampler (for all the particles) or the MOUDI cascade impactor [114] (for particles in different size ranges). Note that the operational flow rate of the impactor was designed at 30 $L\cdot min^{-1}$. An additional clean make-up air was introduced to mix with the particle stream before the MOUDI impactor. A small percentage of as-produced particles was lost during the mixing. After the collection, the flow passed through a residue absorber to reduce the emission of byproducts to the ambient.

Ammonium paratungstate, $(NH_4)_{10}H_2(W_2O_7)_6$ xH_2O, and sodium chloride, NaCl, were the sources of tungsten and sodium, respectively. The concentration of tungsten in the aqueous ammonium paratungstate solution was set as 0.02 mol/L. The sodium concentration in the aqueous sodium chloride solution is also kept at 0.02 mol/L. Two aqueous solutions were then mixed and used as the spray solution. After the collection, particles at different impactor stages were later transferred to the sample holders for characterization. Sample particles were washed with methanol. The process was to disperse the produced particles in methanol at about 1 mg/mL mass volume fraction, ultrasonically vibrate for 1 min, and then collect the particles by centrifugation. After twice applying the above washing process, the particles were dispersed in IPA with a 1 mg/mL particle mass concentration for the Vis-NIR spectrum measurement. The XRD sample of particles collected by each MOUDI stage was prepared by dropping the same particle suspension on the round glass slide and then drying it for characterization. The prepared particle suspension was then loaded in an optical cell with 1 mm thickness for the transmittance spectrum measurement.

4.3 Result and Discussion

4.3.1 Characterization of as-produced particles

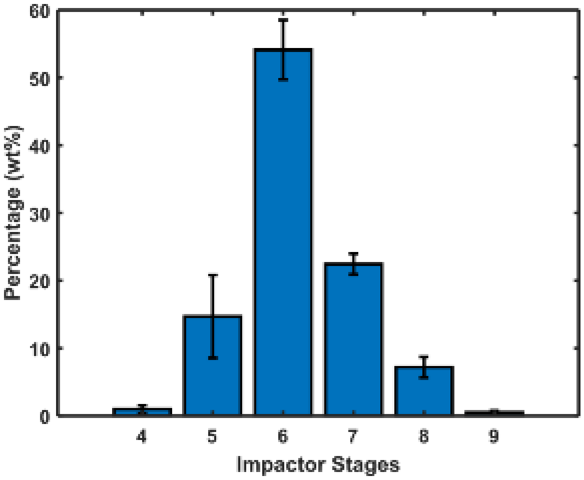

Figure 4-2. Mass-weighted size distribution of washed particle samples collected by the MOUDI impactor.

Figure 4-2 shows the mass percentage of the particles collected by the impaction stages of the MOUDI impactor. It was observed that about 98% of the total mass of produced particles was collected at the 5th to 8th stages of the impactor (Note that the numbering of the stages in the MOUDI impactor can be found in Table 4-1). Accordingly, we primarily selected the particle samples collected at the above stages of the MOUDI impactor for the characterization. The MOUDI impactor was calibrated based on the particle Stoke number (i.e., the 50% cut-off particle size of each impactor stage). The vendor gives the 50% cut-off sizes at different impactor stages, assuming the particle density of 1.0 g/cm^3 (i.e., aerodynamic particle size). Because of the different densities of sodium tungsten bronze particles, the corresponding cut-off size for each impactor stage was thus calculated and shown in Table 4-1.

Table 4-1. MOUDI cascade impactor parameters.

Stage #	Cut-off size (μm)[a]	Slip Coeff.[b]	Particle Size (μm)[c]	Stokes number
1	18.0	1.00	6.6	1.85
2	10.0	1.01	3.6	1.37
3	5.6	1.02	2.0	1.66
4	**3.2**	**1.04**	**1.1**	**2.02**
5	**1.8**	**1.08**	**0.62**	**1.94**
6	**1.0**	**1.15**	**0.32**	**2.22**
7	**0.56**	**1.28**	**0.16**	**2.31**
8	**0.32**	**1.52**	**0.077**	**1.89**
9	**0.18**	**1.99**	**0.036**	**3.15**
10	0.10	2.93	0.017	3.31
11	0.056	4.65	0.0087	2.79

[a] Aerodynamic particle diameter at the 50% collection efficiency of the corresponding MOUDI stage
[b] Slip correction coefficient calculated using Cunningham correction factor [115].
[c] Cut-off particle diameter calculated based on the density of 7.3 g·cm^{-3} for sodium tungsten bronze particles.

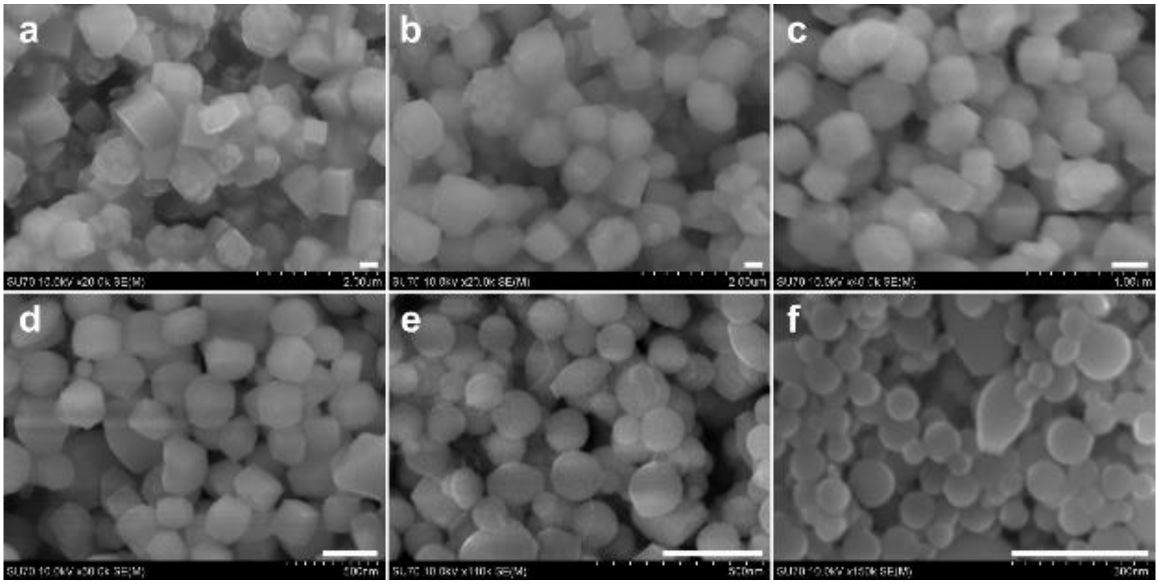

Figure 4-3. SEM images of the particles separated by the cascade impactors, from which the 4th stage (a), 5th stage (b), 6th stage (c), 7th stage (d), 8th stage (e), and 9th stage (f). The scale bar equals 300 nm.

Figure 4-3 shows the SEM images of particles collected at the selected stages of the MOUDI impactor. For the given SEM images, it is found that the sizes of particles collected at the selected stages of the impactor, in general, agreed well with the calculated particle size ranges (shown in Table 4-1). Figure 4-3a shows the images of particles in a size range above 1 µm, which were aggregates (i.e., the assembly of several primary particles). The aggregates (with fewer primary particles than that in Figure 4-3a) were also observed in Figure 4-3b. The bridging of several particles in each aggregate was observed in the above SEM images. The bridging might be formed due to the condensation of water vapor. No bridging was observed from the SEM images shown in Figure 4-3c-f. It might be because of the depletion of water vapor in the first stages of the impactor. The cubic shape was found for particles shown in Figure 4-3c and Figure 4-3d, showing the complete growth of single-crystalline particles in the cubic phase. Particles in slightly large sizes thus have much sharp corners and edges of the cubes, while those in slightly small sizes have more round corners and edges. The shapes of particles shown in Figure 4-3e have much-rounded corners. The shape of the particles in Figure 4-3f was nearly spherical. The above observation was consistent with the fact that the sizes of particles increased during the shape formation in the crystal growth process. Table 4-2 shows the crystallite size calculated from the XRD patterns of particles at selected MOUDI stages. It also shows an increasing trend in the crystal grain size, except for particles at Stage 4. Because of the particle agglomeration at the MOUDI Stage 4, the crystallite size of particles is smaller than that shown in Figure 4-3a and Table 4-1.

Table 4-2. Crystallite size calculated from XRD patterns of particles from each stage.

Stage of particles	Crystallite Size (nm)
S4	855
S5	993
S6	461
S7	219
S8	98
S9	44

Compared to the particles produced in our early work [53], the improvement in the crystal morphology and size uniformity of as-produced particles was observed. It is due to the pre-mixing of precursors before entering the tube reactor in the current process. In the previous process of producing Na_xWO_3 using methanol [53], H_2O was introduced and mixed with other precursors in the gas phase. The mixing in the gas phase may not be as effective as in the liquid phase.

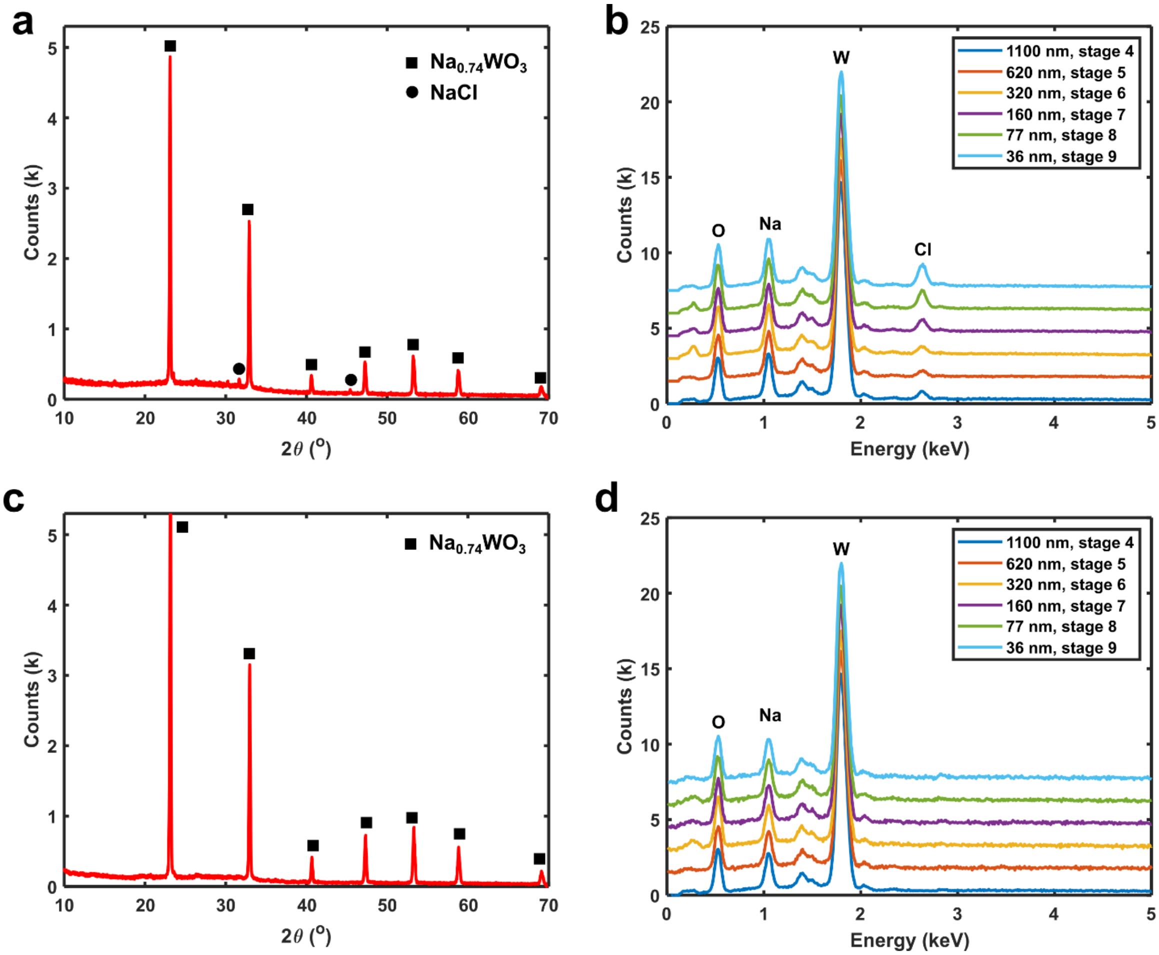

Figure 4-4. XRD of particles collected by filters before washing off (a) and after washing off (c). EDX of particles collected on selected MOUDI stages before washing off (b) and after washing off (d).

The XRD patterns in Figure 4-4a show that all the particles produced by the current process were in the sodium tungsten bronze phase and corresponded to $Na_{0.74}WO_3$ (PDF 01-075-0232). Notice that the particle sample characterized here was collected by filter sampling (i.e., no size classification), not by the MOUDI. A small amount of NaCl was detected in the unwashed product. The EDX analysis (for the elemental composition) of the particle samples at the selected MOUDI impaction stages is also shown in Figure 4-4b. The energy positions corresponding to specific elements are tagged in the spectrum. It can be found that the peaks of chlorine became higher in the samples of particles of small sizes. Because the chlorine source is NaCl in our process, the EDX result implies that particles in smaller size ranges have higher NaCl contents. After the wash step, the NaCl residue in the particle samples collected on filters (i.e., no size classification) was removed, evidenced by the XRD pattern for washed particle samples (Figure 4-4c). The EDX of washed particle samples collected on the MOUDI stages (Figure 4-4d) also shows that no chlorine exists in the particle samples.

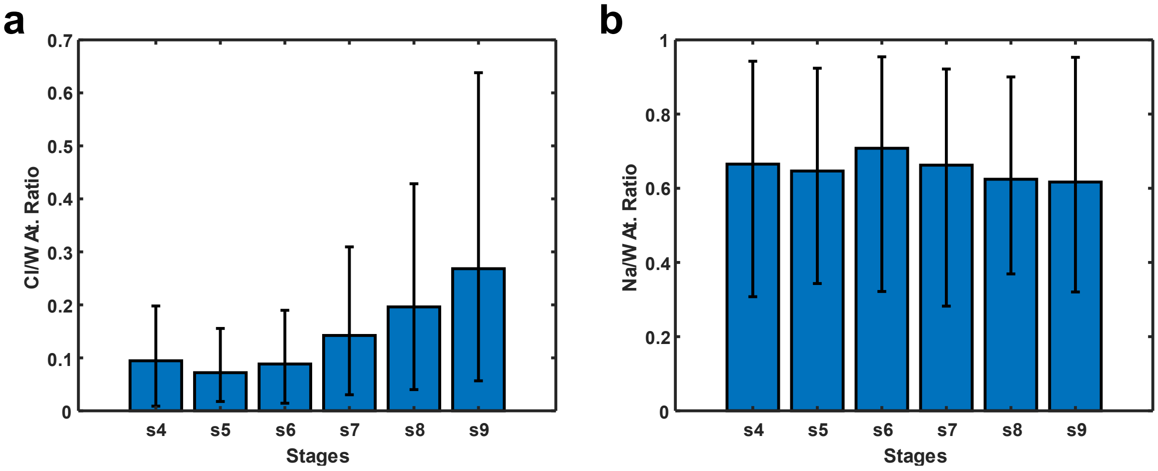

Figure 4-5. The atomic ratios of chlorine to tungsten of unwashed (a) and washed (b) particle samples collected on selected MOUDI stages. All data were calculated from EDX data analysis. Each stage sample was tested 10 times on different areas with thick particle accumulated layers.

Figure 4-5a shows the atomic ratio of chlorine to tungsten in the unwashed particle samples collected at the selected stages of the MOUDI (calculated from the statistics EDX data). The Cl/W atomic ratio was increased with the stage number (except the 4th stage), indicating that small particles have more NaCl (or HCl) residual than large ones. Particles collected on the 9th stage had 2 times more NaCl content than those on the 5th. It is because particles of small sizes can absorb more NaCl (or HCl) on the surfaces than those of large sizes (due to the high specific surface area of small particles). On the contrary, Figure 1-1b shows the Na/W for washed particles collected on selected MOUDI stages. All the ratio values for washed particle samples collected by each MOUDI stage are approximately 0.6+. The Na/W values for washed particles collected by all the MOUDI stages are close, indicating the Na content in the lattice of particles is the same for washed particle samples collected by all the MOUDI stages. It further evidenced that the chemical composition of washed particles of different sizes produced by the process is consistent. Note that the above ratio is less than the values obtained from the XRD data (~0.7). The above observation is because the window of the XRD sensor partially absorbs the X-Ray signal produced by the light element. Due to Z = 11, sodium is very close to the lower limit of the acceptable measurement range. The quantitative data of the sodium element by EDX is thus not reliable[116].

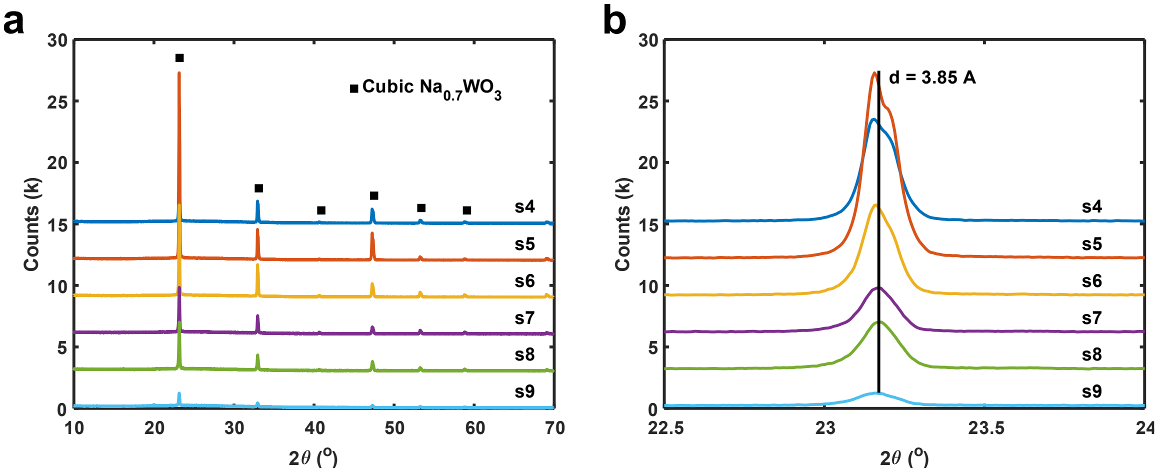

Figure 4-6. (a) XRD pattern of washed particles collected at selected MOUDI stages. (b) Zoom out of the XRD pattern from 22.5 to 24 degrees of 2θ.

The result of XRD measurement for particles collected at selected MOUDI stages is shown in Figure 4-6. In Figure 4-6a, it is found that few NaCl peaks were shown in the XRD patterns of particle samples collected on MOUDI stages, and all of the shown peaks corresponded well to cubic $Na_{0.7}WO_3$. From Figure 4-6b, we found that, for particles collected by MOUDI stages, their d-spacings were close to 3.85 Å, indicating that the x value is ~0.7 for Na_xWO_3 particles from all the stages, according to the relationship between the x values and lattices constant in reference [104]. Note that, despite particles collected on different MOUDI stages being different in size, they are consistent in the crystal structure and chemical composition. The TEM and SEAD characterization supported the above conclusion (Figure 4-7). It is evidenced that particles in both small and large sizes were mostly single crystalline and made of cubic $Na_{0.7}WO_3$. It can be deduced that all the particles simultaneously formed because only in this way that the element concentrations of Na and W are the same for all the particles, resulting in the same chemical composition and crystal structure for all the particles.

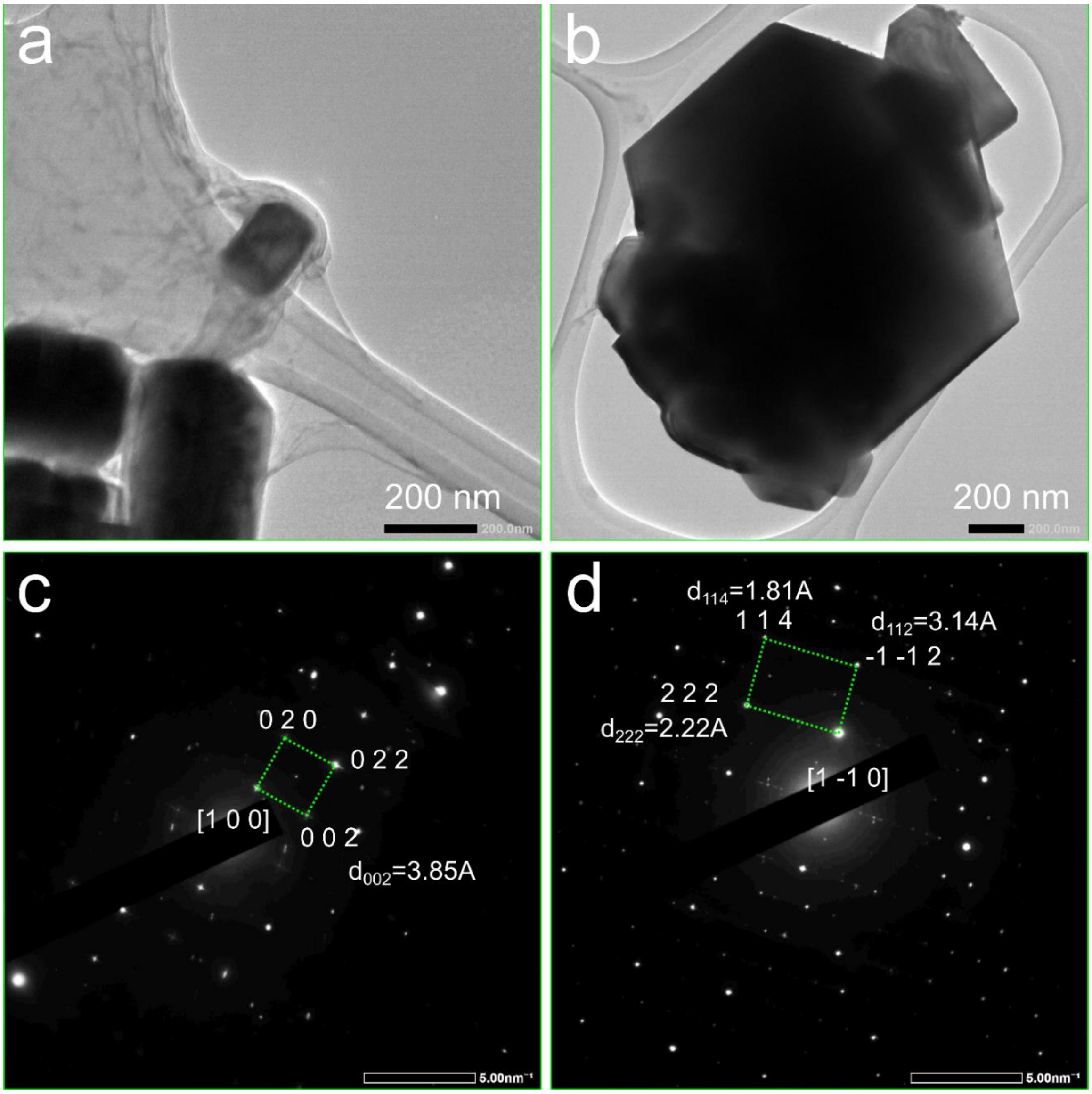

Figure 4-7. TEM images of small particles (a) and large particles (b), and SEAD patterns (c) and (d) of the particles shown in (a) and (b), respectively. Particle samples were washed.

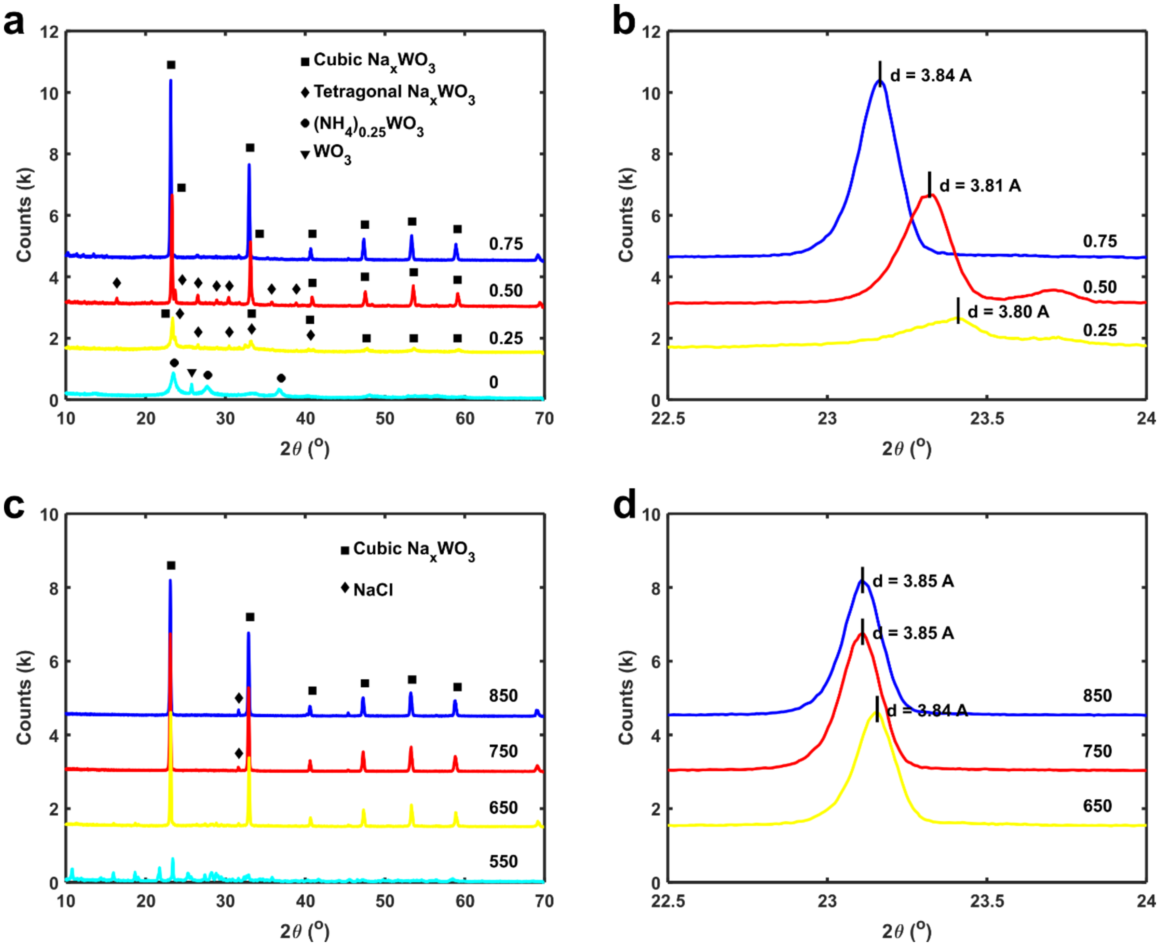

Figure 4-8. (a) XRD of the washed particle samples from the Na/W ratio equal to 0, 0.25, 0.50, and 0.75 in the precursor. (b) The zoom-in from 22.5° to 24° of 2θ in the picture (a). The corresponding d-spacing is listed. (c) XRD of the washed particle sample (Na/W = 1.0) from the furnace temperature set to 550, 650, 750, and 850 degrees Celsius. (d) The zoom-in from 22.5° to 24° of 2θ in picture (c). The corresponding d-spacing is listed. The unit is Å.

Figure 4-8a showed that the as-produced products had different phase compositions when the Na/W ratio in the precursor solutions was varied. A high Na/W ratio in precursor solutions led to a high content of Na_xWO_3 particles in the cubic phase. A low Na/W ratio in the precursor solutions resulted in particles in a tetragonal phase and poor crystallinity (i.e., low intensity of the peaks). When no NaCl was presented in the precursor solutions, the as-produced product was a mixture of $(NH_4)_{0.25}WO_3$ and in very poor crystallinity. From Figure 4-8b, we found that the peak positions of the samples made from precursor solutions of different Na/W ratios changed with the variation of Na content. The corresponding d-spacing (also given in the same figure) evidenced that the crystal lattice was enlarged by more Na atoms inserted in the crystal structure.

The effect of furnace temperature on the process is shown in Figure 4-8c. It was found that the phase of cubic Na_xWO_3 particles only existed when the furnace temperature was set above 550 ºC. Since the lattice constant is closely related to the Na content in the lattice[104], the more the Na atoms doped into the lattice, the larger the d-spacing of the lattice constant. With the increased furnace temperature, more Na atoms can be doped into the crystal lattice, enlarging the d-spacing (Figure 4-8d). In addition, the XRD patterns of unwashed particle samples prepared at different furnace temperatures (Figure 4-8c) show that the NaCl phase showed when the furnace temperature was above 650 ºC. In cases of 750 and 850 ºC, the NaCl phase peaks became clearer than that in the 650 ºC case. The above observation indicated that NaCl could crystallize and form an independent phase at above 650 ºC. At the temperature of 550 ºC, the XRD pattern shows no clear Na_xWO_3 (or NaCl) phase. It is due to the precursor not fully decomposing at a temperature below 650 ºC. Furthermore, the d-spacings of the peaks between 22.5 to 24 degrees of 2θ (Figure 4-8d) show nearly the same 3.85 Å in both 850 and 750 ºC cases, indicating that no more Na atoms could be doped into the lattice at 850 ºC when referenced to that in the 750 ºC case. The more doping Na atom in the lattice, the larger the crystal lattice size. Therefore, it concluded that 750 ºC is sufficient for this process to obtain a qualified product. When the flow passes the high-temperature tube, the overdose of NaCl is in the form of vapor. After exiting the high-temperature furnace, the residual NaCl vapor might condense on resultant $Na_{0.7}WO_3$ particles. Because the melting points of pure bulk WO_3 and NaCl are 1,473 ºC and 800 ºC, respectively, solid residual NaCl should occur at the time of Na_xWO_3 particles forming. The NaCl vapor condensed on the surface of all particles, resulting in higher chlorine content in small particles than in large ones. It is because the smaller the particle size, the higher the per specific surface area.

4.3.2 Formation mechanism

For the reaction mechanism, the chemical reaction that occurred in the tube reactor is given in the following:

$$(NH_4)_{10}H_2(W_2O_7)\cdot xH_2O + 6yH_2 + 12yNaCl$$
$$\rightarrow 12Na_yWO_3 + (x+6)H_2O + 10NH_3 + 12yHCl$$

Aerosol droplets containing the reaction agents (i.e., ammonium paratungstate and sodium chloride) were vaporized once entering the high-temperature tube reactor. The produced compound ammonia and hydrochloride acid were removed with the exhaust flow. No other byproduct except the NaCl was thus kept in as-produced particles.

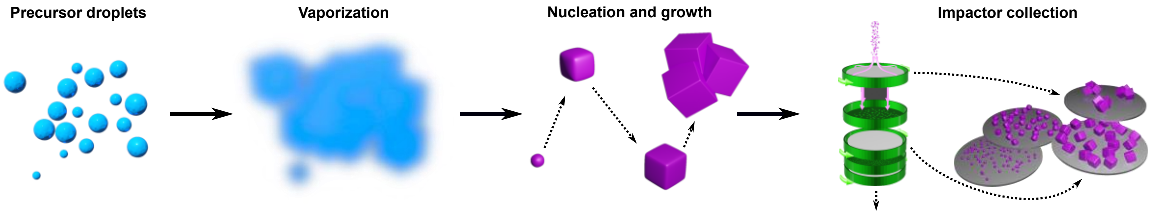

Figure 4-9. Illustration of the particle formation and separation in our preparation process.

Figure 4-9 illustrates sodium tungsten bronze particles' formation mechanisms and the MOUDI impactor's size classification in our current process. Aerosol droplets generated by the Collison atomizer were carried by the $N_2 + H_2$ flow to enter the tube reactor heated by a high-temperature furnace. Since the furnace temperature was set as high as near the melting points of all the reaction agents dissolved in the precursor solution, aerosol droplets were quickly vaporized upon entering the tube reactor. After the carry flow passed through the peak temperature zone in the tube reactor, its temperature decreased, and the nucleation occurred as the temperature dropped below a particular value (i.e., the vapor-to-particle conversion). The vapors of reactants then condensed on newly formed nuclei. The sizes of nuclei grew, and their shapes of particles converted to cubic morphology due to the crystal anisotropy. The carrier gas flow rate was kept at 2.0 sL·min^{-1} to ensure the formation of particles and their crystallinity at a relatively high-temperature level before exiting the tube reactor. From the size dispersity and morphology of particles shown in Figure 4-3, it can be assumed that nucleation was homogenous for the tungsten bronze particles in our process. After exiting the tube reactor, as-produced particles were classified in the cascade impactor (i.e., MOUDI). An impactor collected particle based on particle inertia, characterized by the particle Stoke number. In a cascade impactor, the size of nozzles is reduced for each stage to collect particles in smaller sizes. Large particles are thus collected in the first stages, and smaller particles are collected in the later stages of a cascade impactor.

4.3.3 Optical performance of as-produced particles at selected stages of the MOUDI

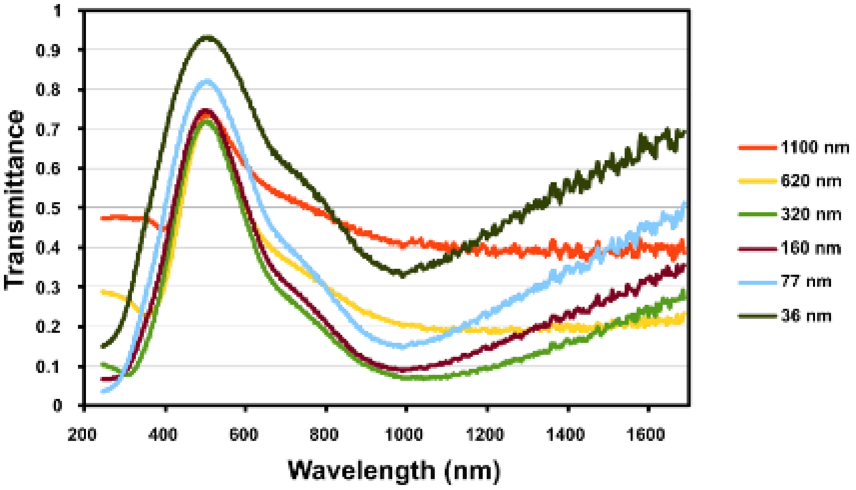

Figure 4-10. The Vis-NIR spectrum of washed sodium tungsten bronze particle samples collected on selected MOUDI stages stage (with different particle cut-off sizes).

Figure 4-10 shows the Vis-NIR spectrum for particles at the selected stages of the MOUDI impactor. In the UV range, the absorption of particles enhanced with the decrease of the particle sizes down to ~77 nm (i.e., the 8th stage). Particles at the 9th stage (i.e., ~36 nm) have a lower UV absorption than those at the 8th stage (~ 77nm). In the visible range, the wavelength for the maximal transmittance occurred at ~500 nm wavelength for particles at stages 4-9 (~1100 nm to ~36 nm). However, the maximum transmittance was increased with the decrease of the particle size (for the samples at stages 4-9). In the NIR range, the absorptance increased with the decrease of the particle size (from ~1100 nm to ~320 nm) and then gradually decreased with the further decrease of the particle size (at the same particle mass concentration). Therefore, at the same particle mass, the transmittance of visible light of $Na_{0.7}WO_3$ particles can enhance by reducing the particle size. However, the decline of the NIR absorption for the particles was also observed when the size was further decreased. Thus, an index, SETS (solar energy transmittance selectivity), defined in the previous works [62,77,117], was used to identify the best optical performance of sodium tungsten bronze particles for the NIR shielding.

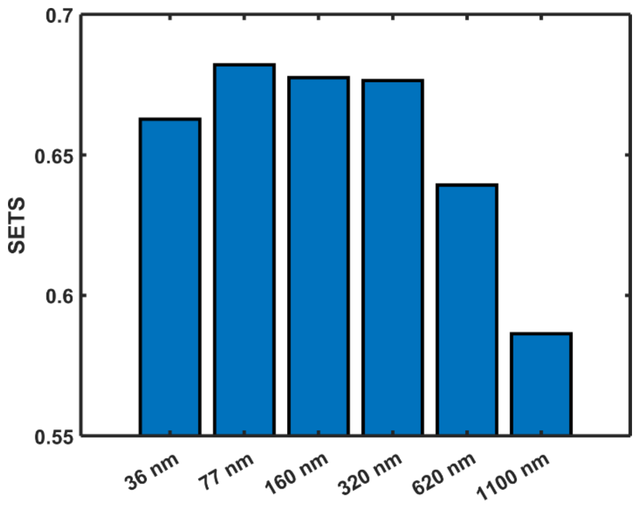

Figure 4-11. Solar energy transmittance selectivity (SETS) of washed particle samples collected on selected MOUDI stages.

Figure 4-11 shows the solar energy transmittance selectivity (SETS) [62,77,117] for particles at selected stages of the MOUDI impactor. The SETS are defined in the following:

$$SETS = \frac{1}{2}\left(1 + \frac{\int_{UV}^{vis} E(\lambda)T(\lambda)d\lambda}{\int_{UV}^{vis} E(\lambda)d\lambda} - \frac{\int_{vis}^{NIR} E(\lambda)T(\lambda)d\lambda}{\int_{vis}^{NIR} E(\lambda)d\lambda}\right)$$

It is a coefficient to evaluate the ability of the NIR shielding of transparent materials. The higher the SETS value, the better the NIR shielding. It is found that based on the index of SETS, particles at the 8th stage (~ 77nm) of MOUDI have the best NIR shielding performance for the transparent sodium tungsten bronze particles at the specific condition. Particles collected at the 6th and 7th stages (i.e., ~ 320 nm and ~160 nm, respectively) of MOUDI have slightly less NIR shielding performance than those at the 8th stage. The transmitted fraction of visible light and NIR for particles collected by selected MODUI stages are shown in Figure 4-12. They were calculated according to the following equations:

$$Visible\ light\ transmitted = \frac{\int_{UV}^{vis} E(\lambda)T(\lambda)d\lambda}{\int_{UV}^{vis} E(\lambda)d\lambda}$$

$$NIR\ transmitted = \frac{\int_{vis}^{NIR} E(\lambda)T(\lambda)d\lambda}{\int_{vis}^{NIR} E(\lambda)d\lambda}$$

It is found that the variation of transmitted NIR fraction for particles at selected MOUDI stages is larger than their fraction of visible light. The combination of both fractions contributes to the SETS values, thus decreasing SETS values (due to the significant loss in the NIR shielding) for 36, 630, and 1100 nm particles. According to Figure 4-2, more than 80 wt% of as-produced particles were collected in these three stages (i.e., stages #6, #7, and #8 of MOUDI).

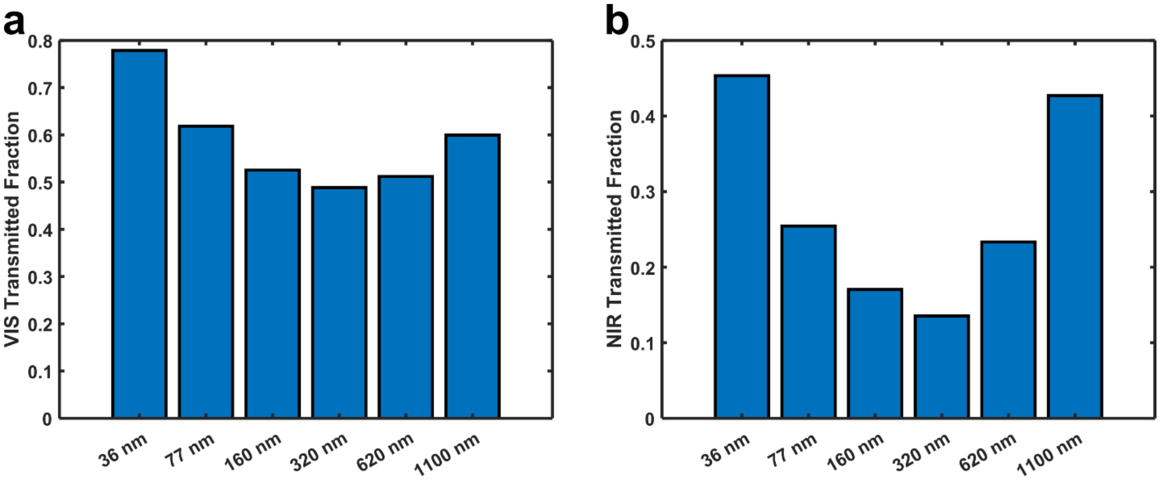

Figure 4-12. Visible light (a) and NIR (b) transmitted fractions for washed particle samples collected on selected MOUDI stages.

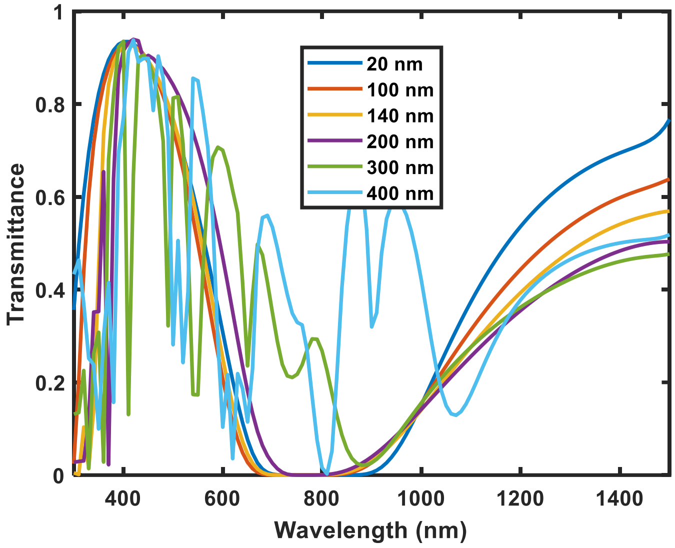

Figure 4-13. Calculated transmittance spectrum for one sphere particle in different sizes confined in the periodic domain.

NIR absorption based on the localized surface plasmon resonance (LSPR) is generally observed for very small particles[118]. LSPR surely exists for small particles absorbing the NIR in a specific wavelength range. However, LSPR is not the only impactor on the NIR shielding performance of particles because the size of NIR shielding particles is highly relative to the scattering of lights, e.g., the Mie scattering. We conducted optical modeling based on Maxwell's equation (via COMSOL) to demonstrate the effect of light scattering. The detail of the modeling can be found in the SI (supplementary information). Figure 4-13 shows the calculated transmittance as a function of wavelength for particles in the sizes of 20, 100, 140, 200, 300, and 400 nm. It shows that the NIR shielding performance of particles in the wavelengths ranging from 1,000 to 1,500 nm declined as the particle size was reduced, which is consistent with the trends experimentally observed in the measured Vis-NIR data (Figure 4-10), and the NIR transmitted fraction (Figure 4-11b). The whole NIR range (i.e., 700 to 1500 nm) was considered in calculating the data shown in the above two figures. If multiple particles are randomly presented in the computational domain, the effect of multiple scattering may make it even more obvious on the variation among the particle sizes. The scattering effect on a specific NIR wavelength could be why the observed NIR shielding performance loss for fine particles. Notice that a high variation of calculated transmittance in less than 1000 nm wavelength was observed for particles of 300 and 400 nm sizes (Figure 4-13). It is because the particle size is close to the wavelength, increasing the interference between the particle size and specific light wavelength, as well as the periodic boundary condition used in the modeling. Our future research will conduct a comprehensive investigation using the modeling (considering multiple particles).

4.4 Conclusion

Crystalline particles of sodium tungsten bronze were produced by an aerosol-assisted process with aqueous precursor solutions. The XRD characterization of as-produced particles indicated that the chemical composition and crystallinity of particles were $Na_{0.7}WO_3$ and excellent, respectively. The mass-weighted size distribution of as-produced particles was also measured by MOUDI. It is found that nearly 80% of particles (by mass) were collected at the 5th to 8th impaction stages of MOUD, which was the size range of particles offering excellent NIR shielding performance (concluded after the characterization of optical transmittance of size-selected particles samples). Particles in different narrow size ranges were classified and collected by the MOUDI. The morphology, chemical composition, and visible-NIR spectrum of size-selected particle samples were characterized. According to the measured NIR spectrum and the SETS index, the size range of produced particles providing the optimal NIR shielding while having a good transmittance for visible lights was found. The loss of NIR shielding for small particles was preliminarily investigated using optical modeling based on the Maxwell equations.

Chapter 5. Optical modeling of tungsten bronze particles

5.1 Introduction

This chapter introduces the NIR shielding performance of an ensemble of tungsten bronze particles. This chapter includes the effects of particles' size and concentration (i.e., packing density) on the NIR shielding performance of particles. Maxwell's equations (solved by a finite element method) were used to calculate the NIR optics of sodium tungsten bronze particles randomly positioned in a transparent carry media. In addition, experiments were further performed to validate our experimental findings. For reference, the optics of a single particle was also modeled. Moreover, to give an insight into the particles' shape effect on the NIR shielding, the cubic particle ensemble modeling is also included to compare with the spherical ones.

5.1.1 Introduction article dispersed media in practice

Equipping window glass with the capability of shielding the NIR (near infrared) light in the solar spectrum has been the solar control strategy, which is widely applied to reduce the energy consumption of heating, ventilation, and air conditioning (HVAC) systems in modern buildings and transportation systems/vehicles. The shielding of NIR for window glass is typically realized by low-emissivity coatings made of silver, indium- or antimony-doped tin oxide (ITO and ATO) layer. The above materials, however, have their limitation for the application. The key functional layer in a Low-E coating is the metallic layer. Although providing good solar heat shielding, the Low-E coatings are in multiple layers, usually requiring complex coating processes to apply. ATO and ITO-based coatings are also excellent for heat shielding, but silver, indium, and antimony costs are expensive.

Alternatively, Tungsten bronze (M_xWO_3, M = Li, Na, K, Ru, Cs, and NH_4) is a promising NIR shielding material in solar energy control applications [119]. These materials have been synthesized by various methods, for example, hydrothermal [60], solvothermal [61], fused salt electrolysis [73], solid-phase reaction [70], flame pyrolysis [62], aerosol-assist spray [120], ball milling [81], and sputtering [121]. In all cases, tungsten bronze particles are synthesized and then applied inside or on the surface of the transparent media, which could be a polymer [72] or glass matrix [56]. Then, due to the optical properties of tungsten bronze, such particle-suspended media can shield NIR and be transparent to visible light.

Different from a slab made of the bulk NIR-shielding material, the optical performance of particle-suspended media is further affected by the physical characteristics of tungsten bronze particles, for example, the size, shape, and concentration of particles in carry media (in addition to the optical property of the material). It is because of the interaction of particles with light. Due to the sizes of these tungsten bronze particles (typically less than 1 μm in size) being close to the wavelength of electromagnetic radiation in visible and NIR ranges (Visible: 400 nm - 750 nm; NIR: 750 nm - 2,500 nm), the interaction between the particles and the light in the Vis-NIR wavelength range could be intensified for particles in certain sizes. The above observation has been reported in previous works. The experimental works [48,49] on lanthanum hexaboride, another NIR shielding material, show that the particle size can highly affect the NIR extinction. In their works, particles in small sizes have a higher extinction in the 900 nm – 1200 nm NIR range. The shape of particles also affects the optical performance of particle-suspended media. The modeling [56,111] based on discrete dipole approximation (DDA) [89] shows that the light scattering extinction varied with the size and shape of tungsten bronze particles (Cs_xWO3, Na_xWO3). The valley of absorptance curves shifts with different shapes of particles, including spherical, cubic, cylindrical, and tetrahedral ones. When particle shape's asymmetry, or the aspect ratio, increased, the light's absorptance valley of particles moved towards the longer wavelength in the solar spectrum. More, the extinction curve valley shifted towards the shorter wavelength and broadened as the particle size decrease.

5.1.2 Modeling of single particle

The modeling based on the Mie scattering[122] has been applied to analyze the NIR optics of a single particle. In the Mie theory, the dielectric function (or refractive index) is treated as a constant to be input at a given wavelength. The extinction cross-section area of a particle in a specific diameter can then be calculated for a given light wavelength. However, the Mie scattering incident ray only applies to a particle with a diameter close to the light wavelength [112]. The DDA method [89] has also been applied to study the optical performance of individual particles via the dipole approximation for the object structure (with the consideration of nanoparticles). The above method can model the optical characteristics of an individual particle in different morphology, e.g., in the spherical, cubic, or cylindrical shape). However, it also requires the dielectric function of the matter as the input parameter.

5.1.3 About the multi-particle optics on NIR shielding

Although the research on the NIR optics for tungsten bronze particles has been reported, all the modeling works only focused on individual particles, not particle ensembles. In the meantime, NIR shielding particles are randomly suspended in a transparent carry matrix. For a coating of particle-suspended media, the variation of the coating thickness is inevitable, which may make the volumetric packing density in the layer significantly change. The effect of particle packing density on the optics of tungsten bronze particles has not been investigated.

5.2 Modeling and Experiments

5.2.1 For the optical modeling of particles

The COMSOL software with the optical module was selected for this optical modeling. In the optical module of COMSOL, the Maxwell equations for electromagnetic waves are solved by the finite element methods [123]. Two different computational domains were used in the modeling: one domain is for an ensemble of randomly placed particles (in a cubic domain), and the other is for a single particle (in a spherical domain).

Sodium tungsten bronze particles were selected for the modeling. The dielectric function (or refractive index) of sodium tungsten bronze ($Na_{0.74}WO_3$) in the wavelength ranging from 300 nm to 1,000 nm was obtained from Owen's work [50]. In the above work, the optical property of sodium tungsten bronze was measured by the polarization modulation ellipsometry on a polished slab of bulk crystalline tungsten bronze synthesized by electrolysis growth from a fused salt melt. A similar process was also applied to measure other bulk tungsten bronze materials doped by cesium 6 and potassium [124]. The dielectric function of sodium tungsten bronze in the wavelength from 1,000 nm to 1,500 nm was obtained from the extrapolation of Owen's data. The above extrapolation was also assisted by the data obtained in the density functional theory calculation of Tegg's work [125]. The refractive index of sodium tungsten bronze particles used in the calculation is shown in Figure 5-1. In this work, the carry media for suspending particles was isopropyl alcohol (IPA). The refractive index of IPA was set to 1.37.

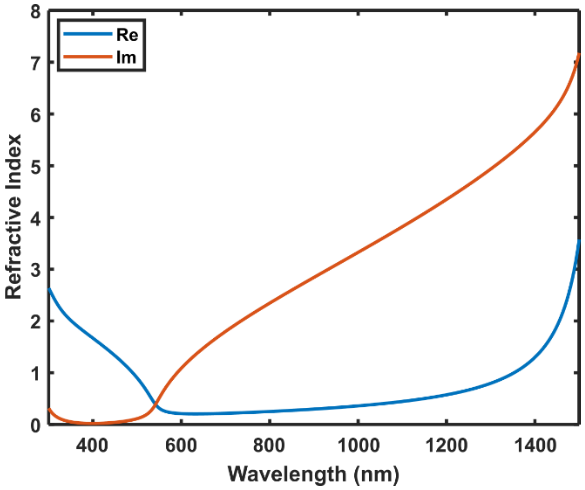

Figure 5-1. The refractive index of $Na_{0.74}WO_3$ using in this work.

5.2.2 In the case of a particle ensemble

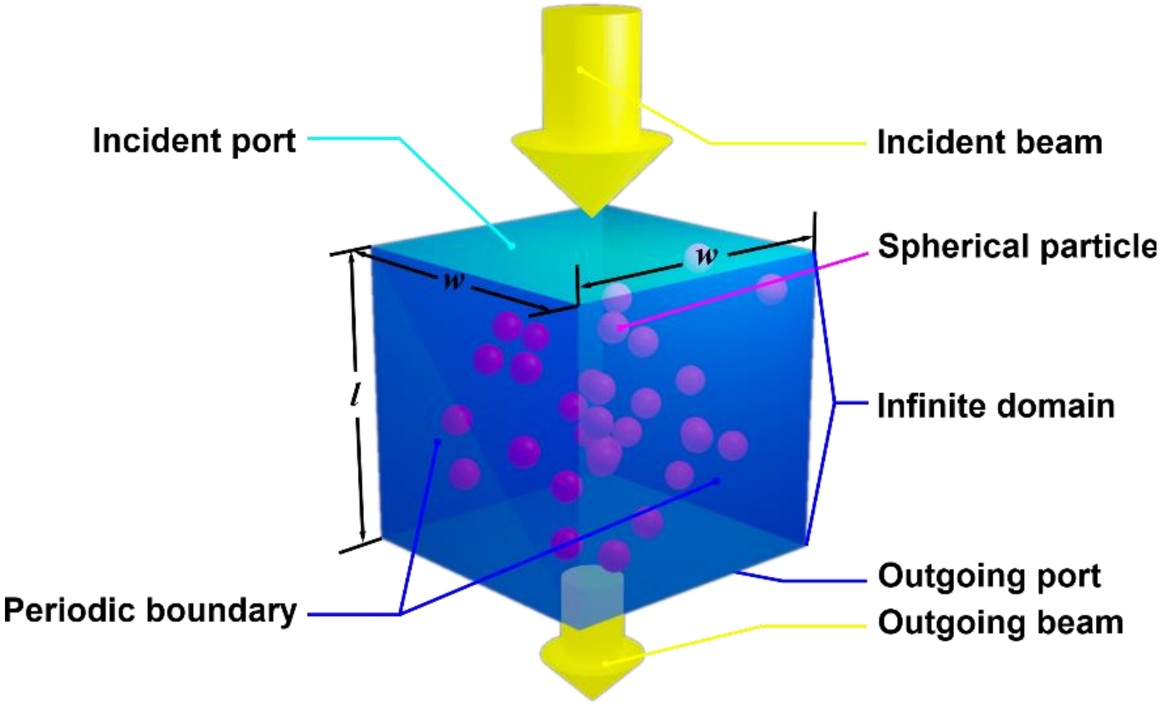

Figure 5-2. Schematic of an ensemble of randomly placed particles in the cubic domain.

Figure 5-2 shows the computational domain for the case with multiple particles. Particles in a specified total number of n and the diameter of d_i were randomly distributed in the domain. The incident beam entered the domain from the top and exited from the bottom. The periodic boundary conditions were applied to the sidewalls of the domain. The tangential components of the electric and magnetic field are equal on the source and destination (the two boundaries in opposite directions). In other words, the domain was irradiated by a plane wave beam from the top. The square cross-section of the domain has the side of w. The path length, l, of the light through the domain, i.e., the thickness of the computational domain, were randomly assigned within the range defined by Equation 5-1 for the modeling:

$$l \in [0.5w, 2w]$$

Equation 5-1

Given the number of particles, n, and their sizes, d_i (where i is the index for each particle), the volumetric packing density of particles in the computational domain can be calculated as Equation 5-2.

$$p = \frac{V_{pTotal}}{V_D} = \frac{1}{w^2 \cdot l} \sum_{i}^{n} \frac{\pi d_i^3}{6}$$

Equation 5-2

V_D is the volume of the computational domain; V_{pTotal} is the total volume of all the particles; p is the volumetric packing density of particles in the domain. Moreover, w is the width of the square cross-section of the domain.

The transmittance of the light passing through the computational domain was calculated based on the ratio of the energy integration on the outgoing surface to that on the incident light surface. The attenuation of the light for the computational domain was calculated from the transmission by Equation 5-3.

$$T = \frac{I_t}{I_0} = \exp(-\mu_{att} l)$$

Equation 5-3

where T is the transmittance of the incident beam. I_0 is the incident beam energy. I_t is the outgoing beam energy. μ_{att} is the attenuation coefficient of the computational domain. l is the thickness of the computational domain. In addition, the reflectance R can be obtained by the ratio of energy integration for the reflected beam I_r to the incident beam I_0 on the incident surface:

$$R = \frac{I_r}{I_0}$$

Equation 5-4

The absorptance A can be easily obtained as Equation 5-5.

$$A = 1 - R - T$$

Equation 5-5

The attenuation coefficient μ_{att} can be normalized by the volumetric packing ratio p, marked as μ_{att}/p.

In the modeling calculations, the wavelength from 300 nm to 1500 nm is considered for all the cases. Each case's particles in 40, 100, 140, 200, 300, and 400 nm sizes are calculated. The mesh method for each modeling is free tetrahedral. The maximum mesh size is kept smaller than 1/10 of the wavelength for non-particle space. For the particle space, the maximum mesh size is below 1/7 of the particle size. Table 5-1 shows the number of mesh elements for each modeling case of a particle ensemble. Because of the random nature of particle placement in the domain and the domain length, each data shown in the result section was the average of multiple runs (more than 30 runs) for each combination of specific parameters given in above.

Table 5-1. Mesh number for each modeling case for particle ensemble.

Particle diameter	Particle number	Packing density	Mesh elements	Wavelength range
400	90	0.1	~1.0e7	300~1500
300	200	0.1	~1.0e7	300~1500
200	200	0.1	~3.1e6	300~1500
140	200	0.1	~1.2e6	300~1500
100	200	0.1	~5.0e5	300~1500
40	500	0.1	~6.0e5	300~1500
300	30	0.01	~9.0e5	650~1500
140	30	0.01	~1.0e6	300~1500
40	30	0.01	~7.0e4	300~1500

5.2.3 In the case of a single particle

The light scattering by a single particle was also performed for the comparison. Instead of using Mie theory, the computational domain to calculate the light scattering of a single particle is shown in Figure 5-3. A spherical particle made of $Na_{0.74}WO_3$ was placed at the center of the spherical domain. This calculation part justifies using a numerical method instead of Mie's theory.

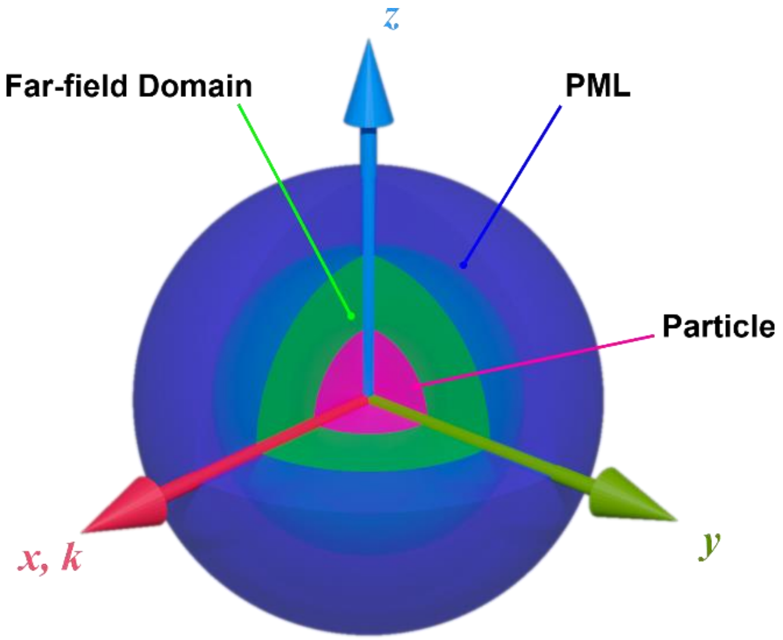

Figure 5-3. Schematic of spherical particle scattering model

The computational domain was divided into two shell layers, i.e., near- and far-field shells. The dimensions of each feature follow Equation 5-6.

$$\begin{cases} t_{FF} = r_p + \frac{1}{2}\lambda \\ t_{PML} = \frac{1}{2}\lambda \end{cases}$$

Equation 5-6

Eq. (1)

Where t_{FF} is the thickness of the far-field domain layer; r_p is the radius of the spherical particle; λ is the wavelength of the scattering wave; t_{PML} is the thickness of the perfect match layer.

All the geometry is in a background scattering plane wave field, traveling in an *x*-axis direction (see Figure 5-3). The scattering cross section is defined in Equation 5-7 [118] as

$$C_{sca} = \frac{W_s}{I_i}$$

Equation 5-7

Eq. (2)

Where C_{sca} is the cross-section of light scattering, W_s is the scattered energy that crosses the particle's surface; I_i is the energy of incident light on the section area of the particle. The absorption cross-section for a particle is definition [118] as Equation 5-8.

$$C_{abs} = \frac{W_a}{I_i}$$

Equation 5-8

Eq. (3)

Where C_{abs} is the cross-section of absorption; W_a is the net (absorbed in our cases) energy that crosses the particle's surface; I_i is the energy rate incident on the section area of the particle. The extinction cross-section C_{ext} can then be calculated [118] as

$$C_{ext} = C_{sca} + C_{abs}$$

Equation 5-9

Eq. (4)

Further, the extinction efficiency Q_{ext}, scattering efficiency Q_{sca}, and absorption efficiency Q_{abs} is shown in Equation 5-10 [118].

$$\begin{cases} Q_{ext} = \dfrac{C_{ext}}{\pi r_p^2} \\ Q_{sca} = \dfrac{C_{sca}}{\pi r_p^2} \\ Q_{abs} = \dfrac{C_{abs}}{\pi r_p^2} \end{cases}$$

Equation 5-10

Eq. (5)

The scattering efficiency Q_{ext} can be normalized by the effective radius a_{eff}, which is equivalent to the radius r_p for a spherical particle. Note that the effective -radius -normalized scattering efficiency Q_{ext}/a_{eff} has the same unit (m^{-1}) as that of the attenuation coefficient, μ_{att}.

In the modeling calculations, the wavelength from 300 nm to 1500 nm is considered for all the cases. Each case's particles in 40, 100, 140, 200, 300, and 400 nm sizes are calculated. The mesh method for each modeling is free tetrahedral. The maximum mesh size is kept smaller than 1/10 of the wavelength for non-particle space. For the particle space, the maximum mesh size is below 1/7 of the particle size. Table 5-2 shows the number of mesh elements for each modeling case of a single particle.

Table 5-2. Mesh number for each modeling case for a single particle.

Particle diameter	Mesh elements	Wavelength range
400	2.3e4	300~1500
300	1.3e4	300~1500
200	8.0e3	300~1500
140	6.8e3	300~1500
100	6.1e3	300~1500
40	6.0e3	300~1500

5.3 For the validation experiment

Experiments were further performed to validate the calculated results. The experimental visible-NIR spectrum for particle-suspended media was measured by the method published in our previous work [126]. The method synthesized sodium tungsten bronze particles using an aerosol-assisted route and size-classified by a MOUDI (micro-orifice uniform deposition impactor). An impactor collects particles via particle inertia (characterized by the particle Stokes number). Nine impaction stages are in a MOUDI. Most of the as-produced particles were collected at the 4th to 9th stages. The cutoff sizes of particles deposited in the above stages are 36 nm, 77 nm, 160 nm, 320 nm, 620 nm, and 1,100 nm. In the light measurement, the media for the particle dispersion was IPA. All the samples were through ultrasound vibration to keep particles well suspended in media immediately before the optical characterization. The attenuation coefficient obtained from the measurement can be normalized by the particle mass concentration as μ_{att}/c (where c is the mass concentration of particles).

5.4 Result and Discussion

5.4.1 Effect of particle size

Figure 5-4 shows the calculated optical performance (i.e., attenuation, absorption, transmission, and reflectance) of an ensemble of sodium tungsten bronze particles in different sizes as a function of the light wavelength. The attenuation coefficient (in Figure 5-4a) shows that the valley of the curves moved towards the longer wavelength regime as the particle size increased, resulting in the increase of attenuation coefficient for the NIR in a longer wavelength (> 1,200 nm) for large particles. The above is more obviously observed in the transmittance curves (in Figure 5-4b), in which the transmittance decreased in a wavelength longer than 1,000 nm. Meanwhile, the transmittance of visible light deteriorates with the increase in particle size. The absorptance curves (in Figure 5-4c) indicate that the NIR shielding performance mostly results from the absorption ability of sodium tungsten bronze because the reflectance (in Figure 5-4d) shows much less light reflected than absorbed. The particles show much-enhanced absorptance in most of the wavelength range with the increase of particle size in Figure 5-4c. The reflectance curves in Figure 5-4d also show that large particles have high reflectance in the wavelength range above 800 nm.

To validate the above observation, experiments were performed to characterize the attenuation coefficient of tungsten bronze particles sized-classified by the MOUID. The result of the attenuation coefficient measurement for an ensemble of sodium tungsten bronze particles is shown in Figure 5-5. It can be found that particles on stage s9 (i.e., the mean size of particles of 77 nm) have reduced NIR shielding than ones collected on stage s8 (mean size of 160 nm). More, for particles collected at the MOUDI's s4 to s6 stages (mean sizes of 1100 nm, 620 nm, and 320 nm, respectively), the NIR shielding increases with the decrease in particle size. To clearly show the variation of the NIR shielding with the particle size, the fraction for transmitted visible and NIR radiation under the solar irradiation for particles in different particle sizes (both calculated and measured) is shown in Figure 5-6. The general trend of both calculated and measured data are consistent in quality. Note that the transmitted fraction of visible and NIR lights under the solar radiation defined herein was based on the definition of solar energy transmittance selectivity (SETS) in Equation 5-11 [62,77,117].

$$SETS = \frac{1}{2}\left(1 + \frac{\int_{UV}^{vis} E(\lambda)T(\lambda)d\lambda}{\int_{UV}^{vis} E(\lambda)d\lambda} - \frac{\int_{vis}^{NIR} E(\lambda)T(\lambda)d\lambda}{\int_{vis}^{NIR} E(\lambda)d\lambda}\right)$$

Equation 5-11

Eq. (6)

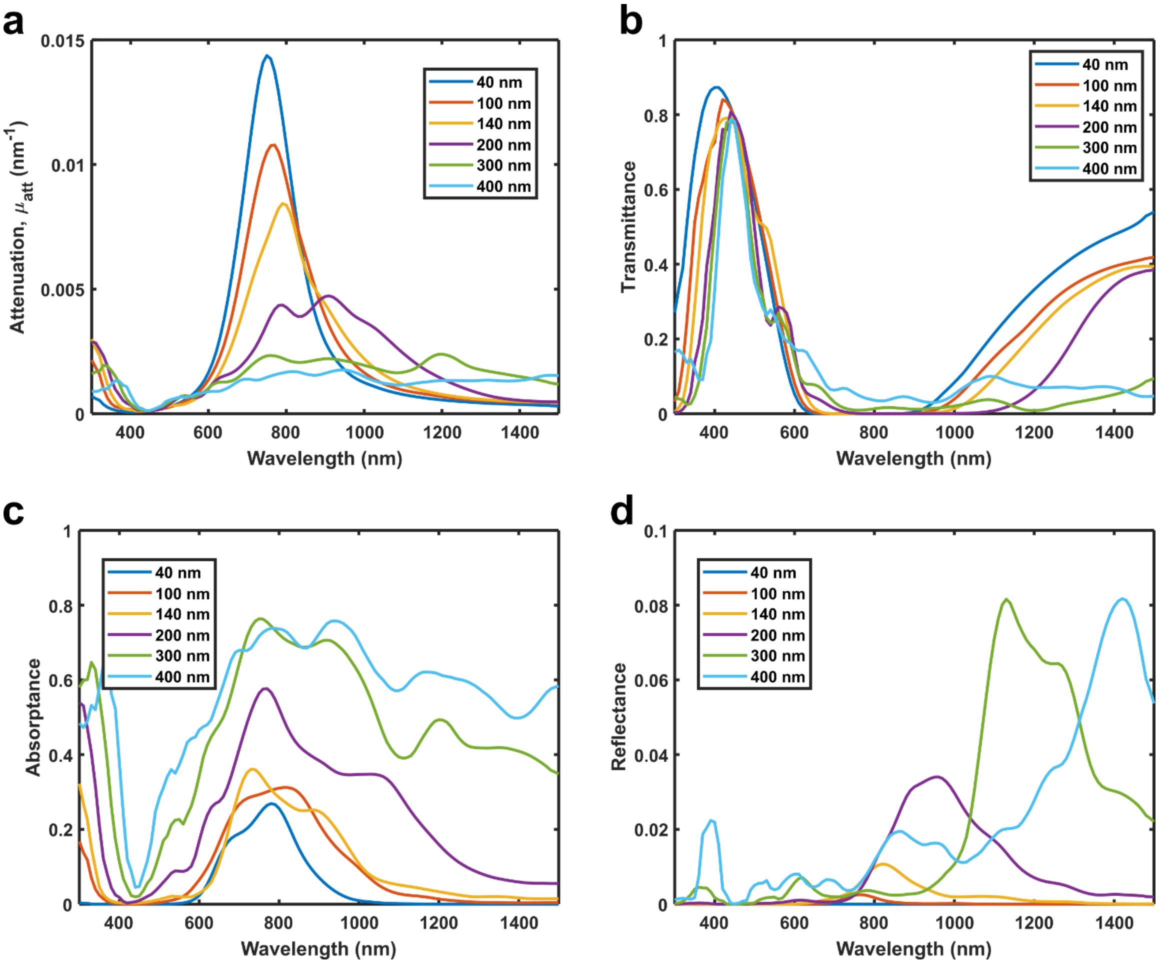

Figure 5-4. The calculated optical performance of an ensemble of sodium tungsten bronze particles in different sizes as the function of light wavelength: (a) for the attenuation coefficient, (b) for the transmittance, (c) for the absorptance, and (d) for the reflectance. The particle density was 0.1. Note that the transmittance, absorptance, and reflectance were normalized by the light path (the thickness of the domain) as 2,000 nm.

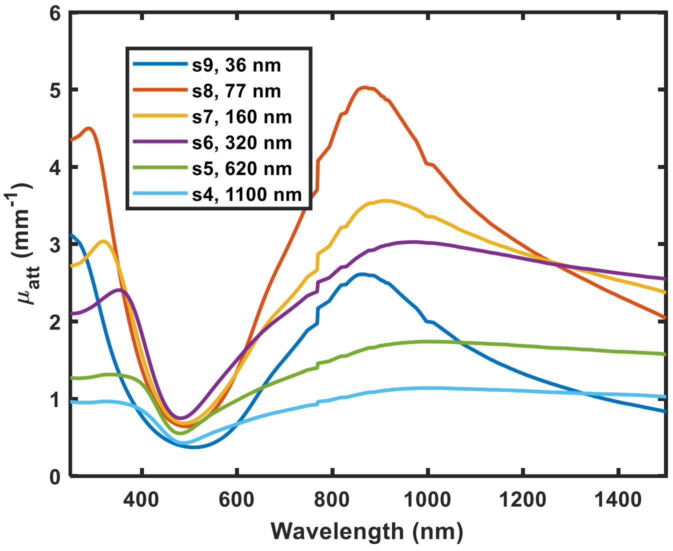

Figure 5-5. Experimental attenuation coefficient of sodium tungsten bronze particles collected on different stages of MOUDI. The mass concentration of particles in the carrying media was kept at 1 mg/mL. The vis-NIR spectrum measurement of particle suspensions was based on the method reported in our previous work [126].

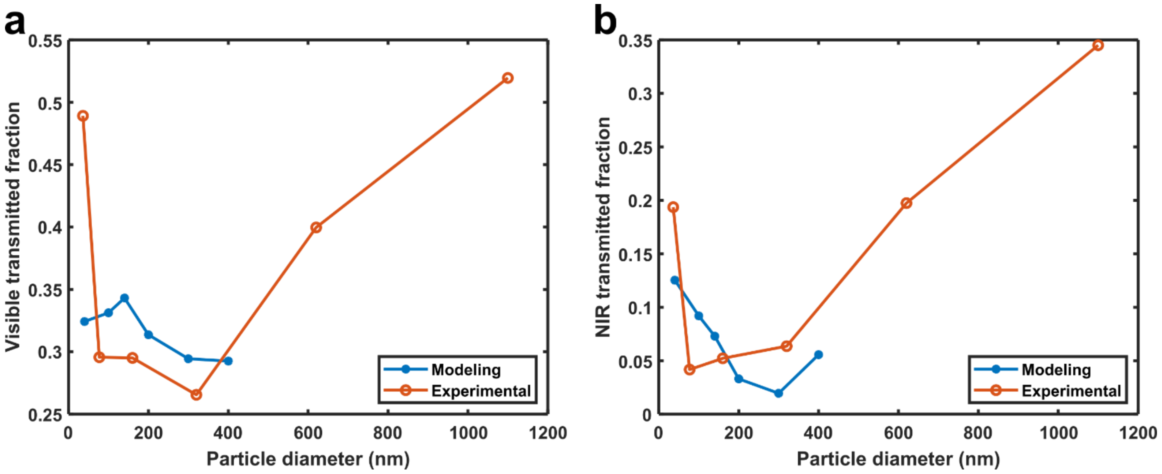

Figure 5-6. The comparison of the calculated and measured fractions of transmitted visible (a) and NIR (b) under solar radiation for particles in different sizes. The calculated transmittance was obtained by normalizing the domain height to 2,000 nm. The thickness of the optical cell used in the measurement was 1 mm.

According to Equation 5-11, we define the visible and NIR light transmitted fractions below.

$$Transmitted\ fraction\ of\ visible\ light = \frac{\int_{UV}^{vis} E(\lambda)T(\lambda)d\lambda}{\int_{UV}^{vis} E(\lambda)d\lambda}$$

Equation 5-12

$$Transmitted\ fraction\ of\ NIR = \frac{\int_{vis}^{NIR} E(\lambda)T(\lambda)d\lambda}{\int_{vis}^{NIR} E(\lambda)d\lambda}$$

Equation 5-13

$E(\lambda)$ comes from the solar irradiance measurement in a standard procedure [127]. Both calculated and measured fractions overlapped in the particle size range of 40 - 400 nm). The calculated transmitted visible radiation (Figure 5-6a) shows the same downturn tendency observed in the experiments. For the transmitted NIR radiation (in Figure 5-6b), both calculated and measured data sets have a turning point as the particle size increased from 40 nm to 400 nm. The above indirectly supports the conclusion that the variation of the NIR shielding for particles in different sizes is largely due to the interaction between the particle size and the irradiance wavelength. Thus, fine particles (mean size of 77 nm) having poor NIR shielding are due to the particle size being much less than the NIR irradiance wavelength.

Because individual ones primarily determine the optical property of a particle ensemble, we further calculated the optics of a single particle under light radiation to determine how a single particle of different sizes interacts with the irradiance. Figure 5-7a shows the extinction efficiency normalized by the effective radius Q_{ext}/a_{eff} (which equals the radius if the particle is spherical). The unit of Q_{ext}/a_{eff}, which is m^{-1}, is the same as that of the attenuation coefficients μ_{att} in the particle ensemble modeling. Compared with the data obtained in the particle ensemble modeling (in Figure 5-4), the Q_{ext}/a_{eff} curves for a single particle (shown in Figure 5-7a) have less difference in the NIR range, particularly for particles in the 300 nm and 400 nm sizes. The particle ensemble modeling shows higher sensitivity on removing NIR in the irradiance for particles of 300 nm to 400 nm. The extinction efficiency Q_{ext} of a single sodium tungsten bronze particle is also given in Figure 5-7b. The peaks of the extinction curves moved towards the red wavelength and became flat as the increase of particle size. In other words, large particles easily interact with long wavelengths. The extinction efficiency of particles composes of scattering and absorption efficiency (shown in Figure 5-7c and d, respectively). It can be found that (1) the scattering efficiency of particles is generally higher than the absorption ones, and (2) the difference in the scattering efficiency as the change of particle size is also larger compared to that for the absorption coefficient. The above finding in single particle modeling contradicts that in particle ensemble modeling.

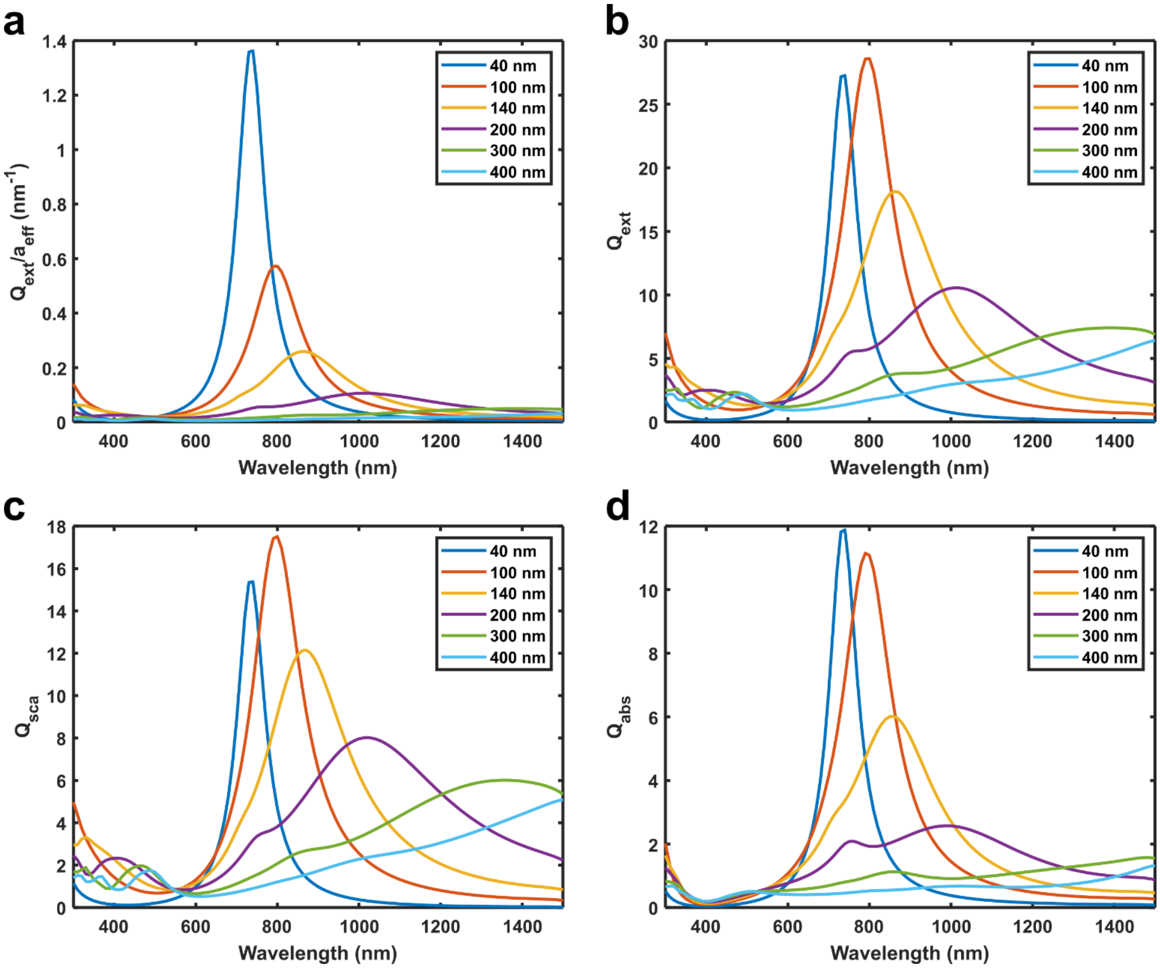

Figure 5-7. The calculated optical performance of single tungsten bronze particles in different sizes: (a) extinction efficiency (normalized by the effective radius of the particle); (b) extinction efficiency, (c) scattering efficiency, and (d) absorption efficiency.

To further evidence the role change of the reflectance (or Q_{sca}) and absorptance (or Q_{abs}) in the particle ensemble (Figure 5-4d and c, respectively) and single particle cases (Figure 5-7c and d, respectively), the ratio of the reflectance (or Q_{sca}) to the absorptance (or Q_{abs}) is calculated in Figure 5-8. It can be found that the ratio value in Figure 5-8a is much lower than in Figure 5-8b. It again indicates that the removal of irradiance beam energy is mostly undertaken by absorption in the particle ensemble modeling, but the removal is mainly done by scattering in the single-particle case. We also found that particles with a large size have higher values for both ratios in the NIR range compared with those for particles of small sizes. The above finding indicates that the particle's reflection (or scattering) increased in the NIR shielding with the particle size increase. One possible explanation for the observed difference between the particle ensemble and single particle cases is that the multiple scattering among particles dramatically increased the chance of the NIR energy absorption. Moreover, NIR absorption is very limited for a single particle when normalized by its size dimension. However, for multiple particles, the differently increased total absorption of NIR can make large differences in each size case. That is why the curve of Q_{ext}/a_{eff} (Figure 5-7a) on the NIR range shows less difference for each size when compared to the μ_{att} (Figure 5-4a).

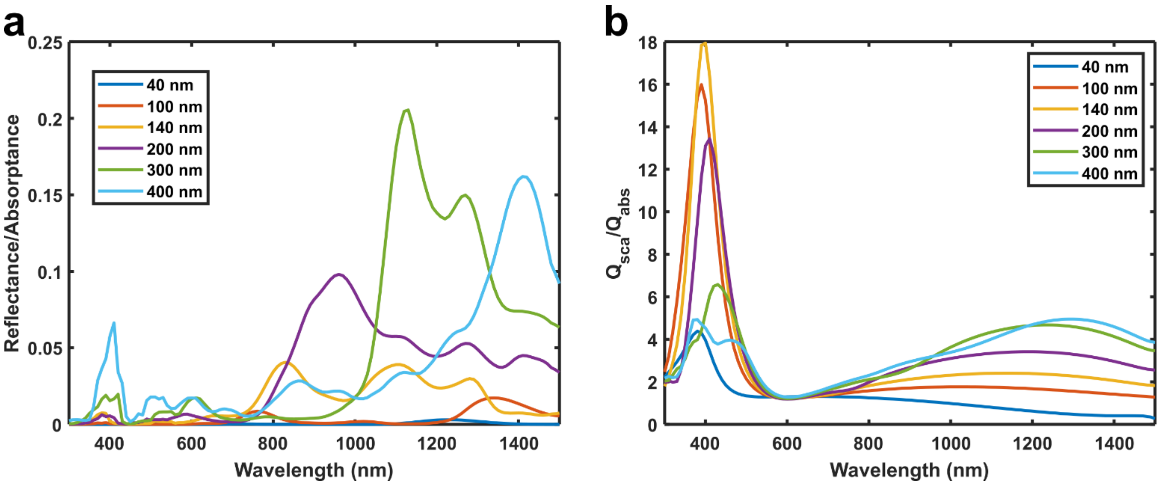

Figure 5-8. (a) The ratio of the reflectance to absorptance (R/A) was obtained in the particle ensemble modeling (in Figure 5-4d and c). (b) The ratio of the scattering efficiency (Q_{sca}) to the absorption efficiency (Q_{abs}) was obtained from a single particle modeling (in Figure 5-7c and d).

Figure 5-9 shows a particle's far-field light scattering pattern in several sizes under a specific wavelength. It is found that the 40 nm-sized particles have scattered radiation mainly in the backward and forward directions at the wavelengths of 420 nm, 730 nm, and 1500 nm (Figure 5-9a, b, and c). A particle in 140 nm also shows a similar scattering pattern for the 1500 nm wavelength (Figure 5-9f). If the energy in the scattering direction is largely in the backward or forward directions, the scattered radiation would have less opportunity to encounter another particle in the particle ensemble cases since the limited spreading in the scattering direction. However, for a particle in the 300 nm diameter, the scattering direction is widely spread for the wavelength of 1,390 nm and 1,500 nm (on the back hemisphere and both sides), which can increase the chance of encountering other particles. The above is also why the ratios of R/A (in Figure 5-8a) in the NIR range for a large particle are higher than those for small particles.

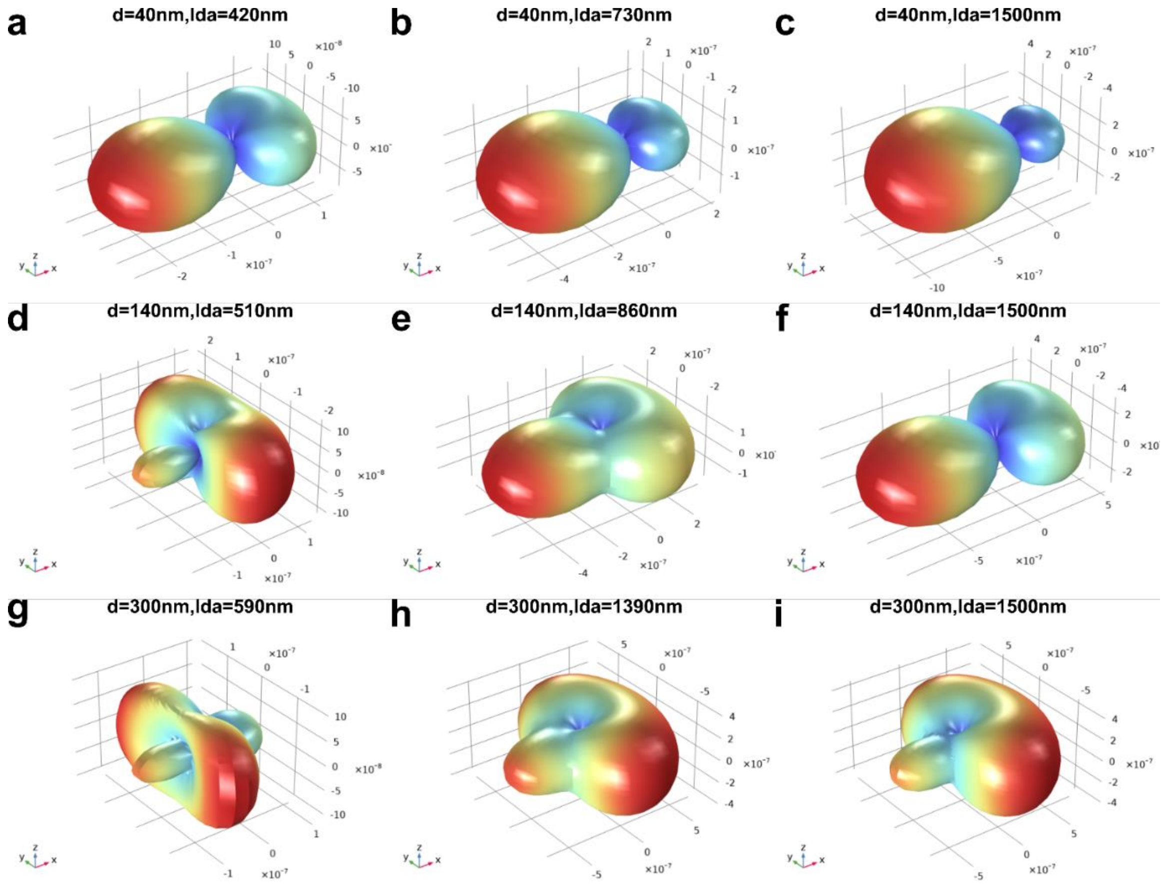

Figure 5-9. The calculated light scattering pattern in the far field of a single particle. The wave-traveling direction of waves is in the x-axis. In the first column, (a), (d), and (g) are for the cases with the particle having the minimum extinction in the visible light range. The second column, (b), (e), and (h), are for the cases having the maximum extinction in the NIR range. The third column, (c), (f), and (i), are for the cases with the upper limit of the wavelength (i.e., 1,500 nm) in the modeling.

5.4.2 Effect of particle density (or concentration)

To support the hypothesis of multiple particles increasing the absorption of NIR scattered energy, we performed the particle ensemble modeling at two different particle densities (0.01 and 0.1) for particles of different sizes. The results of our calculation are shown in Figure 5-10. It is found that, for 40nm particles, the low packing density case has the higher attenuation coefficient curve (μ_{att}/p) in the 600 nm to 800 nm wavelength range (which is partially corresponding to the measured data in Figure 5-11d), but the attenuation in two packing density cases is at the same level for 300nm particles (which is close to the particle size in Figure 5-11a). It indicates that the effect of multi-scattering in different particle packing densities is the reason for the role change in the NIR absorption.

Figure 5-10b, c, and d show the ratio of reflectance to absorptance of particles in two different volumetric packing densities. It is found that small particles (40 nm) in a lower packing density ($p = 0.01$) largely have a lower value of R/A ratio than that in a higher packing density ($p = 0.1$), particularly in the NIR range. For particles in the 140 nm size, the curves of the R/A ratio for two different packing densities became close to each other as the wavelength increased and eventually crossed each other in the NIR range. Moreover, for particles in the 300 nm size, the R/A curve for the $p = 0.01$ case is over that for the $p = 0.1$ cases in most of the NIR range. It can thus be expected that, for particles with a larger size, the R/A curve for the $p = 0.01$ case would be much higher than that for the $p = 0.1$ cases in the NIR range. Given the result shown in Figure 5-8a, it is found that particles with a large size would have a higher fraction of reflection in removing NIR incident energy. At a fixed mass concentration of particles, the average distance between two particles increases with particle size increase. Under the above condition, the multiple light scattering effect should decline with particle size increase. The increased absorption resulting from the multiple light scattering effects is also expected to decrease. When the average distance among particles is much larger than the irradiance wavelength, the situation would be like single-particle scattering.

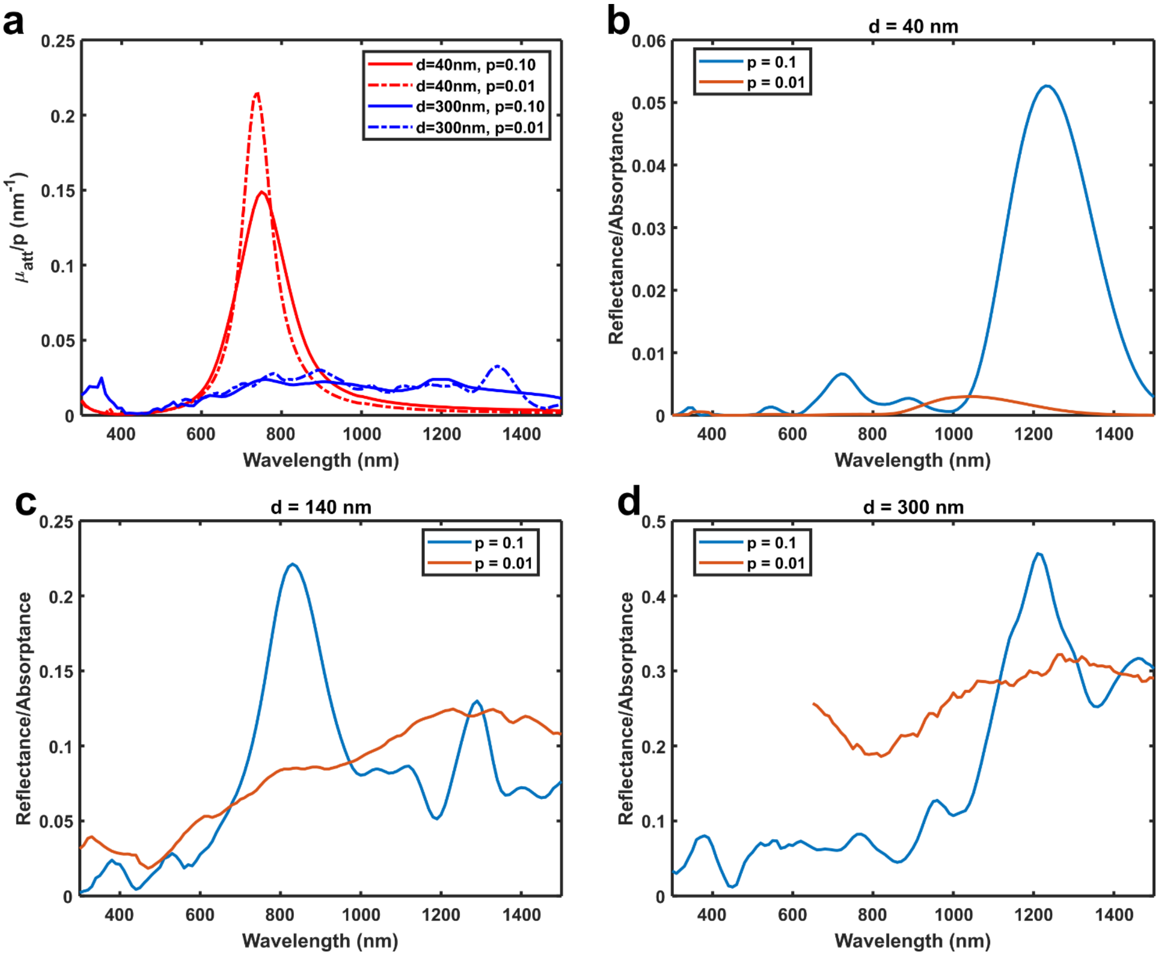

Figure 5-10. (a) The calculated attenuation coefficient (normalized by the particle packing density) of multiple particles in 40 nm and 300 nm diameters and at the particle packing density of p = 0.01 and p = 0.1. The ratio of the reflectance to absorptance (R/A) obtained from the particle multiple ensemble modeling (at the particle packing densities of 0.01 and 0.1) for particles in the diameters of 40 nm (b), 140 nm (c), and 300 nm (d).

To further support the above modeling result, the optical characterization of particle samples collected at the MOUDI stages s6 to s9 was performed at three different particle mass concentrations (i.e., 0.1, 1.0, and 10 mg/mL). The result of the optical characterization is given in Figure 5-11. It is found that for particles on the MOUDI stages s9 to s6 (in

Figure 5-11d, c, b, and a, respectively), the higher the particle mass concentration, the lower the attenuation coefficients (μ_{att}/c) in the NIR wavelength range. It indicates that the interaction of particles with the NIR decreased with the decrease in particle concentration. As shown in Figure 5-8b, the ratio of Q_{sca}/Q_{abs} increases with particle size increase in the NIR wavelength range. The multiple particle scattering can also increase the overall light scattering in the forward direction (i.e., less NIR shielding for each particle) at a high particle concentration (i.e., the reduced intraparticle distance). The difference between the cases of small and large particles is that, for the particles in small sizes (less than 320 nm), the total forward scattering increase is not comparable to the absorption increase. It is why particles from MOUDI stages s6, s7, s8, and s9 share the same tendency: the higher the particle concentration, the lower the normalized attenuation coefficient.

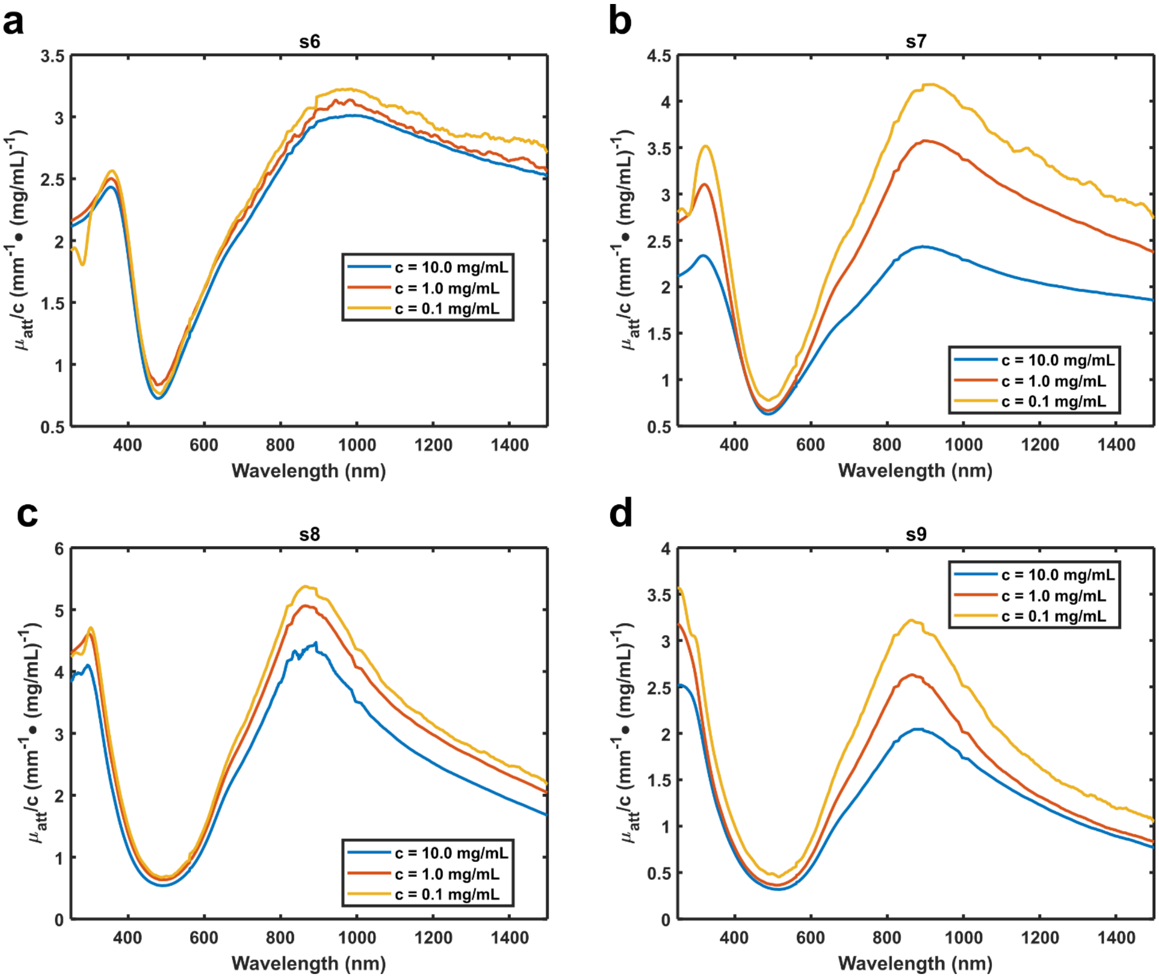

Figure 5-11. The measured light attenuation coefficient (normalized by particle mass concentration) for the suspension of $Na_{0.7}WO_3$ particles collected on different stages of MOUDI. The mean size of particles collected on each MOUDI stage is 320 nm (s6), 160 nm (s7), 77 nm (s8), and 36 nm (s9). The particle mass concentration in the suspension is in the unit volume of carry media.

5.4.3 Effect of particle shape

Figure 5-12 shows the spectrum result of cubic sodium tungsten bronze particles compared to the spherical one. The cubic and spherical particles share the same volumetric diameter of 140 nm. The cubic particle shows a higher attenuation on NIR, as shown in Figure 5-12a. The transmittance in Figure 5-12b also shows the stronger shielding on the wavelength beyond 1000 nm. As shown in Figure 5-12c, the absorptance spectrum demonstrates that most enhanced NIR shielding comes from the absorption, other than the reflectance. Because the value of reflectance in Figure 5-12d is much lower than the absorptance in Figure 5-12c. Thus, multiple scattering enhanced NIR shielding for cubic particles more than the spherical one. The localized surface plasmon resonance (LSPR) gives the sharp corner and edge a more intensified electric field on the surface than the spherical one 114, enabling the cubic nanoparticles to absorb the more specific NIR radiation.

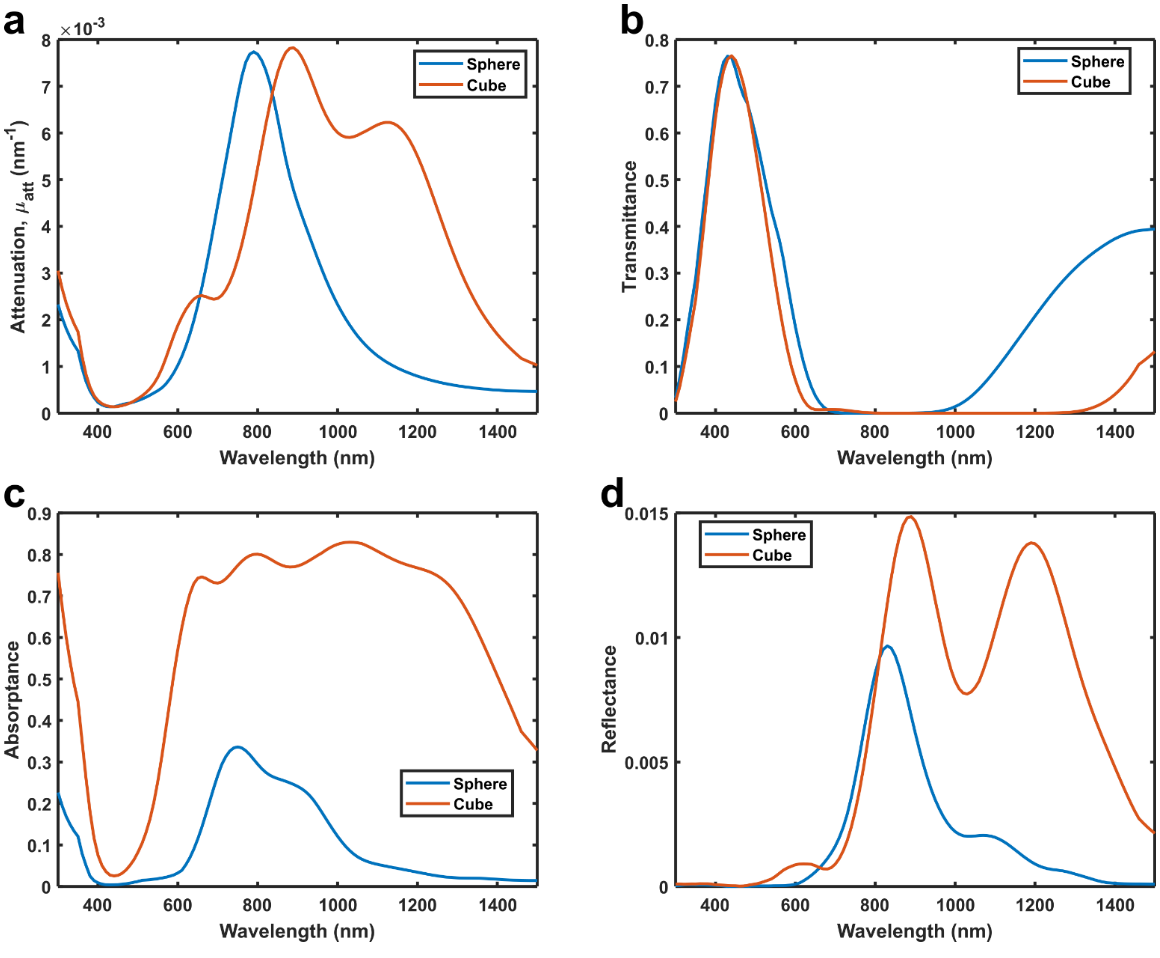

Figure 5-12. The calculated optical performance of an ensemble of cubic and spherical sodium tungsten bronze particles in 140 nm as the function of light wavelength: (a) for the attenuation coefficient, (b) for the transmittance, (c) for the absorptance, and (d) for the reflectance. The particle density was 0.1. Note that the transmittance, absorptance, and reflectance were normalized by the light path (the thickness of the domain) as 2,000 nm.

Moreover, for the other sizes of particles, Figure 5-13 shows both cubic and spherical sodium tungsten bronze particles in several sizes. For each size from 40 to 400 nm, the cubic particles always show a high attenuation in the NIR range, especially for the smaller particles. The difference between the same size of spherical and cubic particles becomes smaller with the increasing particle size. Further, the curve peak for the cubic particles moves to the red side than the spherical ones. Among the cubic particles, the particles of the larger sizes show enhanced shielding in the long wavelength NIR range, which is the same as the spherical ones in different sizes.

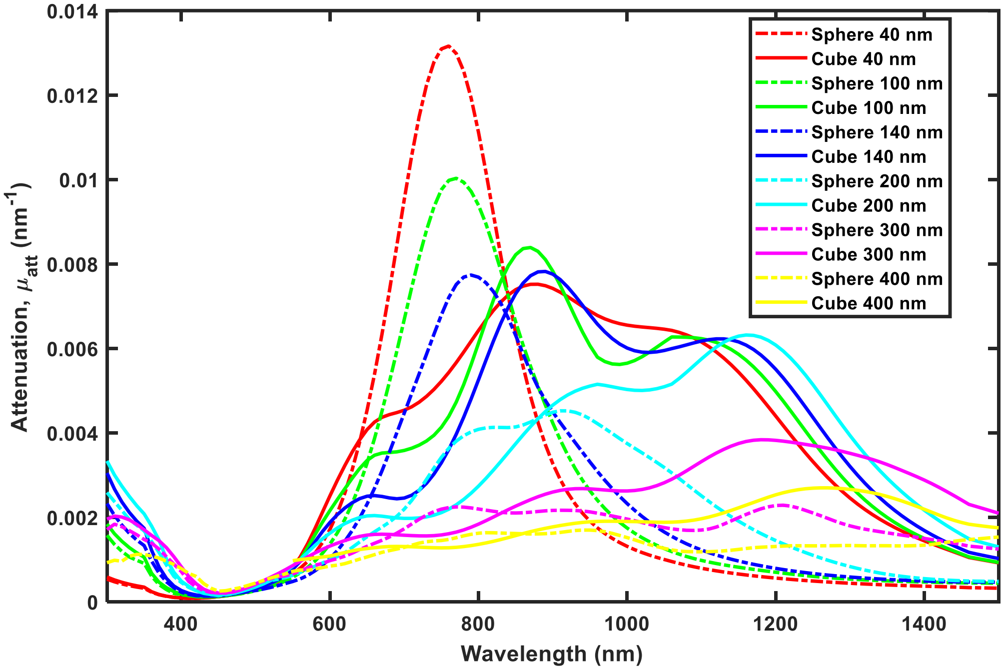

Figure 5-13. Comparison of the calculated optical performance of an ensemble of cubic and spherical sodium tungsten bronze particles in 40, 100, 140, 200, 300, and 400 nm as the function of light wavelength.

5.5 Conclusion

In conclusion, we compare particle ensemble and a single particle of $Na_{0.7}WO_3$ modeling results to investigate the size, concentration, and shape effect on NIR shielding for sodium tungsten bronze. The experimental results in different particle sizes and concentrations confirm the modeling result. The tendency of modeling results on the integral of shielded NIR can follow the experimental result.

The multiple scattering between particles in the particle ensemble can greatly increase the absorption of NIR. This enhancement of NIR absorption is much higher than the reflection part, especially for the smaller particles. Under different concentrations, the ratio of the reflectance to absorptance on the NIR range for small particles at low concentrations is lower than at the high concentration. While for the large particle, the difference between the high and low concentrations cases is not so obvious. That means the smaller particle has a better mass efficiency for NIR shielding at a lower concentration. The experiment result also evidences it for the sodium tungsten bronze particles below 320 nm, the better mass efficiency for NIR shielding was achieved at the lower concentration. As for the sodium tungsten bronze particle's shape, the cubic shape shows better NIR shielding than the spherical ones due to the higher enhancement of NIR absorption intensified by the multi-scattering.

Chapter 6. Conclusion and future works

6.1 Experimental setups in the aerosol synthesis of tungsten bronze particles

We introduced the main setups used in our experiment to synthesize tungsten bronze particles. The setups have various components to control the flow rate, the moisture, the carrier gas, the precursor aerosol, and the corrosion. The dilution flow has a minor effect on the particle size. An example of a droplet-assisted synthesis process to produce sodium tungsten bronze particles in one step is given. The precursor droplets vaporize and crystallize in the tube furnace.

6.2 Precursors and solvents in the aerosol synthesis of tungsten bronze particles

Then, we explored how different precursors/solvents affect the tungsten bronze particles. The alkali species in the precursor determines the type of tungsten bronze. The same atomic ratio of M/W (M = Na, K, and Cs) can produce similar products with different solvents. Some examples of solvents and reagents are given. The water-based precursor solution produces high-quality tungsten bronze particles for different alkali species. We also studied how moisture concentration and heating temperature influence the quality of sodium tungsten bronze particles from the methanol-based precursor. The quality depends on the sodium content in the precursor solution. Higher sodium content and higher furnace temperature improve the quality. Enough moisture reduces the byproduct.

The particle formation and chemical reaction in the process are also included. The methanol solvent evaporates and acts as a reductive regent to help particle crystallization.

The Na/W ratio in the precursor solution affects the phase and purity of the sodium tungsten bronze particles. The cubic phase ($Na_{0.70}WO_3$) particles have higher visibility and lower impurity than the tetragonal phase ($Na_{0.57}WO_3$) particles. Both phases can shield NIR light.

6.3 Effect of particle size on NIR shielding

We completed the production and characterization of sodium tungsten bronze particles by an aerosol-assisted process. The particles have high purity and crystallinity and can shield NIR light. The particle size distribution and the optical transmittance of size-selected particle samples were measured by MOUDI and SETS index. The optimal size range for NIR shielding and visible light transmittance was determined. The optical modeling explained the NIR shielding loss for small particles.

6.4 Optic modeling of tungsten bronze particles

We investigated the comparison of particle ensemble and single particle modeling for sodium tungsten bronze and its effect on NIR shielding. The modeling results are consistent with the experimental results for different particle sizes and concentrations. The multiple scattering increases the NIR absorption more than the reflection, especially for smaller particles. Smaller particles have better mass efficiency for NIR shielding at lower concentrations. Cubic particles have better NIR shielding than spherical ones because of more multi-scattering.

6.5 Suggestions for future research

As for the aerosol synthesis of tungsten bronze particles, even though we can synthesize the particles only via the water solvent and cheap precursor, the particles' size cannot be tuned in existed setup. If dilution flow cannot make the size of particles tunable, synthesizing the particles at low pressure close to a vacuum in a vertical setup may work because, without the thermal and gravity interpretation, the growth of the nanocrystals can be more controllable.

In the NIR shielding application in practice, the diameter of each particle follows some distribution for the ensemble of particles. Moreover, the shape of the particles differs from each other. Thus, particle optical modeling can be more precise if the particles' size and shape are modeled based on some distributions.

Reference

(1) Murdock, H. E.; Gibb, D.; André, T.; Sawin, J. L.; Brown, A.; Ranalder, L.; Collier, U.; Dent, C.; Epp, B.; Hareesh Kumar, C.; others. Renewables 2021-Global Status Report. **2021**.

(2) *Use of electricity - U.S. Energy Information Administration (EIA)*. https://www.eia.gov/energyexplained/electricity/use-of-electricity.php (accessed 2023-03-02).

(3) Astm, G. 173–03: Standard Tables for Reference Solar Spectral Irradiances: Direct Normal and Hemispherical on 37 Tilted Surface. *ASTM International* **2020**.

(4) *Update or Replace Windows*. Energy.gov. https://www.energy.gov/energysaver/update-or-replace-windows (accessed 2023-03-02).

(5) *Solar Control Glass Market Size | Global Industry Report, 2016-2024*. https://www.grandviewresearch.com/industry-analysis/solar-control-glass (accessed 2023-03-02).

(6) Adachi, K.; Asahi, T. Activation of Plasmons and Polarons in Solar Control Cesium Tungsten Bronze and Reduced Tungsten Oxide Nanoparticles. *Journal of Materials Research*, 2012, *27*, 965–970. https://doi.org/10.1557/jmr.2012.25.

(7) Hutter, E.; Fendler, J. H. Exploitation of Localized Surface Plasmon Resonance. *Advanced Materials* **2004**, *16* (19), 1685–1706. https://doi.org/10.1002/adma.200400271.

(8) Link, S.; El-Sayed, M. A. Spectral Properties and Relaxation Dynamics of Surface Plasmon Electronic Oscillations in Gold and Silver Nanodots and Nanorods. *J. Phys. Chem. B* **1999**, *103* (40), 8410–8426. https://doi.org/10.1021/jp9917648.

(9) Garcia, G.; Buonsanti, R.; Llordes, A.; Runnerstrom, E. L.; Bergerud, A.; Milliron, D. J. Near-Infrared Spectrally Selective Plasmonic Electrochromic Thin Films. *Advanced Optical Materials* **2013**, *1* (3), 215–220. https://doi.org/10.1002/adom.201200051.

(10) Chen, W.; Thoreson, M. D.; Ishii, S.; Kildishev, A. V.; Shalaev, V. M. Ultra-Thin Ultra-Smooth and Low-Loss Silver Films on a Germanium Wetting Layer. *Opt. Express* **2010**, *18* (5), 5124. https://doi.org/10.1364/OE.18.005124.

(11) Miao, D.; Jiang, S.; Shang, S.; Chen, Z. Infrared Reflective Properties of AZO/Ag/AZO Trilayers Prepared by RF Magnetron Sputtering. *Ceramics International* **2014**, *40* (8), 12847–12853. https://doi.org/10.1016/j.ceramint.2014.04.139.

(12) Weber, M. F.; Stover, C. A.; Gilbert, L. R.; Nevitt, T. J.; Ouderkirk, A. J. Giant Birefringent Optics in Multilayer Polymer Mirrors. *Science, New Series* **2000**, *287* (5462), 2451–2456.

(13) Zheng, L.; Xiong, T.; Shah, K. W. Transparent Nanomaterial-Based Solar Cool Coatings: Synthesis, Morphologies and Applications. *Solar Energy* **2019**, *193*, 837–858. https://doi.org/10.1016/j.solener.2019.10.029.

(14) Jiang, C.; Cheng, M.; Liu, H.; Shao, L.; Zeng, X.; Zhang, Y.; Shi, F. Fabricating Transparent Multilayers with UV and Near-IR Double-Blocking Properties through

Layer-by-Layer Assembly. *Industrial & Engineering Chemistry Research*, 2013, *52*, 13393–13400. https://doi.org/10.1021/ie401769h.

(15) Tani, T.; Hakuta, S.; Kiyoto, N.; Naya, M. Transparent Near-Infrared Reflector Metasurface with Randomly Dispersed Silver Nanodisks. *Opt. Express* **2014**, *22* (8), 9262. https://doi.org/10.1364/OE.22.009262.

(16) Kiomarsipour, N.; Shoja Razavi, R. Hydrothermal Synthesis of ZnO Nanopigments with High UV Absorption and Vis/NIR Reflectance. *Ceramics International* **2014**, *40* (7), 11261–11268. https://doi.org/10.1016/j.ceramint.2014.03.178.

(17) Wu, X.; Yin, S.; Xue, D.; Komarneni, S.; Sato, T. A CsxWO3/ZnO Nanocomposite as a Smart Coating for Photocatalytic Environmental Cleanup and Heat Insulation. *Nanoscale*, 2015, *7*, 17048–17054. https://doi.org/10.1039/C5NR04452A.

(18) Soumya, S.; Mohamed, A. P.; Paul, L.; Mohan, K.; Ananthakumar, S. Near IR Reflectance Characteristics of PMMA/ZnO Nanocomposites for Solar Thermal Control Interface Films. *Solar Energy Materials and Solar Cells* **2014**, *125*, 102–112. https://doi.org/10.1016/j.solmat.2014.02.033.

(19) Li, Y.-Q.; Kang, Y.; Xiao, H.-M.; Mei, S.-G.; Zhang, G.-L.; Fu, S.-Y. Preparation and Characterization of Transparent Al Doped ZnO/Epoxy Composite as Thermal-Insulating Coating. *Composites Part B: Engineering* **2011**, *42* (8), 2176–2180. https://doi.org/10.1016/j.compositesb.2011.05.015.

(20) Soumya, S.; Mohamed, A. P.; Mohan, K.; Ananthakumar, S. Enhanced Near-Infrared Reflectance and Functional Characteristics of Al-Doped ZnO Nano-Pigments Embedded PMMA Coatings. *Solar Energy Materials and Solar Cells* **2015**, *143*, 335–346. https://doi.org/10.1016/j.solmat.2015.07.012.

(21) Zubizarreta, C.; Berasategui, E. G.; Bayón, R.; Escobar Galindo, R.; Barros, R.; Gaspar, D.; Nunes, D.; Calmeiro, T.; Martins, R.; Fortunato, E.; Barriga, J. Evaluation of the Optoelectronic Properties and Corrosion Behavior of Al2O3-Doped ZnO Films Prepared by Dc Pulsed Magnetron Sputtering. *J. Phys. D: Appl. Phys.* **2014**, *47* (48), 485501. https://doi.org/10.1088/0022-3727/47/48/485501.

(22) Miao, D.; Hu, H.; Gan, L. Fabrication of High Infrared Reflective Al-Doped ZnO Thin Films Through Electropulsing Treatment for Solar Control. *Journal of Alloys and Compounds* **2015**, *639*, 400–405. https://doi.org/10.1016/j.jallcom.2015.03.189.

(23) Luo, Y.-S.; Yang, J.-P.; Dai, X.-J.; Yang, Y.; Fu, S.-Y. Preparation and Optical Properties of Novel Transparent Al-Doped-ZnO/Epoxy Nanocomposites. *J. Phys. Chem. C* **2009**, *113* (21), 9406–9411. https://doi.org/10.1021/jp901501z.

(24) Ni, J.; Zhao, Q.; Zhao, X. Transparent and High Infrared Reflection Film Having Sandwich Structure of SiO2/Al:ZnO/SiO2. *Progress in Organic Coatings* **2009**, *64* (2–3), 317–321. https://doi.org/10.1016/j.porgcoat.2008.08.030.

(25) Buonsanti, R.; Llordes, A.; Aloni, S.; Helms, B. A.; Milliron, D. J. Tunable Infrared Absorption and Visible Transparency of Colloidal Aluminum-Doped Zinc Oxide Nanocrystals. *Nano Lett.* **2011**, *11* (11), 4706–4710. https://doi.org/10.1021/nl203030f.

(26) Trenque, I.; Gaudon, M.; Duguet, E.; Mornet, S. Visible-Transparent and UV/IR-Opaque Colloidal Dispersions of Ga-Doped Zinc Oxide Nanoparticles. *New J. Chem.* **2016**, *40* (8), 7204–7209. https://doi.org/10.1039/C6NJ01668E.

(27) Ma, Q.-B.; Ye, Z.-Z.; He, H.-P.; Zhu, L.-P.; Huang, J.-Y.; Zhang, Y.-Z.; Zhao, B.-H. Influence of Annealing Temperature on the Properties of Transparent Conductive and Near-Infrared Reflective ZnO:Ga Films. *Scripta Materialia* **2008**, *58* (1), 21–24. https://doi.org/10.1016/j.scriptamat.2007.09.009.

(28) Li, Y.; Ji, S.; Gao, Y.; Luo, H.; Kanehira, M. Core-Shell VO2@TiO2 Nanorods That Combine Thermochromic and Photocatalytic Properties for Application as Energy-Saving Smart Coatings. *Sci Rep* **2013**, *3* (1), 1370. https://doi.org/10.1038/srep01370.

(29) Gao, Y.; Wang, S.; Kang, L.; Chen, Z.; Du, J.; Liu, X.; Luo, H.; Kanehira, M. VO2–Sb:SnO2 Composite Thermochromic Smart Glass Foil. *Energy Environ. Sci.* **2012**, *5* (8), 8234. https://doi.org/10.1039/c2ee21119j.

(30) Chew, C.; Bishop, P.; Salcianu, C.; Carmalt, C. J.; Parkin, I. P. Aerosol-Assisted Deposition of Gold Nanoparticle-Tin Dioxide Composite Films. *RSC Adv.* **2014**, *4* (25), 13182–13190. https://doi.org/10.1039/C3RA46828C.

(31) Liu, J.; Lu, Y.; Liu, J.; Yang, X.; Yu, X. Investigation of near Infrared Reflectance by Tuning the Shape of SnO2 Nanoparticles. *Journal of Alloys and Compounds* **2010**, *496* (1–2), 261–264. https://doi.org/10.1016/j.jallcom.2010.01.053.

(32) Sequinel, T.; Cava, S.; Pimenta, J. O.; Pianaro, S. A.; Tebcherani, S. M.; Varela, J. A. IR Reflectance Characterization of Glass–Ceramic Films Obtained by High Pressure Impregnation of SnO2 Nanopowders on Float Glass. *Ceramics International* **2011**, *37* (5), 1533–1536. https://doi.org/10.1016/j.ceramint.2011.01.013.

(33) Shen, B.; Wang, Y.; Lu, L.; Yang, H. Spraying Fabrication of Spectrally Selective Coating with Improved Near-Infrared Shielding Performance for Energy-Efficient Glazing. *Ceramics International*, 2021. https://doi.org/10.1016/j.ceramint.2021.03.243.

(34) Wang, X.; Hu, Y.; Song, L.; Xing, W.; Lu, H.; Lv, P.; Jie, G. Effect of Antimony Doped Tin Oxide on Behaviors of Waterborne Polyurethane Acrylate Nanocomposite Coatings. *Surface and Coatings Technology*, 2010, *205*, 1864–1869. https://doi.org/10.1016/j.surfcoat.2010.08.053.

(35) Feng, J.; Huang, B.; Zhong, M. Fabrication of Superhydrophobic and Heat-Insulating Antimony Doped Tin Oxide/Polyurethane Films by Cast Replica Micromolding. *Journal of Colloid and Interface Science*, 2009, *336*, 268–272. https://doi.org/10.1016/j.jcis.2009.03.025.

(36) Wang, L.; Hang, J.; Shi, L.; Sun, X.; Xu, F. Preparation and Characterization of NIR Cutoff Antimony Doped Tin Oxide/Hybrid Silica Coatings. *Materials Letters*, 2012, *87*, 35–38. https://doi.org/10.1016/j.matlet.2012.07.065.

(37) Koebel, M. M.; Nadargi, D. Y.; Jimenez-Cadena, G.; Romanyuk, Y. E. Transparent, Conducting ATO Thin Films by Epoxide-Initiated Sol–Gel Chemistry: A Highly Versatile Route to Mixed-Metal Oxide Films. *ACS Applied Materials & Interfaces*, 2012, *4*, 2464–2473. https://doi.org/10.1021/am300143z.

(38) Li, Y.; Liu, J.; Liang, J.; Yu, X.; Li, D. Tunable Solar-Heat Shielding Property of Transparent Films Based on Mesoporous Sb-Doped SnO2 Microspheres. *ACS Appl. Mater. Interfaces* **2015**, *7* (12), 6574–6583. https://doi.org/10.1021/am508711p.

(39) Liu, H.; Zeng, X.; Kong, X.; Bian, S.; Chen, J. A Simple Two-Step Method to Fabricate Highly Transparent ITO/Polymer Nanocomposite Films. *Applied Surface Science*, 2012, *258*, 8564–8569. https://doi.org/10.1016/j.apsusc.2012.05.049.

(40) Williams, T. E.; Chang, C. M.; Rosen, E. L.; Garcia, G.; Runnerstrom, E. L.; Williams, B. L.; Koo, B.; Buonsanti, R.; Milliron, D. J.; Helms, B. A. NIR-Selective Electrochromic Heteromaterial Frameworks: A Platform to Understand Mesoscale Transport Phenomena in Solid-State Electrochemical Devices. *Journal of Materials Chemistry C*, 2014, *2*, 3328–3335. https://doi.org/10.1039/C3TC32247E.

(41) Tao, P.; Viswanath, A.; Schadler, L. S.; Benicewicz, B. C.; Siegel, R. W. Preparation and Optical Properties of Indium Tin Oxide/Epoxy Nanocomposites with Polyglycidyl Methacrylate Grafted Nanoparticles. *ACS Applied Materials & Interfaces*, 2011, *3*, 3638–3645. https://doi.org/10.1021/am200841n.

(42) Song, J. E.; Kim, Y. H.; Kang, Y. S. Preparation of Indium Tin Oxide Nanoparticles and Their Application to near IR-Reflective Film. *Current Applied Physics*, 2006, *6*, 791–795. https://doi.org/10.1016/j.cap.2005.04.041.

(43) Tang, H.; Su, Y.; Hu, T.; Liu, S.; Mu, S.; Xiao, L. Synergetic Effect of LaB6 and ITO Nanoparticles on Optical Properties and Thermal Stability of Poly(Vinylbutyral) Nanocomposite Films. *Appl. Phys. A* **2014**, *117* (4), 2127–2132. https://doi.org/10.1007/s00339-014-8632-8.

(44) Llordés, A.; Garcia, G.; Gazquez, J.; Milliron, D. J. Tunable Near-Infrared and Visible-Light Transmittance in Nanocrystal-in-Glass Composites. *Nature*, 2013, *500*, 323–326. https://doi.org/10.1038/nature12398.

(45) Chavez-Galan, J.; Almanza, R. Solar Filters Based on Iron Oxides Used as Efficient Windows for Energy Savings. *Solar Energy*, 2007, *81*, 13–19. https://doi.org/10.1016/j.solener.2006.06.009.

(46) Song, J.; Qin, J.; Qu, J.; Song, Z.; Zhang, W.; Xue, X.; Shi, Y.; Zhang, T.; Ji, W.; Zhang, R.; Zhang, H.; Zhang, Z.; Wu, X. The Effects of Particle Size Distribution on the Optical Properties of Titanium Dioxide Rutile Pigments and Their Applications in Cool Non-White Coatings. *Solar Energy Materials and Solar Cells* **2014**, *130*, 42–50. https://doi.org/10.1016/j.solmat.2014.06.035.

(47) Messing, G. L.; Zhang, S.-C.; Jayanthi, G. V. Ceramic Powder Synthesis by Spray Pyrolysis. *J American Ceramic Society* **1993**, *76* (11), 2707–2726. https://doi.org/10.1111/j.1151-2916.1993.tb04007.x.

(48) Adachi, K.; Miratsu, M.; Asahi, T. Absorption and Scattering of Near-Infrared Light by Dispersed Lanthanum Hexaboride Nanoparticles for Solar Control Filters. *J. Mater. Res.* **2010**, *25* (3), 510–521. https://doi.org/10.1557/JMR.2010.0075.

(49) Takeda, H.; Kuno, H.; Adachi, K. Solar Control Dispersions and Coatings With Rare-Earth Hexaboride Nanoparticles. *Journal of the American Ceramic Society* **2008**, *91* (9), 2897–2902. https://doi.org/10.1111/j.1551-2916.2008.02512.x.

(50) Owen, J. F.; Teegarden, K. J.; Shanks, H. R. Optical Properties of the Sodium-Tungsten Bronzes and Tungsten Trioxide. *Phys. Rev. B* **1978**, *18* (8), 3827–3837. https://doi.org/10.1103/PhysRevB.18.3827.

(51) Schimmoeller, B.; Pratsinis, S. E.; Baiker, A. Flame Aerosol Synthesis of Metal Oxide Catalysts with Unprecedented Structural and Catalytic Properties. *ChemCatChem* **2011**, *3* (8), 1234–1256. https://doi.org/10.1002/cctc.201000425.

(52) Yang, C.; Chen, J.-F.; Zeng, X.; Cheng, D.; Cao, D. Design of the Alkali-Metal-Doped WO3 as a Near-Infrared Shielding Material for Smart Window. *Ind. Eng. Chem. Res.* **2014**, *53* (46), 17981–17988. https://doi.org/10.1021/ie503284x.

(53) Tu, H.; Wang, W.; Chen, D.-R. Aerosol-Assisted Production of NIR Shielding Nanoparticles: Sodium Tungsten Bronze. *Aerosol Air Qual. Res.* **2020**, *20* (4), 690–701. https://doi.org/10.4209/aaqr.2019.10.0548.

(54) Guo, C.; Yin, S.; Sato, T. Effects of Crystallization Atmospheres on the Near-Infrared Absorbtion and Electroconductive Properties of Tungsten Bronze Type MxWO3 (M = Na,K). *J. Am. Ceram. Soc.* **2012**, *95* (5), 1634–1639. https://doi.org/10.1111/j.1551-2916.2011.05039.x.

(55) Luo, J. Y.; Liu, J. X.; Shi, F.; Xu, Q.; Jiang, Y. Y.; Liu, G. S.; Hu, Z. Q. Synthesis of Sodium Tungsten Bronze via Hydrothermal Method Assisted by Citric Acid. *AMR* **2013**, *712–715*, 280–283. https://doi.org/10.4028/www.scientific.net/AMR.712-715.280.

(56) Chao, L.; Sun, C.; Dou, J.; Li, J.; Liu, J.; Ma, Y.; Xiao, L. Tunable Transparency and NIR-Shielding Properties of Nanocrystalline Sodium Tungsten Bronzes. *Nanomaterials* **2021**, *11* (3), 731. https://doi.org/10.3390/nano11030731.

(57) Kihlborg, L.; Hussain, A. Alkali Metal Location and Tungsten Off-Center Displacement in Hexagonal Potassium and Cesium Tungsten Bronzes. *Materials Research Bulletin* **1979**, *14* (5), 667–674. https://doi.org/10.1016/0025-5408(79)90050-3.

(58) Guo, C.; Yin, S.; Huang, L.; Sato, T. Synthesis of One-Dimensional Potassium Tungsten Bronze with Excellent near-Infrared Absorption Property. *ACS Appl. Mater. Interfaces* **2011**, *3* (7), 2794–2799. https://doi.org/10.1021/am200631e.

(59) Qin, J.; Xing, Y.; Zhang, G. Synthesis of Potassium Tungsten Bronze Nanosheets by Phase Transformation. *J. Am. Ceram. Soc.* **2013**, *96* (5), 1617–1621. https://doi.org/10.1111/jace.12173.

(60) Shi, F.; Liu, J.; Dong, X.; Xu, Q.; Luo, J.; Ma, H. Hydrothermal Synthesis of CsxWO3 and the Effects of N2 Annealing on Its Microstructure and Heat Shielding Properties. *Journal of Materials Science & Technology* **2014**, *30* (4), 342–346. https://doi.org/10.1016/j.jmst.2013.08.018.

(61) Liu, J.-X.; Shi, F.; Dong, X.-L.; Liu, S.-H.; Fan, C.-Y.; Yin, S.; Sato, T. Morphology and Phase Controlled Synthesis of CsxWO3 Powders by Solvothermal Method and Their Optical Properties. *Powder Technology*, 2015, *270*, 329–336. https://doi.org/10.1016/j.powtec.2014.10.032.

(62) Hirano, T.; Nakakura, S.; Rinaldi, F. G.; Tanabe, E.; Wang, W.-N.; Ogi, T. Synthesis of Highly Crystalline Hexagonal Cesium Tungsten Bronze Nanoparticles by Flame-Assisted Spray Pyrolysis. *Advanced Powder Technology* **2018**, *29* (10), 2512–2520. https://doi.org/10.1016/j.apt.2018.07.001.

(63) Liu, J.; Xu, Q.; Shi, F.; Liu, S.; Luo, J.; Bao, L.; Feng, X. Dispersion of Cs0.33WO3 Particles for Preparing Its Coatings with Higher near Infrared Shielding Properties. *Applied Surface Science*, 2014, *309*, 175–180. https://doi.org/10.1016/j.apsusc.2014.05.005.

(64) Long, C. S.; Lu, H.-H.; Lii, D.-F.; Huang, J.-L. Effects of Annealing on Near-Infrared Shielding Properties of Cs-Doped Tungsten Oxide Thin Films Deposited by Electron Beam Evaporation. *Surface and Coatings Technology*, 2015, *284*, 75–79. https://doi.org/10.1016/j.surfcoat.2015.06.078.

(65) Machida, K.; Adachi, K. Ensemble Inhomogeneity of Dielectric Functions in Cs-Doped Tungsten Oxide Nanoparticles. *The Journal of Physical Chemistry C*, 2016, *120*, 16919–16930. https://doi.org/10.1021/acs.jpcc.6b02936.

(66) Guo, C.; Yin, S.; Yan, M.; Sato, T. Facile Synthesis of Homogeneous CsxWO3 Nanorods with Excellent Low-Emissivity and NIR Shielding Property by a Water Controlled-Release Process. *Journal of Materials Chemistry*, 2011, *21*, 5099–5105. https://doi.org/10.1039/C0JM04379F.

(67) Liu, J.-X.; Ando, Y.; Dong, X.-L.; Shi, F.; Yin, S.; Adachi, K.; Chonan, T.; Tanaka, A.; Sato, T. Microstructure and Electrical–Optical Properties of Cesium Tungsten Oxides Synthesized by Solvothermal Reaction Followed by Ammonia Annealing. *Journal of Solid State Chemistry*, 2010, *183*, 2456–2460. https://doi.org/10.1016/j.jssc.2010.08.017.

(68) Liu, J.-X.; Shi, F.; Dong, X.-L.; Xu, Q.; Yin, S.; Sato, T. Nanocrystalline CsxWO3 Particles: Effects of N2 Annealing on Microstructure and near-Infrared Shielding Characteristics. *Materials Characterization* **2013**, *84*, 182–187. https://doi.org/10.1016/j.matchar.2013.08.001.

(69) Shen, B.; Ding, S.; Wang, Y.; Lu, L.; Yang, H. Novel One-Pot Solvothermal Synthesis and Phase-Transition Mechanism of Hexagonal CsxWO3 Nanocrystals with Superior near-Infrared Shielding Property for Energy-Efficient Windows. *Solar Energy* **2021**, *230*, 401–408. https://doi.org/10.1016/j.solener.2021.10.057.

(70) Zhu, Y.; Wang, B.; Zhang, Q.; Wang, H.; Zhu, J.; Liu, Y.; Zhang, Y.; Sun, X.; Zhang, X.; Yun, S.; Jiang, H.; Gao, F.; Kang, L. Paraffin Wax–Cs0.33WO3 Composite Windows with Excellent near Infrared Shielding and Thermal Energy Storage Abilities. *Chem. Pap.* **2019**, *73* (7), 1677–1684. https://doi.org/10.1007/s11696-019-00719-8.

(71) Qi, S.; Xiao, X.; Lu, Y.; Huan, C.; Zhan, Y.; Liu, H.; Xu, G. A Facile Method to Synthesize Small-Sized and Superior Crystalline $Cs_{0.32}WO_3$ Nanoparticles for Transparent NIR Shielding Coatings. *CrystEngComm* **2019**, *21* (21), 3264–3272. https://doi.org/10.1039/C9CE00225A.

(72) Guo, C.; Yin, S.; Huang, L.; Yang, L.; Sato, T. Discovery of an Excellent IR Absorbent with a Broad Working Waveband: CsxWO3 Nanorods. *Chem. Commun.* **2011**, *47* (31), 8853. https://doi.org/10.1039/c1cc12711j.

(73) Shanks, H. R. Growth of Tungsten Bronze Crystals by Fused Salt Electrolysis. *Journal of Crystal Growth* **1972**, *13–14*, 433–437. https://doi.org/10.1016/0022-0248(72)90199-6.

(74) Zhu, Y. T.; Manthiram, A. New Route for the Synthesis of Tungsten Oxide Bronzes. *Journal of Solid State Chemistry* **1994**, *110* (1), 187–189. https://doi.org/10.1006/jssc.1994.1156.

(75) Gao, T.; Jelle, B. P. Visible-Light-Driven Photochromism of Hexagonal Sodium Tungsten Bronze Nanorods. *J. Phys. Chem. C* **2013**, *117* (26), 13753–13761. https://doi.org/10.1021/jp404597c.

(76) Guo, C.; Yu, H.; Feng, B.; Gao, W.; Yan, M.; Zhang, Z.; Li, Y.; Liu, S. Highly Efficient Ablation of Metastatic Breast Cancer Using Ammonium-Tungsten-Bronze Nanocube as a Novel 1064 Nm-Laser-Driven Photothermal Agent. *Biomaterials* **2015**, *52*, 407–416. https://doi.org/10.1016/j.biomaterials.2015.02.054.

(77) Zeng, X.; Zhou, Y.; Ji, S.; Luo, H.; Yao, H.; Huang, X.; Jin, P. The Preparation of a High Performance Near-Infrared Shielding CsxWO3/SiO2 Composite Resin Coating and Research on Its Optical Stability under Ultraviolet Illumination. *J. Mater. Chem. C* **2015**, *3* (31), 8050–8060. https://doi.org/10.1039/C5TC01411E.

(78) Chen, Y.; Zeng, X.; Zhou, Y.; Li, R.; Yao, H.; Cao, X.; Jin, P. Core-Shell Structured CsxWO3@ZnO with Excellent Stability and High Performance on near-Infrared Shielding. *Ceramics International* **2018**, *44* (3), 2738–2744. https://doi.org/10.1016/j.ceramint.2017.11.004.

(79) Linyuan, Z.; Mingqing, Y.; Yong, L. Solvothermal Synthesis and Near-Infrared Shielding Properties of Cs $_{0.3}$ WO $_3$ /WO $_3$ Composites. *Int. J. Nanosci.* **2020**, *19* (04), 1950032. https://doi.org/10.1142/S0219581X19500327.

(80) Nakakura, S.; Machida, K.; Tanabe, E.; Adachi, K.; Ogi, T. Improved Photochromic Stability in Less Deficient Cesium Tungsten Bronze Nanoparticles. *Advanced Powder Technology* **2020**, *31* (2), 702–707. https://doi.org/10.1016/j.apt.2019.11.025.

(81) Song, X.; Liu, J.; Shi, F.; Fan, C.; Ran, S.; Zhang, H.; Zou, Z. Facile Fabrication of KmCsnWO3 with Greatly Improved Near-Infrared Shielding Efficiency Based on W5+-Induced Small Polaron and Local Surface Plasmon Resonance (LSPR) Modulation. *Solar Energy Materials and Solar Cells* **2020**, *218*, 110769. https://doi.org/10.1016/j.solmat.2020.110769.

(82) Yi, L.; Zhao, W.; Huang, Y.; Wu, X.; Wang, J.; Zhang, G. Tungsten Bronze Cs0.33WO3 Nanorods Modified by Molybdenum for Improved Photocatalytic CO2 Reduction Directly from Air. *Sci. China Mater.* **2020**, *63* (11), 2206–2214. https://doi.org/10.1007/s40843-019-1263-1.

(83) Wang, T.; Li, Y.; Li, J.; Feng, Z.; Sun, D.; Zhao, B.; Xu, Y.; Li, R.; Cai, H. Synthesis and Infrared Shielding Properties of Molybdenum-Containing Ammonium Tungsten Bronzes. *RSC Adv.* **2014**, *4* (82), 43366–43370. https://doi.org/10.1039/C4RA06946C.

(84) Teoh, W. Y.; Amal, R.; Mädler, L. Flame Spray Pyrolysis: An Enabling Technology for Nanoparticles Design and Fabrication. *Nanoscale* **2010**, *2* (8), 1324. https://doi.org/10.1039/c0nr00017e.

(85) He, T.; V. Jokerst, J. Structured Micro/Nano Materials Synthesized via Electrospray: A Review. *Biomaterials Science* **2020**, *8* (20), 5555–5573. https://doi.org/10.1039/D0BM01313G.

(86) Height, M. J.; Howard, J. B.; Tester, J. W.; Vander Sande, J. B. Flame Synthesis of Single-Walled Carbon Nanotubes. *Carbon* **2004**, *42* (11), 2295–2307.

(87) Hou, X.; Choy, K.-L. Processing and Applications of Aerosol-Assisted Chemical Vapor Deposition. *Chem. Vap. Deposition* **2006**, *12* (10), 583–596. https://doi.org/10.1002/cvde.200600033.

(88) Mooney, J. B.; Radding, S. B. Spray Pyrolysis Processing. *Annual Review of Materials Science* **1982**, *12* (1), 81–101. https://doi.org/10.1146/annurev.ms.12.080182.000501.

(89) Draine, B. T.; Flatau, P. J. User Guide for the Discrete Dipole Approximation Code DDSCAT 7.3. *arXiv:1305.6497 [astro-ph, physics:cond-mat, physics:physics]* **2013**.

(90) Padiyath, R.; Haak, C.; Gilbert, L.; Company, M.; Paul, S. Spectrally Selective Window Films. 5.

(91) Schaefer, C.; Bräuer, G.; Szczyrbowski, J. Low Emissivity Coatings on Architectural Glass. *Surface and Coatings Technology* **1997**, *93* (1), 37–45. https://doi.org/10.1016/S0257-8972(97)00034-0.

(92) Berning, P. H.; Turner, A. F. Induced Transmission in Absorbing Films Applied to Band Pass Filter Design. *J. Opt. Soc. Am.* **1957**, *47* (3), 230. https://doi.org/10.1364/JOSA.47.000230.

(93) Berning, P. H. Principles of Design of Architectural Coatings. *Appl. Opt.* **1983**, *22* (24), 4127. https://doi.org/10.1364/AO.22.004127.

(94) Kimura, S.; Nanba, T.; Kunii, S.; Suzuki, T.; Kasuya, T. Anomalous Infrared Absorption in Rare-Earth Hexaborides. *Solid State Communications* **1990**, *75* (9), 717–720. https://doi.org/10.1016/0038-1098(90)90233-2.

(95) Guo, C.; Yin, S.; Zhang, P.; Yan, M.; Adachi, K.; Chonan, T.; Sato, T. Novel Synthesis of Homogenous CsxWO3 Nanorods with Excellent NIR Shielding Properties by a Water Controlled-Release Solvothermal Process. *J. Mater. Chem.* **2010**, *20* (38), 8227. https://doi.org/10.1039/c0jm01972k.

(96) Svensson, J. S. E. M.; Granqvist, C. G. Modulated Transmittance and Reflectance in Crystalline Electrochromic WO_3 Films: Theoretical Limits. *Appl. Phys. Lett.* **1984**, *45* (8), 828–830. https://doi.org/10.1063/1.95415.

(97) Takeda, H.; Adachi, K. Near Infrared Absorption of Tungsten Oxide Nanoparticle Dispersions. *J American Ceramic Society* **2007**, *0* (0), 070922001254002-??? https://doi.org/10.1111/j.1551-2916.2007.02065.x.

(98) Charitidis, C. A.; Georgiou, P.; Koklioti, M. A.; Trompeta, A.-F.; Markakis, V. Manufacturing Nanomaterials: From Research to Industry. *Manufacturing Rev.* **2014**, *1*, 11. https://doi.org/10.1051/mfreview/2014009.

(99) Gurav, A.; Kodas, T.; Pluym, T.; Xiong, Y. Aerosol Processing of Materials. *Aerosol Science and Technology* **1993**, *19* (4), 411–452. https://doi.org/10.1080/02786829308959650.

(100) Wöhler, F. Ueber Das Wolfram. *Annalen der Physik* **1824**, *78* (12). https://doi.org/10.1002/andp.18240781202.

(101) Straumanis, M. E. The Sodium Tungsten Bronzes. I. Chemical Properties and Structure. *J. Am. Chem. Soc.* **1949**, *71* (2), 679–683. https://doi.org/10.1021/ja01170a085.

(102) Straumanis, M. E.; Hsu, S. S. The Lithium Tungsten Bronzes. *J. Am. Chem. Soc.* **1950**, *72* (9), 4027–4030. https://doi.org/10.1021/ja01165a053.

(103) Magnéli, A.; Blomberg, B.; Reio, L.; Saluste, E.; Stjernholm, R.; Ehrensvärd, G. Contribution to the Knowledge of the Alkali Tungsten Bronzes. *Acta Chem. Scand.* **1951**, *5*, 372–378. https://doi.org/10.3891/acta.chem.scand.05-0372.

(104) Brown, B.; Banks, E. The Sodium Tungsten Bronzes1, 2. *Journal of the American Chemical Society* **1954**, *76* (4), 963–966.

(105) Guo, C.; Yin, S.; Yan, M.; Kobayashi, M.; Kakihana, M.; Sato, T. Morphology-Controlled Synthesis of $W_{18}O_{49}$ Nanostructures and Their Near-Infrared Absorption Properties. *Inorg. Chem.* **2012**, *51* (8), 4763–4771. https://doi.org/10.1021/ic300049j.

(106) Ferrin, P.; Nilekar, A. U.; Greeley, J.; Mavrikakis, M.; Rossmeisl, J. Reactivity Descriptors for Direct Methanol Fuel Cell Anode Catalysts. *Surface Science* **2008**, *602* (21), 3424–3431. https://doi.org/10.1016/j.susc.2008.08.011.

(107) Diehl, R.; Brandt, G.; Salje, E. The Crystal Structure of Triclinic WO $_3$. *Acta Crystallogr B Struct Sci* **1978**, *34* (4), 1105–1111. https://doi.org/10.1107/S0567740878005014.

(108) Daly, G. *Glazes and Glazing Techniques: A Glaze Journey*; Gentle Breeze Pub., 1996.

(109) Eppler, R. A.; Obstler, M. *Understanding Glazes*; American ceramic society, 2005.

(110) Granqvist, C. G. *Handbook of Inorganic Electrochromic Materials*; Elsevier: Amsterdam ; New York, 1995.

(111) Sun, C.; Liu, J.; Chao, L. Theoretical Analysis on Optical Properties of Cs0.33WO3 Nanoparticles with Different Sizes, Shapes and Structures. *Materials Letters* **2020**, *272*, 127847. https://doi.org/10.1016/j.matlet.2020.127847.

(112) Hahn, D. W. Light Scattering Theory. *Department of Mechanical and Aerospace Engineering, University of Florida* **2009**.

(113) Young, A. T. Rayleigh Scattering. *Phys. Today* **1982**, *35* (1), 42–48.

(114) Marple, V. A.; Rubow, K. L.; Behm, S. M. A Microorifice Uniform Deposit Impactor (MOUDI): Description, Calibration, and Use. *Aerosol Science and Technology* **1991**, *14* (4), 434–446. https://doi.org/10.1080/02786829108959504.

(115) Cunningham, E.; Larmor, J. On the Velocity of Steady Fall of Spherical Particles through Fluid Medium. *Proceedings of the Royal Society of London. Series A, Containing Papers of a Mathematical and Physical Character* **1910**, *83* (563), 357–365. https://doi.org/10.1098/rspa.1910.0024.

(116) Konopka, J. Options for Quantitative Analysis of Light Elements by SEM/EDS. *Technical Note* **2013**, *52523*.

(117) Lee, S. Y.; Kim, J. Y.; Lee, J. Y.; Song, H. J.; Lee, S.; Choi, K. H.; Shin, G. Facile Fabrication of High-Efficiency near-Infrared Absorption Film with Tungsten Bronze Nanoparticle Dense Layer. *Nanoscale Research Letters* **2014**, *9* (1), 294. https://doi.org/10.1186/1556-276X-9-294.

(118) Bohren, C. F.; Huffman, D. R. *Absorption and Scattering of Light by Small Particles*; John Wiley & Sons, 2008.

(119) Chao, L.; Bao, L.; Wei, W.; Tegus, O. A Review of Recent Advances in Synthesis, Characterization and NIR Shielding Property of Nanocrystalline Rare-Earth Hexaborides and Tungsten Bronzes. *Solar Energy* **2019**, *190*, 10–27. https://doi.org/10.1016/j.solener.2019.07.087.

(120) Chen, D.; Tu, H. Aerosol-Assisted Synthesis of Crystalline Tungsten Bronze Particles. WO2022035631A1, February 17, 2022. https://patents.google.com/patent/WO2022035631A1/en?oq=WO2022035631A1 (accessed 2022-03-21).

(121) Sato, K.; Ando, I.; Yoshio, S.; Adachi, K. Cesium Polytungstate in Sputtered Solar Control Films. I. Microstructure and Optical Properties. *Journal of Applied Physics* **2021**, *130* (11), 113102. https://doi.org/10.1063/5.0058748.

(122) Mie Scattering. *Wikipedia*; 2022.

(123) *Wave Optics Module User’s Guide*, COMSOL Multiphysics® v. 6.1.; COMSOL AB: Stockholm, Sweden.

(124) Lynch, D. W.; Rosei, R.; Weaver, J. H.; Olson, C. G. The Optical Properties of Some Alkali Metal Tungsten Bronzes from 0.1 to 38 EV. *Journal of Solid State Chemistry* **1973**, *8* (3), 242–252. https://doi.org/10.1016/0022-4596(73)90092-3.

(125) Tegg, L.; Cuskelly, D.; Keast, V. J. The Sodium Tungsten Bronzes as Plasmonic Materials: Fabrication, Calculation and Characterization. *Mater. Res. Express* **2017**, *4* (6), 065703. https://doi.org/10.1088/2053-1591/aa6c40.

(126) Tu, H.; Chen, D. Aerosol-Assisted Process to Produce Sodium Tungsten Bronze Particles from Aqueous Solutions and Effect of Particle Size on the NIR Shielding Performance. *Powder Technology* **2023**, *416*, 118217. https://doi.org/10.1016/j.powtec.2023.118217.

(127) *Standard Tables for Reference Solar Spectral Irradiances: Direct Normal and Hemispherical on 37° Tilted Surface*. https://www.astm.org/g0173-03r20.html (accessed 2023-02-03).

Appendix: Photos

Figure 0-1. Part of the setup to generate aerosol flow before entering the furnace.

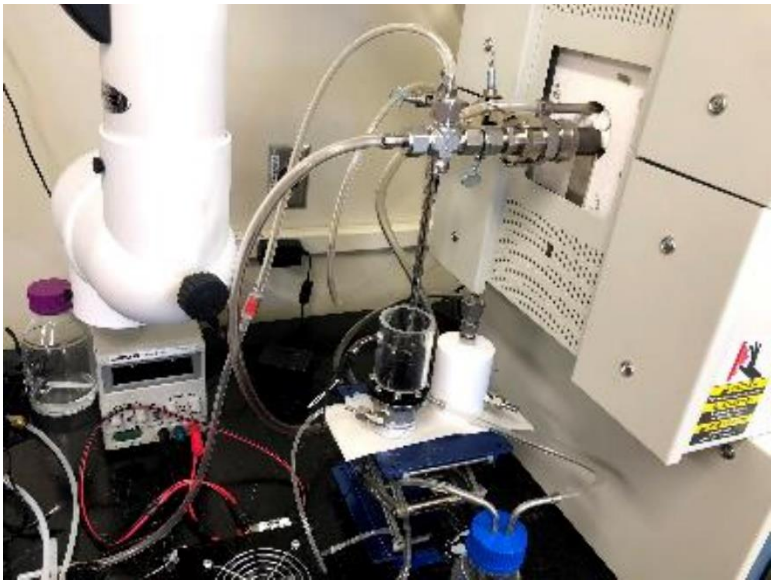

Figure 0-2. Part of the setup with the dilution flow and nebulizer.

Appendix: Vita

Education

B.S., Inorganic Non-metallic Materials Engineering, Wuhan University of Technology, China, 2011

M.S., Material Science, Wuhan University of Technology, China, 2015

Ph.D. student, Mechanical & Nuclear Engineering, Virginia Commonwealth University, 2017-2023.05.13 (Expected)

Publication

1. **Tu, H.**; Chen, D. Aerosol-Assisted Process to Produce Sodium Tungsten Bronze Particles from Aqueous Solutions and Effect of Particle Size on the NIR Shielding Performance. *Powder Technology* 2023, 416, 118217. https://doi.org/10.1016/j.powtec.2023.118217.
2. **Tu, H.**, Wang, W., Chen, D.-R., 2020. Aerosol-assisted Production of NIR Shielding Nanoparticles: Sodium Tungsten Bronze. *Aerosol Air Qual.* Res. 20, 690–701. https://doi.org/10.4209/aaqr.2019.10.0548
3. **Tu, H.**, Xu, L., Mou, F., Guan, J., 2016. Highly active Ta_2O_5 microcubic single crystals: facet energy calculation, facile fabrication and enhanced photocatalytic activity of hydrogen production. *J. Mater. Chem. A* 4, 16562–16568. https://doi.org/10.1039/C6TA06648H
4. **Tu, H.** Chen, D. Optical Performance of Sodium Tungsten Bronze Particles in Transparent Matrix: an Ensemble Particle Modeling Study. *Aerosol Air Qual. Res.* Submitted.
5. **Tu, H.**, Xu, L., Mou, F., Guan, J., 2015. Single crystalline tantalum oxychloride microcubes: controllable synthesis, formation mechanism and enhanced photocatalytic hydrogen production activity. *Chem. Commun.* 51, 12455–12458. https://doi.org/10.1039/C5CC03455H
6. Xu, L., Sun, X., **Tu, H.**, Jia, Q., Gong, H., Guan, J., 2016. Synchronous etching-epitaxial growth fabrication of facet-coupling $NaTaO_3/Ta_2O_5$ heterostructured nanofibers for enhanced photocatalytic hydrogen production. Applied Catalysis B: Environmental 184, 309–319. https://doi.org/10.1016/j.apcatb.2015.11.041
7. Sun, X., Shi, W., **Tu, H.**, Xu, L., Yan, Y., Guan, J., 2014. Precursors-Decomposited Synthesis and Visible-Light-Response Photocatalystic Properties of Uniform Porous Bi_2O_3 Nanospheres. *NANO* 09, 1450067. https://doi.org/10.1142/S1793292014500672

Patent

1. Daren Chen, **Hao Tu**. *Scalable, fast and continuous production of crystalline tungsten bronze particles with tunable sizes*, 2020. In application. https://innovationgateway.vcu.edu/technologies/engineering/continuous-aerosol-based-synthesis-for-tungsten-bronze-particles-.html.
2. Guan, J., **Tu, H**., Xu, L. *A kind of tantalum oxychloride microcube photo-catalyst and its preparation and application*. (CN104874410B)